



저작자표시-비영리-변경금지 2.0 대한민국

이용자는 아래의 조건을 따르는 경우에 한하여 자유롭게

- 이 저작물을 복제, 배포, 전송, 전시, 공연 및 방송할 수 있습니다.

다음과 같은 조건을 따라야 합니다:



저작자표시. 귀하는 원저작자를 표시하여야 합니다.



비영리. 귀하는 이 저작물을 영리 목적으로 이용할 수 없습니다.



변경금지. 귀하는 이 저작물을 개작, 변형 또는 가공할 수 없습니다.

- 귀하는, 이 저작물의 재이용이나 배포의 경우, 이 저작물에 적용된 이용허락조건을 명확하게 나타내어야 합니다.
- 저작권자로부터 별도의 허가를 받으면 이러한 조건들은 적용되지 않습니다.

저작권법에 따른 이용자의 권리는 위의 내용에 의하여 영향을 받지 않습니다.

이것은 [이용허락규약\(Legal Code\)](#)을 이해하기 쉽게 요약한 것입니다.

[Disclaimer](#)

Doctoral Dissertation

**Investigation of ZrN Non-Reactively  
Sputtered Diffusion Barrier Coating  
for U-Mo Dispersion Fuel**

Ji Hyeon Kim

Department of Nuclear Engineering

Graduate School of UNIST

2019

**Investigation of ZrN Non-Reactively  
Sputtered Diffusion Barrier Coating  
for U-Mo Dispersion Fuel**

Ji Hyeon Kim

Department of Nuclear Engineering

Graduate School of UNIST

**Investigation of ZrN Non-Reactively  
Sputtered Diffusion Barrier Coating  
for U-Mo Dispersion Fuel**

A dissertation  
submitted to the Graduate School of UNIST  
in partial fulfillment of the  
requirements for the degree of  
Doctor of Philosophy

Ji Hyeon Kim

12. 07. 2018

Approved by



Advisor

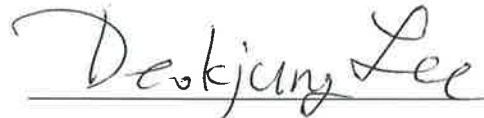
Deokjung Lee

**Investigation of ZrN Non-Reactively  
Sputtered Diffusion Barrier Coating for  
U-Mo Dispersion Fuel**

Ji Hyeon Kim

This certifies that the dissertation of Ji Hyeon Kim is approved.

12. 07. 2018



Advisor: Prof. Deokjung Lee




Co-advisor: Prof. Dong-Seong Sohn



Committee Member: Dr. Jong Man Park



Committee Member: Dr. Yeon Soo Kim



Committee Member: Prof. Jaeyeong Park

## Abstract

Zirconium nitride (ZrN) coating as a diffusion barrier layer has been applied to a U-7wt.% Mo (U-7Mo)/Al dispersion fuel plate owing to its high melting point, high thermodynamic stability against U-Mo and Al, high hardness, and low absorption cross section for thermal neutrons. However, it has been experimentally revealed that a ZrN coating layer adopted in a U-Mo/Al dispersion fuel plate experiences a functional failure locally, and hence undesirably extensive fission-induced interaction layers (ILs) between U-7Mo fuel powders and the surrounding Al matrix reaction layer are locally produced when irradiated. It is believed that the local coating damage generated during the dispersion-fuel-plate fabrication process accelerates the U-Mo/Al interdiffusion by acting as a fast diffusion path of solid materials. Unfortunately, there have been no studies scientifically identifying the causes of, or presenting solutions to, the problem of ZrN coating damage. Accordingly, based on comprehensive microstructural studies, the aim of this research is to experimentally and numerically investigate ZrN coating fracturing as a function of several variables at a high heat-treatment temperature during dispersion-fuel-plate fabrication. This research will help present appropriate solutions for preventing the occurrence of coating fracturing at the heat-treatment temperature, taking into account a realistic coating microstructure. ZrN coating was deposited onto U-7Mo powders using a direct-current magnetron non-reactive sputtering machine equipped with a turnable mixing drum. Microstructural studies on the as-fabricated ZrN coatings were conducted using a scanning electron microscope (SEM), energy-dispersive X-ray spectroscopy (EDS), and X-ray diffractometer (XRD). This research is composed of the following three parts:

First, the microstructural properties and residual stress of as-deposited ZrN coatings were measured as a function of the coating thickness ranging from 0.1 to 2.6  $\mu\text{m}$ . SEM and XRD results show that the microstructural characteristics (e.g., compact density and crystallographic properties) of the ZrN coating varied depending on the coating thickness. In addition, interlaminar delamination occurred when the coating thickness grew to greater than 2.2  $\mu\text{m}$ . Therefore, the thickness of the ZrN coating is considered to be an important factor influencing its microstructure, and thus its fracture resistance.

Second, the effects of the U-7Mo substrate size on the thickness and microstructure of as-fabricated ZrN coatings with a mean thickness of 0.9  $\mu\text{m}$  deposited on 45–90- $\mu\text{m}$  sized U-7Mo powders were investigated. With an increase in the U-7Mo substrate size, the ZrN coatings showed an increase in the coating thickness and grain size, and a decrease in the compact density owing to the increased macroscopic defects. Based on the measured coating thickness, a semi-empirical model expressing the relationship between the coating thickness and substrate size was newly developed. Based on the experimental results, it can be predicted that the U-7Mo substrate size, as well as the ZrN coating thickness, also affects the fracture resistance of the ZrN coating.

Based on the above parametric studies on the ZrN coating microstructure, the structural integrity of ZrN coating was investigated at a high fabrication temperature as a function of the coating thickness, U-7Mo substrate size, and annealing temperature. To theoretically assess whether a mechanical failure of the ZrN coatings occurs at a given coating thickness, U-7Mo substrate size, and annealing temperature, a finite element simulation (FES) was conducted. The FES results show that the coating fracture is dependent on the given coating thickness, U-7Mo powder size, and annealing temperature, which affect the fracture criteria or induced tensile-hoop-stress of the corresponding coating. The thicker the coating, the larger the U-Mo substrate size, whereas the higher the heat-treatment temperature, the more likely a coating fracturing is to occur. The FES results are in good accordance with the corresponding experimental results.

## Contents

Abstract .....	i
Contents .....	iii
List of figures.....	vi
List of tables.....	x
Nomenclatures and Abbreviations.....	xi
Chapter 1. Introduction .....	1
1.1. General research background.....	1
1.1.1. Evolution of research and test reactor fuel.....	1
1.1.2. U-Mo/Al fuel type.....	4
1.1.3. Irradiation behavior of U-Mo/Al dispersion fuel plate .....	5
1.2. Application of diffusion barrier into U-Mo/Al dispersion fuel.....	11
1.2.1. Deposition methods for a diffusion barrier coating on U-Mo fuel powders.....	11
1.2.2. Magnetron sputtering .....	13
1.3. Literature review of Zirconium nitride (ZrN) coating .....	17
1.3.1. General application in fields other than nuclear field .....	17
1.3.2. Application as a diffusion barrier in U-Mo/Al dispersion fuel plate .....	17
1.4. Damage to ZrN coating within U-Mo/Al dispersion fuel plates.....	21
1.4.1. Possible causes.....	21
1.4.2. Impacting on diffusion barrier performance .....	22
1.4.3. Factors influencing the coating fracture resistance .....	23
1.5. Objective and scope of the present research .....	24
Chapter 2. Experimental methods.....	46
2.1. Coating deposition .....	46
2.2. Experimental techniques for coating characterization .....	46
2.2.1. Scanning electron microscopy (SEM) .....	46
2.2.2. Energy-dispersive X-ray spectroscopy (EDS) .....	47
2.2.3. X-ray diffractometer (XRD) .....	48
2.2.3.1. Principle and operation condition .....	48
2.2.3.2. Analysis equations for crystallographic properties .....	49
2.3. Annealing tests.....	51
2.4. Sample preparation .....	52
2.4.1. U-7Mo powders .....	52
2.4.2. Sample preparation for characterization .....	52



Chapter 3. Evolution of microstructure and residual stress of ZrN coating with coating growth.....	60
3.1. Analysis results of as-deposited ZrN coatings .....	60
3.1.1. Coating thickness and deposition rate.....	60
3.1.2. Morphology.....	61
3.1.3. Texture .....	62
3.1.4. Lattice parameter and density .....	63
3.1.5. Grain size and microstrain .....	63
3.1.6. Residual stress.....	64
3.2. Discussion.....	65
3.2.1. Microstructural evolution trends of the as-fabricated ZrN coating during growth .	65
3.2.2. Influence of residual stress on the structural integrity of ZrN coating.....	69
3.2.3. Optimum thickness of ZrN coating based on the analyzed microstructure .....	72
Chapter 4. Effect of U-7Mo substrate size on thickness and microstructure of ZrN sputtered coatings .....	91
4.1. Examination results of ZrN coatings.....	91
4.1.1. Coating thickness .....	91
4.1.2. Surface topology .....	93
4.1.3. Crystallographic characteristics .....	93
4.2. Impacting factors for coating microstructure.....	95
4.3. Effect of structure on the diffusion barrier capability of ZrN coating .....	96
4.4. Established semi-analytical model describing ZrN coating thickness as a function of U-7Mo substrate size .....	97
Chapter 5. Effect of coating thickness, U-Mo substrate size, and annealing temperature on structural failure of ZrN coating on U-Mo powders at a high post-deposition processing temperature .....	113
5.1. Characterization of as-deposited ZrN coatings with different thicknesses .....	113
5.1.1. Morphology.....	113
5.1.2. Grain size and microstrain .....	115
5.2. Experimental examination of heat-treated ZrN coating.....	116
5.2.1. Effect of coating thickness and substrate size (coating diameter) on ZrN coating failure .....	116
5.2.2. Effect of heat-treatment temperature on ZrN coating failure.....	117
5.3. Stress analysis of heat-treated ZrN coating by finite element simulation.....	118
5.3.1. Stress development .....	118
5.3.2. Failure criterion.....	119
5.3.2.1. Failure of coating thinner than critical thickness .....	119

5.3.2.2. Failure of coating thicker than critical thickness .....	120
5.3.3. Modelling of finite element simulations .....	121
5.4. Finite element simulation results .....	123
5.4.1. Effect of coating thickness and diameter on the coating failure .....	123
5.4.2. Heat-treatment temperature effect on coating failure .....	124
Chapter 6. Conclusions .....	143
6.1. Summary .....	143
6.2. Conclusions.....	146
6.3. Other uncertainties and Future works .....	147
References .....	148
Acknowledgements.....	165
Journal Publications .....	166

## List of figures

Figure 1. Phase diagram of uranium-molybdenum alloy [214].	31
Figure 2. Time-Temperature-Transformation diagram for $\gamma$ -U alloy fuel candidates [98].	32
Figure 3. Schematic of commonly used plate-type dispersion fuel: (a) overview and (b) cross-sectional image [215].	33
Figure 4. Normal fuel assembly loaded into research and test reactors [216].	34
Figure 5. In-pile irradiation test results of U-Mo/Al dispersion fuel shows a severe swelling and even rupture with increasing the burnup [9].	35
Figure 6. Recrystallization (upper images) and swelling behavior (bottom graph) of irradiated U-10Mo/Al dispersion fuel plate as a function of fission density [8].	36
Figure 7. U-Mo/Al dispersion fuels irradiated upto a high burnup shows fission gases are agglomerated into a large pore by 'snowploughing effect' of U-Mo/Al interaction layer [9].	37
Figure 8. (a) Photo and schematic of the STEPS & DRUMS [97] and (b) schematic diagram of a general barrel sputter deposition system [217].	38
Figure 9. Schematics and photo of three-type CVD systems fabricating a diffusion barrier coating on U-Mo dispersion fuel powders: (a) Pack-cementation for U-Si coating [78], (b) CVD with a tunable substrate mixer for U-N coating [77, 78], and (c) FB-CVD for ZrN coating [67].	39
Figure 10. (a) Set-up and (b) schematic view of ALD Savannah system [218].	40
Figure 11. Magnetron sputtering systems for ZrN coating deposition: (a) non-reactive system (KAERI, used in this research) and (b) reactive sputtering (SCK-CEN).	41
Figure 12. Thornton's structure zone model [177]: (a) coating morphologies as a function of deposition temperature and working pressure, and the (b) cross-section and (c) growth steps and corresponding dominant diffusion mechanism of Zone I, T, and II structures as a function of coating thickness [128].	42
Figure 13. Three types of U-Mo/Al interaction layer observed in ZrN coated U-7Mo/Al dispersion fuel irradiated upto $\sim 5.0 \times 10^{21}$ fission/cm <sup>3</sup> : (a) thin IL, (b) 'erupting volcano' shaped extensive IL near the coating crack, and (c) huge IL formed through the coating crack that once existed [36].	43
Figure 14. (a) TEM bright-field cross-sectional image and (b) TEM-EDS mapping image of a ZrN reactively sputtered coating layer on a U-7Mo powder [61].	44
Figure 15. (a) Critical stress sources for ZrN coating damage during a general fabrication process of dispersion fuel plates and (b) exploded view of a U-Mo/Al dispersion fuel assembly with a uranium density of 8 gU/cm <sup>3</sup> [8].	45
Figure 16. (a) Photo and (b) schematic illustration of DC magnetron sputtering coating system used in this research.	54

Figure 17. Schematic drawings of (a) SEM and (b) interaction volume (detection volume) for an electron beam [212, 213].	55
Figure 18. (a) EDS principle and (b) an EDS spectrum example [214, 215].	56
Figure 19. (a) Schematic representation of XRD experimental setup (left) and Bragg's law (right), and (b) XRD spectra [223].	57
Figure 20. SEM SE top-view micrograph of 45–90 $\mu\text{m}$ -sized U-7Mo powders.	58
Figure 21. XRD profile of U-7Mo powders in the size range of 45–90 $\mu\text{m}$ .	59
Figure 22. SEM BSE cross-sectional image of mean 2.2 $\mu\text{m}$ -thick ZrN coating on a U-7Mo powder.	76
Figure 23. EDS mapping image of mean 2.2 $\mu\text{m}$ -thick ZrN coating on a U-7Mo powder.	77
Figure 24. SEM BSE top view image of U-7Mo powders coated with a mean 2.2 $\mu\text{m}$ -thick ZrN layer.	78
Figure 25. Plot of coating thickness against deposition time.	79
Figure 26. Top view SEM BSE image of a mean 2.6 $\mu\text{m}$ -thick ZrN coating showing laminar spallation.	80
Figure 27. SEM BSE fractured cross-sectional image of a 2.7 $\mu\text{m}$ -thick ZrN coating.	81
Figure 28. SEM BSE top-view images of mean (a) 0.1, (b) 0.2, (c) 0.5, (d) 0.8, (e) 2.2, and (f) 2.6 $\mu\text{m}$ -thick ZrN coatings.	82
Figure 29. High magnification SEM BSE top-view image of a mean 2.6 $\mu\text{m}$ -thick ZrN coating.	83
Figure 30. Defect types detected in SEM SE top-view image of mean 0.8 $\mu\text{m}$ -thick ZrN coatings: (a) hillock and (b) pinhole & crater.	84
Figure 31. XRD profiles of U-7Mo powders deposited with ZrN coatings of different thicknesses.	85
Figure 32. Texture coefficient of ZrN coatings as a function of coating thickness.	86
Figure 33. Lattice constant and calculated density of ZrN coatings with different thicknesses.	87
Figure 34. Halder-Wagner plot with slope of $K\lambda/D$ and y-intercept of $\eta^2$ .	88
Figure 35. Grain size and lattice strain obtained by Halder-Wagner plotting.	89
Figure 36. Residual stress evolution of ZrN coatings.	90
Figure 37. Cross-sectional EDS mapping images of a ZrN-coated U-7Mo powder [63].	101
Figure 38. Measured thickness and deposition rate of ZrN coatings on U-7Mo powders of various sizes [63].	102
Figure 39. SEM BSE top-view image of 45–90 $\mu\text{m}$ -sized U-7Mo powders coated with a ZrN single layer [63].	103
Figure 40. SEM BSE top-view micrographs of ZrN coatings on different sizes of U-7Mo powders: (a) 0.55 $\mu\text{m}$ -thick coating for 45 $\mu\text{m}$ -diameter U-7Mo powders, (b) 0.80 $\mu\text{m}$ for 53 $\mu\text{m}$ , (c) 0.88 $\mu\text{m}$ for 63 $\mu\text{m}$ , (d) 1.10 $\mu\text{m}$ for 75 $\mu\text{m}$ and (e) 1.17 $\mu\text{m}$ for 90 $\mu\text{m}$ [63].	104

Figure 41. Measured density and total area fraction of surface defects formed in ZrN coatings [63]. .....	105
Figure 42. SEM BSE fractured cross-sectional micrograph (left) and schematic cross-section (right) of a 3.8 $\mu\text{m}$ -thick ZrN coating layer on a U-7Mo powder [62]. In the schematic, (a) 0.55 $\mu\text{m}$ -thick coating for 45 $\mu\text{m}$ -diameter U-7Mo powders, (b) 0.80 $\mu\text{m}$ for 53 $\mu\text{m}$ , (c) 0.88 $\mu\text{m}$ for 63 $\mu\text{m}$ , (d) 1.10 $\mu\text{m}$ for 75 $\mu\text{m}$ and (e) 1.17 $\mu\text{m}$ for 90 $\mu\text{m}$ are displayed [63].....	106
Figure 43. XRD patterns of ZrN-coated U-7Mo powders as a function of the powder size [63].....	107
Figure 44. Lattice constants of ZrN coatings on U-7Mo powders of various sizes [63]. .....	108
Figure 45. Grain size and microstrain of ZrN coatings on U-7Mo powders of different sizes [63]..	109
Figure 46. Forces acting on a U-7Mo powder which are displayed in a schematic diagram of the used coating machine [63].....	110
Figure 47. Linear plot of measured $\cot\alpha$ values (represented by individual data points) versus U-7Mo powder diameter [63].....	111
Figure 48. Fitting the measured values for ZrN coatings to the cosine power law of Eq. (23) [63]..	112
Figure 49. SEM BSE cross-sectional micrograph of ZrN coatings on U-7Mo powders [62]. .....	131
Figure 50. SEM BSE top-view image of ZrN-coated U-7Mo fuel powders [62].....	132
Figure 51. SEM BSE micrograph and schematic (upper-right image) of fractured cross-section of the ZrN coating deposited on a U-7Mo powder for 25 h [62]. .....	133
Figure 52. SEM BSE top-view images of ZrN coatings with deposition times of (a) 2 h, (b) 4 h (0.49 $\mu\text{m}$ -thick ZrN coating on 45 $\mu\text{m}$ -sized powder), (c) 4 h (0.73 $\mu\text{m}$ -thick ZrN coating on 90 $\mu\text{m}$ -sized powder), (d) 7 h, (e) 15 h, and (f) 25 h on a U-7Mo powder [62].....	134
Figure 53. XRD profile of ZrN coatings deposited on 45–90 $\mu\text{m}$ -sized U-7Mo powders for 7 h [62]. .....	135
Figure 54. Halder-Wagner grain size-microstrain plot of ZrN coatings deposited on 45–90 $\mu\text{m}$ -sized U-7Mo powders for 7 h. The slope and the y-intercept of the plot are $K\lambda/D$ and $16\epsilon^2$ , respectively [62].....	136
Figure 55. SEM BSE top-view image of a mean 3.46 $\mu\text{m}$ -thick ZrN coating after annealing at 500°C for 2 h [62]. .....	137
Figure 56. Cross-sectional SEM BSE image of a 3.8 $\mu\text{m}$ -thick ZrN coating layer annealed at 500°C for 2 h [62].....	138
Figure 57. Surficial SEM BSE images of average 1.06 $\mu\text{m}$ -thick ZrN coatings annealed at 300°–700°C for 2 h [62]. .....	139
Figure 58. Crack density of 1.06 $\mu\text{m}$ -thick ZrN coatings various annealing temperatures based on surficial SEM BSE image analysis [62].....	140

Figure 59. Comparison of the calculated hoop stress and fracture criterion of ZrN coatings at different coating thicknesses with respect to two U-7Mo powder sizes [62]. The fracture criterion is ultimate tensile strength for coating thicknesses less than 0.5  $\mu\text{m}$ , and fracture strength for coating thicknesses over 0.5  $\mu\text{m}$ . ..... 141

Figure 60. Comparison of the calculated hoop stress and fracture strength (fracture criterion) of ZrN coatings at different annealing temperatures with respect to two U-7Mo powder sizes (i.e., two coating forms) [62]..... 142

## List of tables

Table 1. Candidates for LEU dispersion fuel [12].	26
Table 2. Advantages and disadvantages of coating deposition methods used for U-Mo dispersion fuel powders.	27
Table 3. Comparison of ZrN coating deposition-systems used in this research and the SELENIUM project (SCK·CEN).	28
Table 4. Material properties of ZrN.	29
Table 5. Analyzed characteristics and necessary studies of ZrN reactively-sputtered coating deposited on U-Mo atomized powder by different coating methods	30
Table 6. Deposition condition of ZrN sputtered coating.	53
Table 7. Summary of measured crystallographic properties of ZrN coatings.	75
Table 8. Measured thicknesses of ZrN coatings on U-7Mo powders as a function of deposition time and U-7Mo powder size [62].	125
Table 9. Observed mechanical failure behavior of ZrN coating on U-7Mo powder as a function of coating thickness and powder size (coating diameter) [62].	126
Table 10. Examined mechanical failure behavior of ZrN coating on U-7Mo powder as a function of annealing temperature and powder size (coating diameter) [62].	127
Table 11. Material properties used in the FEA simulation [62].	128
Table 12. Calculated hoop stress by ABAQUS and estimated coating fracture for different ZrN- coating thickness of 45 and 90 $\mu\text{m}$ -sized U-7Mo powders annealed at 500°C [62].	129
Table 13. Calculated hoop stress by ABAQUS and estimated coating fracture for ZrN coatings on 45 and 90 $\mu\text{m}$ -sized U-7Mo powders annealed at various given temperatures [62].	130

## Nomenclatures and Abbreviations

### Chapter 1

#### Subsection 1.1

RR	=	Research and test reactors
HEU	=	Highly-enriched uranium
LEU	=	Low-enriched uranium
RERTR	=	Reduced Enrichment for Research and Test Reactors
CNEA	=	Comisión Nacional de Energía Atómica, Argentina
AECL	=	Atomic Energy of Canada Limited
CEA	=	Commissariat à l'énergie atomique, France
TUM	=	Technical University of Munich
KAERI	=	Korea Atomic Energy Research Institute
SCK-CEN	=	Studiecentrum voor Kernenergie, Centre de l'Énergie Nucléaire
VNIIM	=	Mendeleev National Research Institute of Metrology
RDIPÉ	=	Research and Development Institute of Power Engineering
IPPE	=	Institute of Physics and Power Engineering
NCCP	=	Novosibirsk Chemical Concentrates Plant
RIAR	=	Research Institute of Atomic Reactors
NNSA	=	National Nuclear Security Administration
ATR	=	Advanced Test Reactor
MURR	=	Missouri Research Reactor
NBSR	=	National Bureau of Standards Reactor
$\alpha$ -U	=	Alpha phase uranium
$\beta$ -U	=	Beta phase uranium
$\gamma$ -U	=	Gamma phase uranium
$\gamma'$ -U	=	Uranium molybdenum intermetallic (U <sub>2</sub> Mo)
$\left(\frac{\Delta V}{V_0}\right)_f$	=	Total fuel swelling
$\left(\frac{\Delta V}{V_0}\right)_s$	=	Fuel swelling induced by fission solid products
$\left(\frac{\Delta V}{V_0}\right)_g$	=	Fuel swelling induced by fission gas products
$f_d$	=	Fission density
wt.%.	=	Weight percent
at.%.	=	Atomic percent
vol.%.	=	Volume percent



FG	=	Fission Gases (Kr and Xe)
TEM	=	Transmission Electron Microscopy
SEM	=	Scanning Electron Microscopy
PIE	=	Post Irradiation Examination
IL	=	Interaction Layer
SELENIUM	=	Surface Engineered Low ENrIched Uranium Molybdenum fuel
$Y_{IL,0}$	=	Interaction layer thickness
$\dot{f}$	=	Fission rate
$R$	=	Ideal gas constant (8.314 J/mol/K)
$T$	=	Temperature of fuel meat
$t$	=	Processing time
$Y_{IL}$	=	Interaction layer thickness considering additional correction factors ( $f_{Si}$ and $f_{Mo}$ )
$f_{Si}$	=	Correction factors for Si content added into the Al matrix
$f_{Mo}$	=	Correction factors for Mo content of the U-Mo fuel
$W_{Si}$	=	Weigh percentage of Si content in the Al matrix
$W_{Mo}$	=	Weigh percentage of Mo content in U-Mo alloy fuel

### Subsection 1.2

SCK·CEN	=	Studiecentrum voor Kernenergie, Centre de l'Energie Nucléaire
PVD	=	Physical vapor deposition
ALD	=	Atomic layer deposition
CVD	=	Chemical vapor deposition
DC	=	Direct Current
RF	=	Radio Frequency
STEPS & DRUMS	=	Sputtering Tool for Engineering Powder Surface and Deposition Reactor
FB-CVD	=	Fluidized Bed Chemical Vapor Deposition
EMPIRE	=	European Mini-Plate IRradiation Experiment
TRIM	=	Transport of Ions in Matter
CTE	=	Coefficient of Thermal Expansion
SZM	=	Structure Zone Model

### Subsection 1.3

BR-2	=	Belgian Reactor 2
------	---	-------------------

**Chapter 2****Subsection 2.1**

EDS = Energy-Dispersive X-ray Spectroscopy

XRD = X-Ray Diffractometer

**Subsection 2.2**

SE = Secondary Electron

BSE = BackScattered Electron

 $d_{hkl}$  = Interplanar spacing of the corresponding (hkl) plane

h, k, l = Miller indices

 $\lambda$  = Wavelength of the radiation beam (0.1506 nm for CuK $\alpha$  radiation) $\theta$  = Diffraction angle $TC_{(hkl)}$  = Texture coefficient of (hkl) orientation $I_{(hkl)}$  = Measured relative intensity of a (hkl) plane

D = Grain size

 $\eta$  = Equivalent microstrain $\beta$  = Diffraction-peak width

K = Shape coefficient

 $\lambda$  = Wavelength of the radiation beam (0.1506 nm for CuK $\alpha$  radiation)

a = Lattice constant

 $\rho$  = DensityA = Avogadro constant ( $6.02 \times 10^{23}$ )

M = Molar mass

V = Unit cell volume

 $\sigma$  = Induced stress

E = Young's modulus

 $\varepsilon$  = Macrostrain $\sigma_x$  = In-plane residual stress in a x direction $\sigma_z$  = Out-of-plane residual stress $d_{(002)}$  = Measured of lattice spacing for the (002) diffraction plane of the ZrN coating $d'_{(002)}$  = Standard lattice spacing for the (002) diffraction plane of the ZrN coating**Subsection 2.4**UO<sub>2</sub> = Uranium dioxide

UC = Uranium carbide

## Chapter 3

### Subsection 3.1.

ICDD = International Centre for Diffraction Data

### Subsection 3.2.

$T_h$  = Homologous temperature (the ratio of the melting point of a coating material to the deposition temperature)

$P$  = Working Ar pressure

## Chapter 4

### Subsection 4.3

$x$  = Root mean square of diffusion distance

$D$  = Diffusivity (diffusion coefficient or diffusion constant)

$t$  = Process time

### Subsection 4.4

$F_r$  = Induced rolling friction of a U-7Mo powder in drum

$M$  = Mass of a U-7Mo powder

$G$  = Gravitational acceleration (i.e.,  $9.8 \text{ m/s}^2$ )

$\alpha$  = The angle in-between a target and a U-7Mo powder in degree

$N$  = Normal force at the drum surface where the powder rolls down

$b$  = Coefficient of rolling friction depending on the surfaces

$r$  = Radius of a U-7Mo powder

$D$  = Diameter of a U-7Mo powder

$h$  = Distance between the drum center and target of the coating machine

$\theta$  = Emmission angle of coating vapors

$R$  = Radius of drum

$Y(\theta)$  = Sputtering yield distribution as a function of angular emission angle

$Y_{\max}$  = Maximum sputtering yield at  $\theta = 0^\circ$

$n$  = Dimensionless fitting parameter relying on the deposition parameters

$T(\theta)$  = Deposited coating thickness distribution as a function of angular emission angle

$T_{\max}$  = Maximum coating thickness for  $\theta = 0^\circ$

**Chapter 5****Subsection 5.1**

UTS = Ultimate Tensile Strength

**Subsection 5.3**

H = Hardness

$H_0$  = Hardness in the absence of grain boundary

k = Strengthening coefficient

d =- Grain size

$\alpha_f$  = Fracture strength

E = Young's modulus

$\gamma$  = Surface energy

c = Crack tip length.

$t_{ZrN}$  = Thickness of ZrN coating layer

$t_0$  = Maximum coating layer thickness in the absence of crack formation

S8RT = Eight nodes with reduced integration

**Subsection 5.4**

E = Young's modulus

$\nu$  = Poisson's ratio

$\alpha$  = Diagonal component of the Cauchy stress tensor matrix

$\gamma$  = Shear component of the stress tensor matrix

G = Shear modulus

t = Shear strain

$\tau$  = Thermal expansion coefficient

T = Temperature

## Chapter 1. Introduction

### 1.1. General research background

#### 1.1.1. Evolution of research and test reactor fuel

Research and test reactors (RRs), normally referred to as non-power reactors, are a type of nuclear reactor that mainly serve as a neutron source and irradiation tester rather than for power generation. Currently, more than 150 research reactors exist worldwide. Typically, RRs are operated at a low temperature (normally,  $<250^{\circ}\text{C}$ ) under atmospheric pressure, and for the safety of the reactor produce low power ranging from 0.01 to 250 MW [1]. This operation condition of an RR is significantly different from that of a power reactor (which has an operation pressure of 150 atm and a high temperature of above  $300^{\circ}\text{C}$ , and outputs 1 GW of power for pressurized water reactors, for example). The power level of an RR is controlled for its application [1], namely, 1) basic science and activation studies for low-power reactors (typically developed in universities), 2) irradiation studies on materials for high-power reactors, and 3) the testing of prototype fuel elements or coolants, or for a prototype mechanism production, and the production of medical isotopes for intermediate power reactors.

Since its first fabrication for use in nuclear weapons through the Manhattan project, highly enriched uranium (HEU) ( $^{235}\text{U}$  content of  $\geq 20\%$ ) has been utilized for civil applications as a part of the Atoms for Peace program. Because RR fuels generally require high fissile material densities to maximize the neutron flux and/or minimize the capital and fuel cycle costs, HEU with 70–95 wt.%  $^{235}\text{U}$  (normally  $> 90\%$   $^{235}\text{U}$ ) has been used as RR fuel in the form of  $\text{UAl}_x$ ,  $\text{U}_3\text{O}_8$ , or  $\text{UZrH}_x$  alloy of 1.7, 1.3, and  $0.5\text{ gU/cm}^3$  uranium loadings, respectively [2,3]. Most of the reactors built in the 1950s–1970s were designed to utilize HEU dispersion fuel plates.

However, HEU, which can be easily converted for use in a nuclear weapon, is not good from a non-proliferation standpoint. The United States (US), which normally supplied RR facilities and their HEU fuel to 41 different countries during the timeframe mentioned above, became worried about the non-peaceful use of HEU RR fuels. In particular, the entire fuel cycle takes approximately 4 years to complete in an RR, and approximately 5,000 kg of U-235 in total can be stored at each reactor [4].

Accordingly, as a non-proliferation activity, the Reduced Enrichment for Research and Test Reactor (RERTR) program was started in 1978 by the United States Department of Energy (DOE). The goal of this program is to replace HEU with low-enriched uranium (LEU;  $^{235}\text{U}$  content of  $<19.75\%$ ) in all existing RR facilities without significant financial or programmatic penalties [7–9]. The RERTR project has received significant attention and assistance worldwide, and has subsequently become an international cooperation project, with participation by Korea Atomic Energy Research Institute

(KAERI) in the Republic of Korea; Atomic Energy and Alternative Energies Commission (CEA) in France; Studiecentrum voor Kernenergie, Centre de l'Énergie Nucléaire (SCK·CEN) in Belgium; Technical University of Munich (TUM) in Germany; Mendeleev National Research Institute of Metrology (VNIIM), Research and Development Institute of Power Engineering (RDIPE), Institute of Physics and Power Engineering (IPPE), Novosibirsk Chemical Concentrates Plant (NCCP), and Radionuclide production at the Russia State Scientific Center (RIAR) in Russia; Canadian National Energy Alliance (CNEA) in Argentina; and Atomic Energy of Canada Limited (AECL) in Canada. Currently, the project is administered by the Office of Nuclear Material Threat Reduction within the National Nuclear Security Administration (NNSA). According to the aim of the RERTR program, LEU fuels replacing HEU fuels must satisfy the following criteria [5]:

1. The testing/experiment capability (i.e., neutron flux and core lifetime) of the reactors should be maintained without significant degradation;
2. Core lifetime should be sustained without a significant reduction;
3. No extensive reactor modifications and changes in fuel dimensions are required; and
4. No new or significant safety problems or licensing issues should be raised.

To meet criteria 1 to 3, LEU fuels should have the same total fissile atom (i.e.,  $^{235}\text{U}$ ) density as existing HEU fuels. Accordingly, LEU fuels should increase the charge volume of the fuel powders to compensate the decrease in  $^{235}\text{U}$  enrichment from HEU to LEU. There are two possible approaches to achieve high uranium loading without a dimensional change to existing RR fuels:

1. Alternative fuels of high intrinsic uranium density can be adopted; and
2. Fissile materials in the fuel zone (called fuel meat) can be increased in the volume fraction.

Candidate fuels are listed in Table 1. During the 1980s, by applying these two approaches, a  $\text{UAl}_x$  fuel powder/Al matrix ( $2.3 \text{ gU/cm}^3$ ),  $\text{U}_3\text{O}_8/\text{Al}$  ( $3.2 \text{ gU/cm}^3$ ),  $\text{UZrH}_x/\text{Al}$  ( $3.7 \text{ gU/cm}^3$ ), and  $\text{U}_3\text{Si}_2/\text{Al}$  ( $4.8 \text{ gU/cm}^3$ ) with increased uranium densities were qualified as a LEU dispersion fuel [8].  $\text{U}_3\text{Si}$  fuel, exhibiting an unpredictable growth behavior of the fission gas bubble, and hence significant swelling in the case of normal plate-type dispersion fuel, was approved for application to only rod-type dispersion fuels operated at a limited moderate temperature [10–12]. The inherent compressive stress of a rod-type fuel enables a strong swelling-suppression as compared to a plate-type fuel.

By 1988, approximately 90% of the RRs existing at that time were able to achieve HEU-to-LEU fuel conversion using  $\text{U}_3\text{Si}_2$  at  $4.8 \text{ g/cm}^3$ . However, high-performance reactors (also called high-power reactors or high-flux reactors) such as Advanced Test Reactor (ATR), Missouri University

Research Reactor (MURR), and National Institute of Standards & Technology Reactor (NBSR) require a high uranium density of greater than  $8.0 \text{ gU/cm}^3$  [12]. Thus, the development of alternative fuel materials was inevitable. Because the loading of dispersed fuel powders can reach up to  $\sim 55 \text{ vol.}\%$  within a fuel meat in the case of recent manufacturing techniques, the intrinsic uranium density of the fissile fuel powder itself must be beyond  $14.5 \text{ gU/cm}^3$  to reach the desired minimum uranium density of  $8.0 \text{ gU/cm}^3$  [12]. Accordingly, the development of new alternative fuels was inevitable.

Regarding the intrinsic uranium density, pure uranium of  $19.0 \text{ gU/cm}^3$  may be the best alternative fuel. However, pure uranium cannot sustain the gamma phase with a high irradiation stability at an RR operation temperature (commonly,  $<250^\circ\text{C}$ ). As shown in Figure 1, pure uranium has three crystalline phases below its melting point: an alpha phase ( $\alpha\text{-U}$ ), a beta phase ( $\beta\text{-U}$ ), and a gamma phase ( $\gamma\text{-U}$ ), at  $25\text{--}650^\circ\text{C}$ ,  $668\text{--}775^\circ\text{C}$ , and at temperatures beyond  $775^\circ\text{C}$ , respectively. In addition,  $\gamma\text{-U}$  shows an acceptable irradiation-growth behavior in contrast to the other phases (i.e.,  $\alpha\text{-U}$  and  $\beta\text{-U}$ ). The irradiation growth of a material is defined as its change in shape without a change in volume when no external stress is applied. In contrast to  $\gamma\text{-U}$  with an isotropic structure (i.e., body-centered cubic),  $\alpha\text{-U}$  and  $\beta\text{-U}$  with anisotropic crystal structures (orthorhombic structure for  $\alpha\text{-U}$  and tetragonal structure for  $\beta\text{-U}$ ) show directional irradiation growth, leading to poor dimensional stability during irradiation. During irradiation,  $\alpha\text{-U}$  expands in the  $[010]$  direction, and conversely shrinks in the  $[100]$  direction without any dimensional change in the  $[001]$  direction [13]. Unfortunately, at low operation temperatures of RRs (typically,  $<250^\circ\text{C}$ ), pure uranium exhibits only a thermodynamically stable  $\alpha\text{-U}$  phase, and no  $\gamma\text{-U}$  phase even when the  $\gamma\text{-U}$  uranium melt is quenched. At a low operation temperature of below  $250^\circ\text{C}$ ,  $\gamma\text{-U}$  thermodynamically decomposes into  $\alpha\text{-U}$  and  $\gamma'\text{-U}$  ( $\text{UMo}_2$ ).

Instead of pure uranium, there are two material types satisfying the required intrinsic uranium density (i.e.,  $\geq 8.0 \text{ gU/cm}^3$ ), namely,  $\gamma\text{-U}$  alloys containing a small amount of a  $\gamma\text{-U}$  phase stabilizer element such as Mo, Nb, Zr, and Cr, and  $\text{U}_6\text{M}$  ( $\text{M} = \text{Fe}$  or  $\text{Mn}$ ) intermetallics. Unfortunately,  $\text{U}_6\text{Fe}$  and  $\text{U}_6\text{Mn}$  intermetallic fuels show an uncontrolled acceleration in the swelling rate during irradiation, which is normally referred to as “breakaway swelling” [15–18]. Accordingly, only  $\gamma\text{-U}$  alloys can be utilized as a high-performance RR fuel material. In addition,  $\gamma\text{-U}$  alloy candidates need high gamma-stability (i.e., retarded  $\gamma \rightarrow (\alpha + \gamma')$  decomposition) at a low operation temperature, and a sufficient U-density for the required reactor performance. Such  $\gamma\text{-U}$  alloy candidates involving U-Mo, U-Mo-Pt, U-Mo-Sn, U-Nb-Zr, and U-Mo-Ru alloys have been assessed using in-pile irradiation tests (RERTR-1 and RERTR-2) and annealing tests for gamma-stability (Figure 2) [12]. These metallic fuels when applied as nuclear fuel are advantageous owing to a high thermal conductivity, safety when inactive, easy production, and easy spent fuel recycling [19–21]. Among the  $\gamma\text{-U}$  alloy candidates, U-Mo alloy containing a Mo element of 7–10 wt.% was selected as a next high-performance RR fuel material owing

to its excellent irradiation behavior, high intrinsic density (15.3 to 16.4 gU/cm<sup>3</sup>), and plethora of available irradiation records from fast reactor use [22–24].

U-Mo alloy is currently in the development and demonstration process for its qualification and eventual commercialization as a next advanced dispersion fuel for high-performance RRs. The irradiation performance of U-Mo alloys has been fully demonstrated with regard to the fabrication and characteristics of as-fabricated and irradiated fuel, as well as based on out-of-pile test results. A post-irradiation non-destructive examination (e.g., visual, neutron radiography, profilometry, and precision gamma scanning) and subsequent analyses are usually conducted to demonstrate whether a fuel satisfies the established requirements for the irradiation performance, including its expectable behavior and stability with regard to its mechanical properties and geometry.

### 1.1.2. U-Mo/Al fuel type

Depending on the form, U-Mo research reactor fuels can be divided into two general classes: flat-plate and cylindrical-rod fuels. As a research and test reactor fuel, flat-plate fuel is more advantageous than cylindrical-rod fuel because a thin plate geometry (typically, <1.5 mm) is favorable for removing heat for fuel safety during irradiation, although it is structurally weaker than a rod geometry.

Flat-plate U-Mo fuels are composed of a fueled zone and surrounding Al alloy cladding (normally Al-6061), as shown in Figure 3 (a). The fueled zone, normally called the “fuel meat” or “fuel core”, is the region where the fissile material (i.e., U-Mo) is filled. Depending on the configuration of the fuel meat, there are two fuel types, namely, dispersion and monolithic fuels: a composite form for dispersion fuel (Figure 3 (b)) and a foil form for monolithic fuel. Research and test reactors built prior to the RERTR program are typically designed to fit dispersion plate-type fuels. That is, dispersion fuels have a long usage history. As illustrated in Figure 3, a fuel meat, in which fissile U-Mo alloy powders of a tiny range in size (45–150 μm, but normally 45–90 μm) are dispersed into pure Al, Al-Si alloy, or an Al-Si mixture matrix, is metallurgically sandwiched between two Al alloy claddings.

On the other hand, monolithic fuel, which is a new U-Mo-fuel-plate design to achieve much higher fission densities, has been developed primarily by the US. A monolithic fuel, where a thin U-10wt.%Mo (U-10Mo) foil, is encapsulated in aluminum-alloy cladding. Compared to the dispersion-fuel design, the monolithic-fuel design is advantageous in that it easily achieves a high uranium density of above 8.0 gU/cm<sup>3</sup>, minimizing the contact area, and hence the undesired IL generation between the fuel and matrix during irradiation. U-10Mo/Al monolithic fuel plates has shown a promising irradiation performance.



Although dispersion fuel provides a lower uranium density compared to monolithic fuel, it has a long history (i.e., lots of available irradiation data), and has been shown to be more advantageous in terms of the manufacturing difficulty, thermal conductivity, and neutronic performance. Furthermore, high-energy fission events can occur within the matrix, which blocks the fission-induced structural, mechanical, and thermal degradation of the fuel plate. Moreover, dispersion fuels are structurally strong, enabling their utilization at up to a high burnup and in a high-power (high-neutron-flux) irradiation environment, which is an important requirement for fuels of high-performance RRs [24]. Hereafter, monolithic fuel will not be discussed in this dissertation.

### 1.1.3. Irradiation behavior of U-Mo/Al dispersion fuel plate

The qualification strategy of U-Mo fuel is nearly the same as in previous  $U_3Si_2$  fuel. At an early stage, as the power and burnup used in irradiation testing gradually increased, U-Mo fuel was qualified through irradiation tests.

From the point of view of reactor exploitation and fuel qualification, the most important behavior of a fuel plate is its swelling. As shown in Figure 4, the cooling gaps between fuel plates in a plate fuel assembly of a research reactor are considerably narrow (typically, 2–3 mm). The cooling gaps must be maintained to avoid fuel heatup during operation. Unfortunately, as shown in Figure 5, swelling of the fuel plate subsequently occurs mainly in the thickness direction, and thus the cooling gaps reduce with an increase in burnup. Typically, fuel swelling should not exceed 150–200  $\mu\text{m}$  in the thickness direction.

The swelling of solid fuels results from fission products (particularly, Xe atoms of a high yield) produced during a fission event, and is therefore inevitable. Based on the difference between the plate thicknesses before and after irradiation, the percentage of total swelling volume of U–Mo fuel can be obtained. For a U-Mo alloy fuel, the fuel swelling was correlated based on the measured fuel thicknesses depending on the fission density [8]. This correlation was based on post-irradiation examination (PIE) data from the changes in the thicknesses of the plates before and after irradiation. The total fuel swelling can be expressed as follows:

For  $f_d \leq 3 \times 10^{27}$  fissions/ $m^3$ ,

$$\left( \frac{\Delta V}{V_0} \right)_f = 5.0 \cdot f_d \quad (1)$$

For  $f_d > 3 \times 10^{27}$  fissions/ $m^3$ ,

$$\left(\frac{\Delta V}{V_0}\right)_f = 15.0 + 6.3(f_d - 3) + 0.33(f_d - 3)^2 \quad (2)$$

where  $\left(\frac{\Delta V}{V_0}\right)_f$  is the measured percentage of total fuel swelling, and  $f_d$  is the fission density at  $10^{27}$  fissions/ $m^3$ . The total fuel swelling consists of two elements, solid-fission-product induced swelling and gas-fission-product induced swelling. Solid-fission-product swelling shows the following linear function of the fission density (or burnup):

$$\left(\frac{\Delta V}{V_0}\right)_s = 4.0 \cdot f_d \quad (3)$$

where  $\left(\frac{\Delta V}{V_0}\right)_s$  is the solid-fission-product induced swelling in percentage. In addition, the gas bubble swelling (Eqs. (4) and (5)) can be calculated by subtracting the solid-fission-product swelling (Eq. (3)) from the total measured swelling (Eqs. (1) and (2)). The gas-fission-product induced swelling initially shows a linear increase with the fission density, and afterward exhibits a parabolic increase with the fission density, which is given as follows:

For  $f_d \leq 3 \times 10^{27}$  fissions/ $m^3$ ,

$$\left(\frac{\Delta V}{V_0}\right)_g = 1.0 \cdot f_d \quad (4)$$

For  $f_d > 3 \times 10^{27}$  fissions/ $m^3$ ,

$$\left(\frac{\Delta V}{V_0}\right)_g = 3.0 + 2.3(f_d - 3) + 0.33(f_d - 3)^2 \quad (5)$$

where  $\left(\frac{\Delta V}{V_0}\right)_g$  is the gaseous-fission-product induced swelling in percent. The measured fuel swelling data and prediction correlation are shown in Figure 6. The transition in the gas-fission-product swelling rate is due to gas-bubble agglomeration accompanying the microstructural evolution of the  $\gamma$ -phase of U-Mo, which is called “recrystallization”, “grain refinement,” or “grain sub-division” (see the upper images in Figure 6). The recrystallization originates from (1) the internal stress induced through the formation and agglomeration of (noble) fission gases, and (2) the generation and accumulation of lattice

defects by fission products with high kinetic energies during fission events. Before the recrystallization takes place, the fission gases exist in the form of 2–3-nm-sized nanobubbles inside a super lattice with a spacing of 6–7 nm, which was confirmed through a transmission electron microscopy (TEM) image analysis [25]. However, as the irradiation proceeds, fission gas bubbles increase in size from nanobubbles to microbubbles observable using a scanning electron microscope (SEM).

Figure 6 shows the microstructural change in the  $\gamma$ -phase of U–Mo fuel as a function of the fission density. The microstructural changes in the  $\gamma$ -phase of U–Mo fuel occur through three steps: pre-transition, recrystallization, and post-transition. In the pre-transition stage, at a low burnup (35% burnup,  $2.0 \times 10^{21}$  fissions/cm<sup>3</sup>), fission gas bubbles of 0.1  $\mu\text{m}$  in size appear locally along the pre-existing grain boundaries. Owing to the thermodynamic instability, grain-boundaries are typically a suitable place where micro-bubbles preferentially form. During the recrystallization stage at an intermediate burnup (65% burnup,  $4.8 \times 10^{21}$  fissions/cm<sup>3</sup>), as the bubble population in the grain boundaries, and the accumulated defects, increase, grain recrystallization occurs, and consequently the average grain size decreases. That is, during this stage, additional grain boundaries are newly generated. The bubbles along the pre-existing grains spread out into the newly formed grain boundaries. During the post-transition stage at a high burnup (80% burnup,  $5.6 \times 10^{21}$  fissions/cm<sup>3</sup>), bubbles are uniformly scattered over the entire fuel as the grain refinement is nearly completed.

Moreover, the fuel swelling should not only be quantitatively restricted, it should also have a gradual swelling rate as a function of the burnup. Conversely speaking, unmanageable accelerations in the swelling rate, referred to as “breakaway swelling”, are unacceptable. At low power and burnup, U–Mo/Al dispersion fuel plates have shown a high irradiation performance at low power and burnup. However, some U–Mo/Al dispersion test fuel plates have failed through induced breakaway-swelling at high power and burnup [27, 28], even though they exhibited stable irradiation swelling prior to the breakaway swelling [28].

The PIE results showed that the breakaway swelling is associated with the fuel amorphization through the generation of an amorphous interaction layer (IL) between U-Mo fuel powders and Al matrix. The IL, originating from the interdiffusion of U-Mo and Al atoms, mainly through the ballistic effect of fission events during irradiation, typically exhibits an amorphous nature owing to the lattice defects produced through high-energy fission events. At low RR irradiation temperatures (typically <250 °C), the generated lattice defects cannot be recovered and are accumulated [30–32].  $\text{UAl}_x/\text{Al}$  [29] and  $\text{U}_3\text{Si}_2/\text{Al}$  [31, 32] dispersion fuels also generate amorphous IL during irradiation. Although amorphous IL, and even the fuel material itself, found in irradiated  $\text{UAl}_x/\text{Al}$  [29] and  $\text{U}_3\text{Si}_2/\text{Al}$  [31, 32] dispersion fuels does not inevitably lead to a poor irradiation behavior of the fuels, an amorphous interaction of some fuels involving U-Mo,  $\text{U}_3\text{Si}$  (in the case of plate-type fuel),  $\text{U}_6\text{Fe}$  [17] or  $\text{U}_6\text{Mn}$  [14]

can give rise to the breakaway swelling owing to their weakened interfaces in the IL and Al matrix by the agglomerated large fission-gas-bubbles.

Owing to the low retention for noble fission gases, fission gas bubbles in U-Mo/Al amorphous IL are easily agglomerated into huge crescent-like cavities (i.e., highly concentrated gas-fission-products) at the IL-matrix interface or at the IL-IL interface in locations where the entire Al matrix is consumed, as shown in Figure 7. In general, amorphization of crystalline materials generally increases the lattice spacing and volume, leading to an increase in atomic mobility and diffusion, and thus a low retention for the fission-gas products in them. The fission-gas product agglomeration of amorphous IL, called “snowploughing” or “sweeping,” has been detected in irradiated dispersion fuels [33, 34]. It is believed that an excessive internal stress induced in the pores causes a mechanical deformation of the fuel plate, resulting in a cladding bulge (called “pillowing” or “blistering”) and even fuel-plate failure (i.e., fuel-plate rupture). For all plates applied in all experiments, the matrix is typically found to decrease to volume fractions of <10% in locations where indications of a fuel failure are visible.

In addition to breakaway swelling through fission-gas agglomeration, U-Mo/Al IL causes unfavorable effects such as a reduction of the cladding layer thickness, and the generation of IL phases with a relatively low thermal conductivity, low melting point, and different thermal expansion from the adjacent U-Mo fuel powder and Al matrix. Metallurgical interactions between the U-Mo fuels and Al alloy can arise during processing and irradiation [22, 35–41]. A number of studies [7, 15, 16, 22, 23, 42–44] have been conducted to characterize U-Mo/Al IL. It has been empirically revealed that IL consists of  $UAl_2$ ,  $UAl_2$ ,  $UMo_2Al_{20}$ , and  $U_6Mo_4Al_{42}$  for an out-of-pile annealing test [45–49], and is a  $(U-Mo)Al_x$  form where  $x$  varies with an irradiation power/temperature of  $x = 3-4$  for high irradiation powers of FUTURE and IRIS-3, and  $x = 6-7$  for low powers of IRIS-1 and IRIS-2 [10, 28].

In addition, dispersion fuel plates of UMo/Al have shown a higher IL formation rate than those of  $U_3Si_2/Al$ , and UMo/Al IL occupies extremely large volume fractions of the fuel meat (e.g., 45–50% for the IRIS2 irradiation test, and a maximum of 70% at the greatest burnup/power spots for the FUTURE irradiation test). For U-Mo and pure aluminum, the IL growth under the in-pile condition is given as follows:

$$Y_{IL,0}^2 = 2.6 \times 10^{-8} \dot{f}^{1/2} \exp\left(-\frac{32009}{RT}\right) t \quad (6)$$

where  $Y_{IL,0}$  is the IL thickness in  $\mu m$ ,  $\dot{f}$  is the fission rate (fissions/cm<sup>3</sup>·s),  $R$  is the ideal gas constant (8.314 J/mol/K),  $T$  is the temperature of fuel meat in Kelvin, and  $t$  is the processing time. The equation was modified from the Arrhenius equation to additionally consider the athermal fission-enhanced diffusion factor along with the thermal diffusion.

Additional correction factors (Si addition into the Al matrix and Mo content in the U-Mo fuel) accounting for fission-enhanced diffusion, fitted from the irradiation data, can be expressed as follows:

$$Y_{IL} = Y_{IL,0}^2 \cdot f_{Si} \cdot f_{Mo} \quad (7)$$

with

$$f_{Si} = (1.212 - 6.2 \times 10^{-4} T) \cdot \exp[-(10.333 - 2.1 \times 10^{-2}T)W_{Si}] + (6.2 \times 10^{-4} T - 0.201) \cdot \exp[-(8.1 \times 10^{-4}T - 0.302)W_{Si}]$$

$$f_{Mo} = 1.35 - 0.05W_{Mo}$$

where  $Y_{IL}$  is the IL thickness considering additional correction factors,  $f_{Si}$  and  $f_{Mo}$  are the correction factors for Si content added into the Al matrix, and the Mo content of the U-Mo fuel, respectively; and  $W_{Si}$  and  $W_{Mo}$  are the Si content in the Al matrix, and the Mo content in the U-Mo alloy fuel, in weight percentage.

If the volume fraction of IL stays sufficiently low, the U-Mo/Al fuel will show an acceptable irradiation behavior. The RERTR international program has started to recognize U-Mo/Al IL as the main drawback to be solved. Several remedies to suppress U-Mo/Al IL growth during fabrication and irradiation have been suggested and evaluated as follows:

1. The addition of a third alloying element to U-Mo to form a U-Mo-X ternary alloy (X, such as Zr and Ti) [45–47];
2. The addition of 2–5 wt.% silicon to the aluminum matrix [29, 36, 45, 53–55];
3. A change in the matrix material from Al to Mg possessing a negligible solubility and no intermetallic compound with respect to U-Mo (i.e., Mg that has no reaction potential with U-Mo) [58–61]; and
4. Coating of U-Mo with Si or ZrN to provide a diffusion-barrier layer between U-Mo and Al [37, 40, 56, 57, 61–64].

It was identified from the PIE results of U-Mo/Al dispersion fuel plates that remedy 1 showed no big benefit, while remedy 2 were somewhat effective in reducing the IL quantity. However, it has been reported that these remedies cannot perfectly suppress the pillowing problem at high burnup. In the E-FUTURE irradiation results, two of four UMo/Al-(4.1–6.0)wt.%Si dispersion fuel plate samples had been pillowed (that is, severely deformed) [64]. Moreover, the usage of even a small amount of silicon in nuclear fuel is not desirable from a fuel reprocessing viewpoint since Si-contained fuel is more sticky and tends to clog the reprocessing stream than non-Si fuel plate. Accordingly, the processor needs to refresh the process line with a non-Si fuel plate every 10 Si-contained fuel plates. In addition,

remedies 3 and 4 were proposed, and have been studied as alternatives. The Mg usage of remedy 3 is dangerous to be applied to RR fuels since Mg, as an alkali metal, is explosive in air and water. If coolant reaches a U-Mo/Mg fuel meat through a small opening in the cladding, the violent reaction with the Mg matrix and coolant, resulting in the RR accidents. Furthermore, Mg is not compatible with generally-used Al-based alloy claddings. Accordingly, remedy 4 is the best method so far, and thus has been actively studied, especially by the Surface Engineered Low Enriched Uranium Molybdenum Fuel (SELENIUM) international-cooperation project [37, 40, 56, 57, 62]. My study also focuses on ZrN diffusion barrier coating.

## 1.2. Application of diffusion barrier into U-Mo/Al dispersion fuel

### 1.2.1. Deposition methods for a diffusion barrier coating on U-Mo fuel powders

As a thin-film deposition technique for U-Mo dispersion fuel powders, magnetron sputtering, chemical vapor deposition (CVD), and atomic layer deposition (ALD) have been developed. The unique advantages and disadvantages of each the coating deposition technique are summarized in Table 2.

The first deposition technique, magnetron sputtering, is a type of physical vapor deposition (PVD) in which atoms are ejected from the target by striking the target with positively-charged Ar ions generated in plasma, and then condense on a substrate surface. For powder-type substrates like U-Mo powders used in this study, sputtering techniques involving magnetron sputtering, ion-assisted deposition, dual-ion beam sputtering, and ion plating are typically used [65]. To obtain a homogeneous thickness of the resultant sputtered coating layer on a powder-type substrate, it is necessary to continuously mix the substrate powder during sputtering since sputtered coating atoms or molecules are generally transported in a line-of-sight trajectory from the target to the substrate. Therefore, magnetron sputtering machines for U-Mo powders possess a mixing component: tunable drum for a non-reactive sputtering machine used in this paper and the RF reactive sputtering machine called the “STEPS & DRUMS” (the Sputtering Tool for Engineering Powder Surface and Deposition Reactor; at SCK-CEN), and oscillating shaker operated in magnetic fields for a DC non-reactive sputtering machine (at TUM). The STEPS & DRUMS is illustrated in Figure 8. Magnetron sputtering technique is explained in more detail in the next section (section 1.2.2).

The second deposition technique, CVD, encompasses all deposition techniques using chemical reactions in a gas phase to form coatings. In general CVD, one or more chemical vapor precursors react and/or decompose on the exposed surface of a substrate to create the wanted deposit. In order to achieve the sufficient energy for the chemical reactions, CVD is normally operated at raised temperatures in contrast to PVD and ALD. In addition, volatile by-products are normally generated, which are eliminated by gas flow in the reaction chamber. For U-Mo dispersion fuel powders, pack-cementation, CVD-equipped with a substrate mixer, and Fluidized Bed CVD (FB-CVD) have been used to fabricate a single coating layer of uranium silicide (U-Si), uranium nitride (U-N), and ZrN, respectively. These CVD machines were presented in Figure 9.

The last deposition technique, ALD actually belongs to CVD. Unlike other CVD methods, ALD is a cyclic process consisting of two or more separate chemical reactions. Each the separate reaction is self-restricting, which allows certain advantages such as extremely precise coating-thickness, high coating conformality, and pure coating containing less impurities than coatings produced by other CVD

methods. On the other hand, ALD's disadvantage is the very low deposition speed (a monolayer per cycle) and hence expensive.

As a possible candidate deposition method to create a ZrN diffusion barrier coating layer on U-Mo powders, magnetron reactive sputtering, FB-CVD, and ALD have been developed. Until now, only the ZrN coating, deposited by the "STEPS & DRUMS" (i.e., a reactive sputtering machine), have reported irradiation test results [36, 66]. As another ZrN coating deposition method, FB-CVD and ALD have been studied over the last years by INL and CEA (the former), and ANL (the latter) [67]. By using a FB-CVD machine, tri-layers of uranium oxide (U<sub>2</sub>O<sub>3</sub>) / zirconium oxide (ZrO<sub>2</sub>) / zirconium nitride (Zr<sub>3</sub>N<sub>4</sub>) were fabricated on U-8wt.%Mo atomized powders at 280°C by the chemical reaction between the used precursor carrier (dimethylamino zirconium) and fluidization gas (N<sub>2</sub>+H<sub>2</sub>) [67]. The multiple coating layers showed a very low deposition-rate of 1.1 μm/day, and could be fabricated up to 2.4 μm coating thickness. In addition, by a modified ALD machine, Savannah 200 (Figure 10), a ZrN thin coating was produced on U-Mo dispersion fuel powders. The Savannah 200 machine, operated in a hot wall reactor with a temperature between 235°C and 245°C, is a batch powder coating machine applying the chemical precursors of ammonia (NH<sub>3</sub>) and Tetrakis (dimethylamino) zirconium (TDMAZr), together with a nitrogen (N<sub>2</sub>) carrier gas. The as-fabricated ALD ZrN coatings showed an epitaxial structure and possessed a very low level of chemical impurities unlike normal CVD methods.

These deposition methods have their own advantages and disadvantages as listed in Table 2. That is, all the deposition methods are not perfect. For example, ALD's the biggest obstacle is the fact that it is very time consuming and expensive. So, if magnetron sputtering method shows comparable results, if not all the same, it can be more attractive.



### 1.2.2. Magnetron sputtering

Ever since magnetron sputtering technique was first pioneered in 1852 and then commercialized during the 1960s and 1970s, it has rapidly developed, and has become the main method for deposition to meet the demand for high-quality functional coatings used in various fields of industry. Its major applications are its use in diffusion barriers, and as corrosion-resistant, hard, low-wear, friction-resistant, decorative, optical, and electrical coatings [68].

The primary advantages of magnetron sputtering deposition are as follows:

1. Fast production rates;
2. Compatibility with various metals, alloys, or compounds;
3. Compatibility with heat-sensitive substrates;
4. High-purity of as-fabricated coatings;
5. Remarkably strong adhesion between the substrate and as-fabricated coating;
6. Excellent uniformity for an extensive and uneven substrate surface; and
7. Ease of automation.

The magnetron sputtering is a type of sputtering operated under a plasma environment made by applying hundreds of volts using a direct current (DC) or radio frequency (RF) power source in a working gas (typically, argon gas) atmosphere. For compound coatings such as nitrides and oxides, magnetron sputtering can be divided into two types depending on the deposition principle: “non-reactive sputtering” and “reactive sputtering”. In the SELENIUM project, a ZrN coating layer has been deposited on the U-7Mo particles by a reactive magnetron sputtering system equipped with a barrel called the “STEPS&DRUMS” [37, 40, 56, 63, 64, 67]. However, a ZrN coating layer can also be fabricated by using a non-reactive sputtering system. Non-reactive sputtering is a process in which compound coating molecules are directly sputtered onto a substrate from the compound target. In contrast, reactive sputtering is a process in which compound molecules to be deposited are formed through chemically interacting sputtered metal target atoms (e.g., Zr for ZrN coating) with an applied reactive gas (e.g., nitrogen gas for ZrN coating) prior to deposition on the substrate. The resulting reactively-sputtered coatings are changeable in terms of their composition and stoichiometry depending on the ratio and quantity of the inert and reactive gases. Generally, group IV transition metal nitrides including ZrN have a large variety of stoichiometries of  $x < 2$ . For zirconium nitride, a nitride phase of  $ZrN_{1-x}$ , exists for the N/Zr ratio  $< 1$ , while a ZrN solid phase and  $N_2$  gas phase exist in the absence of super-stoichiometric nitrides for the N/Zr ratio  $> 1$ . Therefore, reactive sputtering has a relative difficulty

sustaining the composition and stoichiometry of the resulting coating because of its sensitivity to the gas condition, and is also likely to make a less dense coating structure than non-reactive sputtering owing to the relatively higher working pressure, although it can create a compound coating through the use of a cheap corresponding metal target, and control the stoichiometry of the resultant coating. So, in this study, a ZrN coating layer was deposited on U-7Mo dispersion fuel powders by a non-reactive sputtering machine. In Figure 11 and Table 3, the schematic and deposition condition of two sputtering machines of this study and SCK-CEN are compared. Both the machines employ a barrel (turnable drum) as a substrate mixer to create a uniform coating layer on a U-Mo substrate powder.

If a high voltage is applied to a magnetron sputtering machine, a closed magnetic field is generated and then allows the initial ionization process for plasma formation by trapping free electrons. The induced plasma consists of pure Ar, positively charged Ar ions (i.e., Ar cation), and free electrons. The Ar positive ions are accelerated through the electrical attraction of an anode of thousands of electron volts physically in contact with the back of the target. The accelerated Ar positive ions strike the negatively charged target with the significant kinetic energy (from a few tens to hundreds of electron volts) sufficient to eject the coating atoms/molecules from the target. The ejected coating atoms/molecules are sputtered into the substrate surface facing the target with a line-of-sight cosine distribution, and then reach on a substrate surface.

A coating layer grows through the following steps:

1. **Adatom migration on substrate surface:** The reached coating atoms/molecules are physically adsorbed on the substrate, and so are called “adatoms”. They may be diffusible with a certain degree of freedom in diffusion, which is influenced mainly by their binding force and deposition temperature (i.e., substrate surface’s temperature during deposition). For adatoms with strong bonding strength or at very low deposition temperatures, the adatoms are hard to move. In contrast, adatoms with weak bond strengths or at higher temperatures are able to diffuse on the substrate surface (surface- or 2D-diffusion), or even into the substrate lattice (bulk- or 3D-diffusion). The adatoms continue to move until they reach a position that minimizes the total energy.
2. **Nucleation:** After a certain time of adatom diffusion, the adatoms are condensed into clusters (named nuclei) which is energetically more favorable. Then, the nuclei grows through various mechanisms. Van der Merwe mechanism describes the method where the atoms cover the whole surface before a second layer is grown. If the nuclei grow as hemispheres and a thin film is formed once the hemispheres have grown large enough to touch

each other, then it is referred to as the Volmer-Weber mechanism. If the growth process is a combination of the two by covering the surface first and then growing by hemispheres, it is referred to as the Stranski-Krastanov mechanism. The nuclei is initially in a metastable state, but once it reaches a critical size, it will become energetically stable and fixed.

3. **Calescence:** As the randomly positioned nuclei increase in size into islands, the islands will be located close to each other. Once the spacing between any two nuclei or islands is within a critical distance, they will move toward each other and coalesce into a single entity. With the continued growth, there will be coalescence of several nuclei and islands into more complex shapes, resulting in a network (channel) of interconnected islands containing lots of holes (uncovered substrate regions). Larger islands grow together, leaving channels and holes of uncovered substrate. However, with continuous deposition, the holes will continue to shrink until the coating becomes complete and is continuous. Once the surface is completely covered, the coating thickness will then increase and the coating crystals with a variety of orientations can grow.

By understanding and controlling above the microscopic coating growth processes, desired coating mirostructures for specific technological applications can be fabricated. Generally, the coating growth processes and consequently coating microstructure are dependent on the deposition method and deposition environment (deposition parameters), affecting the coating growth processes. Extensive studies of the correlation between the microstructure of deposited coatings and the related deposition parameters have been carried out in the past decades.

A well-known model showing the relationship between two deposition parameters (deposition temperature in homologous temperature, and Ar working gas pressure in mTorr) and resulting sputtered coating's morphology is Thornton's structure zone model (SZM) [70], depicted in Figure 12 (a), which categorizes the coating morphology as a function of the two parameters. The SZM has been developed based on a morphological examination of as-fabricated metal sputtered coatings. According to the SZM, with an increase in the deposition temperature and a reduction in the Ar working pressure, the resulting coating microstructure changes from a porous fine columnar structure to a dense equiaxed structure similar to that of a bulk material due to a change in the adatom's kinetic energy and hence activated diffusion mechanism from surface diffusion to volume (bulk) diffusion.

Typically, sputtering machines are operated at low deposition temperatures (normally,  $\sim 300^\circ\text{C}$ ), corresponding to the homologous temperature ( $T_s/T_m$ )  $< 0.3$ , where  $T_s$  and  $T_m$  are the substrate temperature and the coating material's bulk melting temperature both in Kelvin. Thus, sputtered coatings typically have a porous fine columnar structure (denoted as "Zone I structure") through the

adatom's limited surface diffusion, or a densely packed V-shaped columnar structure (denoted as "Zone T structure") through the adatom's competitive surface diffusion. In addition, in order to fabricate a denser sputtered coating, sputtering is commonly operated at a low deposition pressure (normally called "working pressure") to reduce the background gas (e.g., Ar, O<sub>2</sub>, and N<sub>2</sub>)'s deleterious effects: (1) making the resulting coating more porous by inducing an energy loss of the sputtered atoms/molecules; and (2) causing the incorporation of the background gas inside the coating.

### 1.3. Literature review of Zirconium nitride (ZrN) coating

#### 1.3.1. General application in fields other than nuclear field

Among group IV transition metal nitrides, ZrN possesses a combination of suitable chemical, thermal, mechanical, optical, and electromagnetic characteristics such as excellent erosion resistance, su high thermal stability perior, abrasion resistance, and beautiful appearance (ZrN coatings deposited by a PVD method exhibit attractive light-gold color.), as summarized in Table 4. So, ZrN coating has been used for a long time in a diverse range of industrial applications as: 1) diffusion barrier coating and electrical contacts in electronics industry; 2) abrasion resistant and hard coating for components and devices (e.g., cutting tools, medical devives, and atutomotive and aerospace components subject to high wear environments); 3) high temperature oxidation-resistance coating; and 4) decorative coating. In all of these applications, the deposition of an inert ZrN coating has resulted in a better performance, extended life, and higher reliability of the applied products.

#### 1.3.2. Application as a diffusion barrier in U-Mo/Al dispersion fuel plate

As mentioned before, one promising remedy to suppress the formation of deleterious U-Mo/Al IL is applying a ZrN diffusion barrier layer on U-Mo powders. The excellent barrier material (X) for U-Mo/Al fuels should satisfy the following conditions [61, 68, 69]:

1. Low mass transport rate of U-Mo and Al across X;
2. Low mass transfer (or loss) rate of X into U-Mo and Al;
3. High thermodynamic stability against U-Mo and Al. Even If any intermetallics are formed, they should be stable during irradiation;
4. High thermal conductivity;
5. High fracture-resistance under internal and external stresses;
6. Compatibility with dispersion-fuel plate manufacturing process (typically a rolling method);
7. Acceptably low absorption cross section for thermal neutrons (i.e., low neutron loss); and
8. Free of reprocessing issues.

Together with transition metals (e.g., Zr [61, 69–71], Mo [64, 69, 70], Ti [61, 72], and Nb [61, 69] and intermetallic compounds (UO<sub>2</sub>, [75, 76], U-Si [77, 78], U-N [77, 78]), ZrN [37, 40, 56, 63, 64, 67] satisfying the above criteria have been applied as a diffusion barrier material to U-Mo/Al dispersion fuel plates. As summarized in Table 4, ZrN possesses desired properties as a diffusion barrier in U-

Mo/Al system such as high thermodynamic and chemical stability, a high hardness (i.e., high fracture-resistance), and a low thermal-neutron absorption cross-section.

Accordingly, ZrN was chosen as a promising diffusion barrier material for U-Mo/Al dispersion fuels. The effectiveness of a ZrN thin coating layer was assessed by an irradiation test at the MIR reactor in Russia from 2008 to 2010. A pin-type dispersion fuel containing 2–3  $\mu\text{m}$ -thick ZrN coated U-9wt.%Mo dispersion fuel particles and an almost pure Al matrix (Si content of <0.4wt.%) were irradiated up to very high burnups [80]. The PIE results showed that a 2–3  $\mu\text{m}$ -thick ZrN coating layer successfully suppressed the U-Mo/Al IL growth (the IL accounted for 6 vol.%) at a high average burnup of 85%  $^{235}\text{U}$  [80].

Based on the good irradiation performance of ZrN coating, the SELENIUM project selected ZrN as a promising diffusion barrier for plate-type U-Mo/Al dispersion fuels. In order to determine the desired thickness of a ZrN coating layer between the U-Mo fuel and Al matrix, a simulation was performed by using the Transport of Ions in Matter (TRIM) program. The simulation result showed that 1  $\mu\text{m}$  was the minimum ZrN coating thickness to sufficiently prevent the intermixing between U-Mo fuel particles and an Al matrix by the ballistic collisions of high-energy fission products [37, 40]. However, the simulation results (i.e., a 1  $\mu\text{m}$  coating thickness) do not consider the coating microstructure and multiple displacement process by energetic fission products.

In the SELENIUM project, a single coating of ZrN with a thickness of 1  $\mu\text{m}$  has been deposited onto U-7Mo dispersion fuel powders by utilizing the STEPS & DRUMS (a RF magnetron reactive sputtering machine) at SCK·CEN [40, 58, 67]. The as-fabricated ZrN coated U-Mo powder has been actively studied on the evaluation of the diffusion barrier performance by various tests and microstructural characterization.

To assess the diffusion barrier performance of a 1  $\mu\text{m}$  thick ZrN reactively-sputtered coating in U-Mo/Al system, an annealing test [59], a heavy-ion irradiation test [60], and an in-pile irradiation test [36] were carried out. All test results verify that a 1- $\mu\text{m}$  thick ZrN coating is very effective in limiting the growth of the U-Mo/Al IL if it is structurally intact. However, near the damaged ZrN coatings, a huge U-Mo/Al IL was observed in an annealed U-Mo(ZrN)/Al cylindrical compact sample [59] and irradiated U-Mo(ZrN)/Al dispersion fuel samples [37, 57]. The heavy-ion irradiation test with 80 MeV iodine ions for ZrN-coated U-Mo fuel showed IL layer growth at the site where the coating was damaged [60]. Moreover, a full-sized dispersion fuel plate (the SELENIUM plate called U7MD1231) irradiated up to a fission density of  $\sim 5.0 \times 10^{27}$  fission/cm<sup>3</sup> [36] also showed extensive and local ILs, as depicted in Figure 13 (b) and (c). The localized large ILs near the damaged coating showed a distinct difference from the thin IL near the intact ZrN coating (Figure 13 (a)). Likewise, the structural integrity of the ZrN diffusion barrier coating is the most important factor in determining its diffusion barrier capability. It was suspected that the coating damage had occurred during the dispersion-fuel-plate

fabrication. Indeed, among the EMPIRE ((European Mini-Plate IRradiation Experiment) mini-plates and SEMPER FIDELIS full-sized plates, all the as-fabricated dispersion fuel plates, containing PVD ZrN coated U-7Mo powders, showed severe delamination parallel to the rolling direction, and radial cracking of the ZrN coating [81]. It was guessed that the coating delamination was caused by the high hardness (i.e., poor plastic deformability) of un-annealed U-Mo powders, and, on the other hand, the radial cracking probably originated from the deformation incompatibility between the coating and U-Mo substrate during the fuel plate fabrication (particularly, during high temperature heating) as suggested in [61]. Thus, for an acceptable functional performance, the ZrN coating should not break during the dispersion-fuel-plate fabrication. However, there have been no studies scientifically investigating the ZrN coating's structural integrity in a manufacturing process that may damage the coating layer, and hence no clear criteria to prevent the coating damage have been proposed.

Furthermore, to understand the ZrN coating's fracturing behavior (damage formation) as well as diffusion barrier performance, the microstructure affecting the fracture-resistance should be examined first. The analysis results of the ZrN coating microstructure are summarized in Table 5. One of the prominent features of the ZrN coating is the fact that the coating microstructure changed depending on two parameter, coating thickness and U-Mo powder. It was identified by TEM image analysis that the coating's compacting density changed along the coating thickness (the first parameter) [62, 75]. As shown in Figure 14, a dense-to-porous structural transformation of the coating was found at a coating thickness of 0.2  $\mu\text{m}$ , beginning to form V-shaped column-boundary-gaps among the coating columns. That is, a 1- $\mu\text{m}$  thick ZrN coating was composed of two regions, a dense inner region of below 0.2  $\mu\text{m}$  in thickness, and a porous outer region starting from a thickness of 0.2  $\mu\text{m}$ . The TEM-EDS point and mapping analysis results (Figure 14 (b)) of the coating identified that the porous outer coating had a relatively higher oxygen contents than the dense inner coating [62, 75]. In addition, it was observed that the coating thickness itself was varied depending on the U-Mo substrate powder (the other parameter) although the coating layer of each U-Mo powder was uniform in thickness [62, 68, 75]. The as-fabricated ZrN coatings showed an extensive thickness distribution: 0.8–1.5  $\mu\text{m}$  for average 1  $\mu\text{m}$ -thick coatings [61], 0.6–2.2  $\mu\text{m}$  for average 1.2  $\mu\text{m}$ -thick coating [69], 0.8–1.7  $\mu\text{m}$  for average 1.2  $\mu\text{m}$ -thick coating, 0.9–2.0  $\mu\text{m}$  for average 1.4  $\mu\text{m}$ -thick coating, 1.6–2.5  $\mu\text{m}$  for average 2.0  $\mu\text{m}$ -thick coating, 1.0–2.0  $\mu\text{m}$  for average 1.4  $\mu\text{m}$ -thick coating, 0.7–1.4  $\mu\text{m}$  for average 1.1  $\mu\text{m}$ -thick coating, 1.1–2.4  $\mu\text{m}$  for average 1.7  $\mu\text{m}$ -thick coating [81]. (In my research, it has been proven experimentally that the thickness of ZrN non-reactively sputtered coatings depends actually on the U-Mo substrate size.) Likewise, average 1  $\mu\text{m}$ -thick ZrN reactively sputtered coatings showed different microstructures depending on the coating thickness and U-Mo substrate powder. Therefore, as written in Table 5, to understand the realistic microstructure of the ZrN coating, the comprehensive microstructural studies

should be performed as a function of the coating thickness and U-Mo substrate powder. Unfortunately, there is no parametric study of the ZrN coating microstructure.

As well as the RF magnetron reactive sputtering mentioned above, other deposition methods (i.e., ALD and FB-CVD) to form a ZrN coating layer on U-Mo powders have been studied over the last years. Only the ZrN coating deposited by magnetron sputtering has irradiation test data, but the irradiation performance of the ZrN coating layer deposited by the other methods has not yet been revealed. The EMPIRE test recently conducted at the ATR in the US will show the effectiveness of ZrN coatings deposited on U-Mo dispersion fuel powders by different coating deposition methods in suppressing the U-Mo/Al IL growth. The selected coating deposition methods were magnetron sputtering deposition developed by SCK-CEN (Belgium), and ALD developed by the ANL (US). In addition to the EMPIRE test, the SEMPER-FIDELIS test at the Belgian Reactor 2 (BR-2) in Belgium is currently underway to verify the benefits of the ZrN magnetron reactively-sputtered coating on the swelling behavior of U-Mo/Al dispersed fuels. In this research, only the results of the ZrN reactively-sputtered coating deposited in a similar manner to the deposition method used in this study will be considered.



## 1.4. Damage to ZrN coating within U-Mo/Al dispersion fuel plates

As mentioned before, for diffusion barriers to operate properly in U-Mo/Al dispersion fuel plates, their structural integrity must be maintained during all post-deposition processing (i.e., dispersion fuel plate fabrication). In this subsection, the observed structural failure of ZrN coating applied to U-Mo/Al dispersion fuel plates was discussed.

### 1.4.1. Possible causes

As illustrated in Figure 15, dispersion fuel plates are typically fabricated through a sequence of steps including mixing, compaction, assembly, welding, hot-rolling with multiple heating normally at 500°C, blister testing normally at 500°C, cold-rolling at room temperature, trimming, and inspections in that order [8]. Considering these fabrication steps, it has been predicted that a single coating layer deposited onto U-Mo fuel powder can be damaged through the excessive stresses induced during the manufacturing step. Indeed, the ZrN coating damage could be confirmed in heavy-ion irradiation test results [60] and the SELENIUM irradiation test results [36]. The driving source for the ZrN coating damage is believed to be the fabrication processing of a dispersion fuel plate [37, 56, 57]. It is suspected that the manufacturing process causes the ZrN coating cracking by (1) thermal stresses induced by the mismatch of the coefficient of thermal expansion (CTE) between the ZrN coating and U-Mo substrate powder during the heat-treatment processing, and/or (2) external mechanical stresses during the compacting or hot/cold rolling processing. In this research, focus is given to the thermal stress as the driving source for a ZrN coating failure.

The fabrication process of dispersion fuel plates typically involves several heat treatments before each hot-rolling step and during the blister test. The heat-treatment temperature is determined based on the ductility of the cladding material. A fuel meat is typically clad with a hard aluminum alloy 6061 (AA6061), which is fabricated normally at 500°C. As an exception, the SELENIUM plates clad using AG3NET (AA5754) were produced below 450°C [60]. The total heating time is approximately 2 h. During the heating steps, thermal stress is induced through a CTE mismatch between the coating material and U-Mo fuel. Under high-temperature conditions of the heating processes, the generated thermal stress over the coating can cause a loss of the structural integrity of the coating layer. Many studies have been conducted to investigate the coating failure based on the thermal stress [76–81]. When the CTEs of a coating layer and a substrate are significantly different, the coating fracture and/or delamination are attributable to the thermal stress induced. In this regard, the thermal stress occurring during heat treatment should not exceed the mechanical strength of the coating to sustain the structural integrity of the coating. Unfortunately, only a few studies have evaluated the effects of

induced stresses on the ZrN coating cracking during heat treatment. For the successful utilization of ZrN coating, it is essential to examine how stresses are generated in the coating and affect the coating integrity during fabrication. In addition, guidelines for optimizing the coating design and heat-treatment process conditions should be provided.

#### 1.4.2. Impacting on diffusion barrier performance

In a diffusion-limited process, the root mean square of diffusion distance ( $x$ ) can be expressed as follows [89]:

$$x = \sqrt{D \cdot t^2} \quad (8)$$

where  $D$  is the diffusivity, and  $t$  is the process time. Applying the equation to the case of a diffusion barrier coating,  $x$ , and  $t$  can be interpreted as the thickness and lifetime of the coating, respectively, and  $D$  can be treated as the diffusivity (diffusion coefficient or diffusion constant) of a passing solid material in the coating. According to the equation, the lifetime ( $t$ ) of a diffusion barrier coating is linearly proportional to the coating thickness ( $x$ ). On the other hand, the diffusivity ( $D$ ) is significantly dependent on the coating microstructure. More specially, macroscopic coating defects present over the coating considerably degrade the diffusion barrier performance of the coating by significantly increasing the the diffusivity ( $D$ ). Coating cracks are one of macroscopic defects. Generally, coating cracks formed during all the post-deposition processing (i.e., dispersion-fuel-plate manufacturing) act as a very fast diffusion path of solid materials, leading to the functional failure of the corresponding coating. It is known that the diffusivity in a coating crack is several orders of magnitude higher than that in a crack-free undamaged coating. Therefore, for the long lifetime ( $t$ ) of a diffusion barrier coating, the significant (several orders of magnitude) increase in  $D$  induced by the generated coating damages should be prevented even by decreasing the coating thickness ( $x$ ).

### **1.4.3. Factors influencing the coating fracture resistance**

For solid materials, the fracture resistance and diffusion barrier capability are significantly dependent on the microstructural properties such as the thickness, shape, packing density, type and density of the defects, grain size, texture, and surface roughness [90]. Furthermore, the residual stress also affects the fracture resistance. Theoretically, a coating layer has a high fracture resistance if it has a high compaction density with no macroscopic defect, and possesses a residual stress that is opposite to the stress that may cause the coating fracturing.

In general, thin sputtered coatings typically have a considerably different microstructure, and hence fracture resistance, as the corresponding bulk materials. In addition, as-deposited coatings also show various microstructures, and thus fracture resistance, depending on the deposition method and conditions applied. Therefore, by optimizing the controllable deposition-parameters, the coating microstructure can be improved, and consequently, the coating can achieve a superior fracture resistance to bulk materials. For magnetron sputtering machines, the controllable-deposition parameters are the applied voltage and current to the anode, distance between the target and substrate, base and working pressures of the chamber, and the working gas (normally, Ar gas). These controllable factors influence the kinetic energy of sputtered atoms ejected from the target material, and consequently influence the microstructure of the resulting coatings. Furthermore, the chemical and physical reactions of the coatings occurring during the deposition also influence the resulting coating microstructure. Hence, the microstructural characteristics of an applied thin film barrier need to be experimentally examined [69, 82].

## 1.5. Objective and scope of the present research

As mentioned before, U-7Mo/Al dispersion fuel plates containing a high density of LEU are considered a next-generation fuel design for high-performance RRs. For the fuel plates to be qualified and then commercialized, undesired phenomena limiting their lifetime (i.e., burnup) should be prevented. One phenomenon is the formation of the IL between U-7Mo fuel powders and an embedding Al matrix. To suppress the IL formation, a ZrN diffusion barrier layer has been applied to U-7Mo/Al dispersion fuels. It has been experimentally demonstrated through an annealing test, heavy-ion irradiation, and in-pile tests that a ZrN coating layer with a mean thickness of 1  $\mu\text{m}$  in U-7Mo/Al dispersion fuel plates shows a satisfactory diffusion barrier capability when structurally intact.

However, local and extremely large U-Mo/Al ILs were generated near the damaged coating regions, which is the main problem or drawback for the ZrN diffusion barrier layer. It was believed that coating damage had been generated during the dispersion-fuel-plate manufacturing. The dispersion-fuel-plate manufacturing includes two stress sources that may cause a damaged coating: One is thermal stress induced during heat-treatment processing (such as a blister test or preheating for hot rolling), and the other is an external mechanical stress induced during the compaction, hot-rolling, and cold-rolling steps. Accordingly, to allow fine solutions to avoid damage to their ZrN coating, several studies investigating the effects of each expected source of the coating damage need to be conducted. However, studies providing guidance on how best to suppress ZrN coating damage have yet to be applied.

In this research, focused is given to the effects of the first stress source (i.e., thermal stress induced at a high fabrication temperature) on ZrN coating fracturing. In addition, parametric studies of the ZrN coating microstructure were first conducted to characterize a realistic coating microstructure, which is necessary to understand the coating fracturing behavior. This dissertation is eventually aimed at suggesting ways to improve the diffusion barrier performance of a ZrN coating in U-Mo/Al dispersion fuel plates by maintaining its structural integrity.

This research is composed of three separate parts: the first two parts describe parametric studies of the ZrN coating microstructure, and the last part deals with research associated with the effects of a stress source on ZrN coating fracturing.

1. First, ZrN coatings of various thicknesses ranging from a mean of 0.1 to 2.6  $\mu\text{m}$  were deposited using a DC magnetron non-reactive sputtering technique on 45–90  $\mu\text{m}$ -sized U-7Mo powders, and were then examined in terms of the microstructural characteristics and residual stress using SEM, EDS, and XRD.

2. Second, the morphology and crystallographic properties of an as-fabricated ZrN sputtered coating were characterized as a function of the U-7Mo substrate size. A single-layer ZrN coating of mean 0.9  $\mu\text{m}$  thickness was deposited on 45–90  $\mu\text{m}$ -sized U-7Mo powders using a DC magnetron non-reactive sputtering machine. The as-fabricated coated U-7Mo powders were classified into four or five sized groups of (<45), 45–53, 53–63, 63–75, and 75–90  $\mu\text{m}$  through sieving. Subsequently, each powder group was characterized using SEM, EDS, and XRD. In addition, a semi-analytical model describing the relationship between the coating thickness and U-7Mo substrate size has been newly developed based on the measured coating thickness and the estimated friction-based position of the U-7Mo powders during deposition.
3. Lastly, by setting the checked parameters as variables, the effects of the coating thickness (0.3–3.5  $\mu\text{m}$ ), U-Mo substrate size (45 and 90  $\mu\text{m}$ ), and annealing temperature (300–700°C) on the ZrN coating failure on U-Mo powders at high post-deposition processing temperature (i.e., the heat-treatment temperature of dispersion-fuel-plate manufacturing) were investigated experimentally and numerically.

**Table 1. Candidates for LEU dispersion fuel [12].**

<b>Candidate Fuels</b>	<b>Uranium Density (g/cm<sup>3</sup>)</b>
UAl <sub>3</sub>	5.1
UO <sub>2</sub>	9.7
U <sub>3</sub> Si <sub>2</sub>	11.3
U <sub>2</sub> Mo	13.8
U-9Nb-3Zr	14.2
U <sub>3</sub> Si	14.7
U-6Nb-4Zr	14.8
U-5Nb-3Zr	15.5
U-10Mo	15.3
U-10Mo-0.05Sn	15.3
U-8Mo	16.0
U-7Mo	16.4
U-6Mo	16.7
U6Fe	16.7
U-6Mo-0.6Ru	16.5
U-6Mo-1Pt	16.5
U-6Mo-1.7Os	16.4
U-4Mo	17.4
U	19.0

**Table 2. Advantages and disadvantages of coating deposition methods used for U-Mo dispersion fuel powders.**

Method	Classification	Advantages	Disadvantages
<b>Magnetron sputtering deposition</b>  (A kind of Physical Vapor Deposition (PVD))	Depending on the substrate mixing equipment, <b>1) Turnable drum</b> (at KAERI and SCK·CEN )  - Only method with available irradiation data  - Used method in this research  <b>2) Shaking by oscillating magnet</b> (at TUM)	- Excellent uniformity on powder substrates - Dense coating - Low deposition temperature (i.e., ability to coat heat-sensitive substrates) - Excellent process control - No limitation on coating material (metal, alloy or compound)	- Line-of-sight deposition - Low deposition rate
<b>Chemical Vapor Deposition (CVD)</b>	<b>CVD with turnable substrate mixer</b> (at KAERI; for U-N coating)	- High deposition rate - Production of thick coating - No limitation on coating material (metal, alloy or compound)	- Relatively low thickness uniformity - High deposition temperature
	<b>Pack-cementation</b> (at KAERI, for U-Si coating)		
	<b>Fluidized Bed CVD</b> (FB-CVD; at CEA and INL)	- High thickness uniformity	- Very low deposition rate - Critic adjustment of the flow
<b>Atomic Layer Deposition (ALD)</b>	<b>ALD (at ANL)</b> ※ Recent EMPIRE test at ATR will show its effectiveness.	- Nearly perfect coating structure without any defects - High thickness uniformity and precise thickness control - 3D conformality (Coatable for substrates of complex geometry) - Low deposition temperature	- Critic adjustment of the flow - Very low deposition rate - Better with compound coating material like ZrN, not good with metal coating - Expensive equipment ; scale-up not demonstrated

**Table 3. Comparison of ZrN coating deposition-systems used in this research and the SELENIUM project (SCK-CEN).**

	<b>This research</b>	<b>SELENIUM project [61]</b>
<b>Deposition type</b>	Non-reactive DC magnetron sputtering	Reactive RF magnetron sputtering
<b>Rectangular target (purity)</b>	ZrN (>99.5%)	High-purity Zr
<b>Deposition time for 1-<math>\mu</math>m thickness (hour)</b>	7	7
<b>Rotation speed of mixing drum (rotations per minute)</b>	8	2 – 5
<b>Base pressure (Torr)</b>	$3 \times 10^{-5}$	$7.5 \times 10^{-4}$
<b>Gas (mass flow)</b>	Ar (55cc/min)	Ar (76cc/min) + N <sub>2</sub> (6 cc/min)
<b>Working pressure (Torr)</b>	$2.0 \times 10^{-3}$	–
<b>Power (kW)</b>	1.0	0.8
<b>Distance of drum bottom to target (cm)</b>	17	–



**Table 4. Material properties of ZrN.**

Property	ZrN
<b>Structural properties</b>	
<b>Lattice structure</b> (space group)	Faced-centered cubic (Fm-3m, No. 225) [92]
<b>Lattice constant (Å)</b>	4.5700 [92]
<b>Density (g/cm<sup>3</sup>)</b>	7.09 [93]
<b>Thermal properties</b>	
<b>Melting point (°C)</b>	2952 [93]
<b>Standard enthalpy of formation (kJ/mol)</b>	-365.26 [94]
<b>Activation energy of oxidation (kJ/mol)</b>	241±10 <sup>a</sup> [95]
<b>Thermal conductivity (W/m/K)*</b>	20.5 <sup>b</sup> [96]
<b>Mechanical properties</b>	
<b>Vickers hardness (GPa)</b>	25 [92]
<b>Young's modulus (GPa)</b>	450 [92]
<b>Poisson's ratio</b>	0.25 [92]
<b>Optical property</b>	
<b>Color</b>	Gold
<b>Nuclear property</b>	
<b>Absorption cross section for thermal neutron (barn)</b>	2.24

<sup>a</sup> At 475°–650 °C.

<sup>b</sup> At room temperature.

**Table 5. Analyzed characteristics and necessary studies of ZrN reactively-sputtered coating deposited on U-Mo atomized powder by different coating methods**

	<b>Magnetron reactive sputtering</b>	<b>Need to be studied</b>
<b>Phase</b>	ZrN single phase containing impurities (ZO <sub>2</sub> , ZN <sub>2</sub> , and O) [30,60,62,76]	-
<b>Target thickness (μm)</b>	1 [37,88] (based on a TRIM simulation result)	-
<b>Uniformity in coating thickness</b>	Low [62,68,75] (e.g., 0.8-1.5 μm for mean 1.0 μm [61])	(For the realistic evaluation of ZrN coating microstructure,) A detailed study on the microstructural parameters as a function of the coating thickness and U-Mo powder
<b>Dense-to-porous structural transformation thickness</b>	0.2 μm [62,76] (the thickness starting column-boundary defect)	
<b>Structure</b>	Columnar structure [62,76]	-
<b>Grain size</b>	Nanosize [62,76]	-
<b>Deposition rate</b>	High (142 nm/h) [61]	
<b>Diffusion barrier performance</b>	Good for intact coatings, whereas poor for locally damaged coatings [37,61]	Evaluation and appropriate solutions of coating fracturing in a manufacturing process that may damage the coating

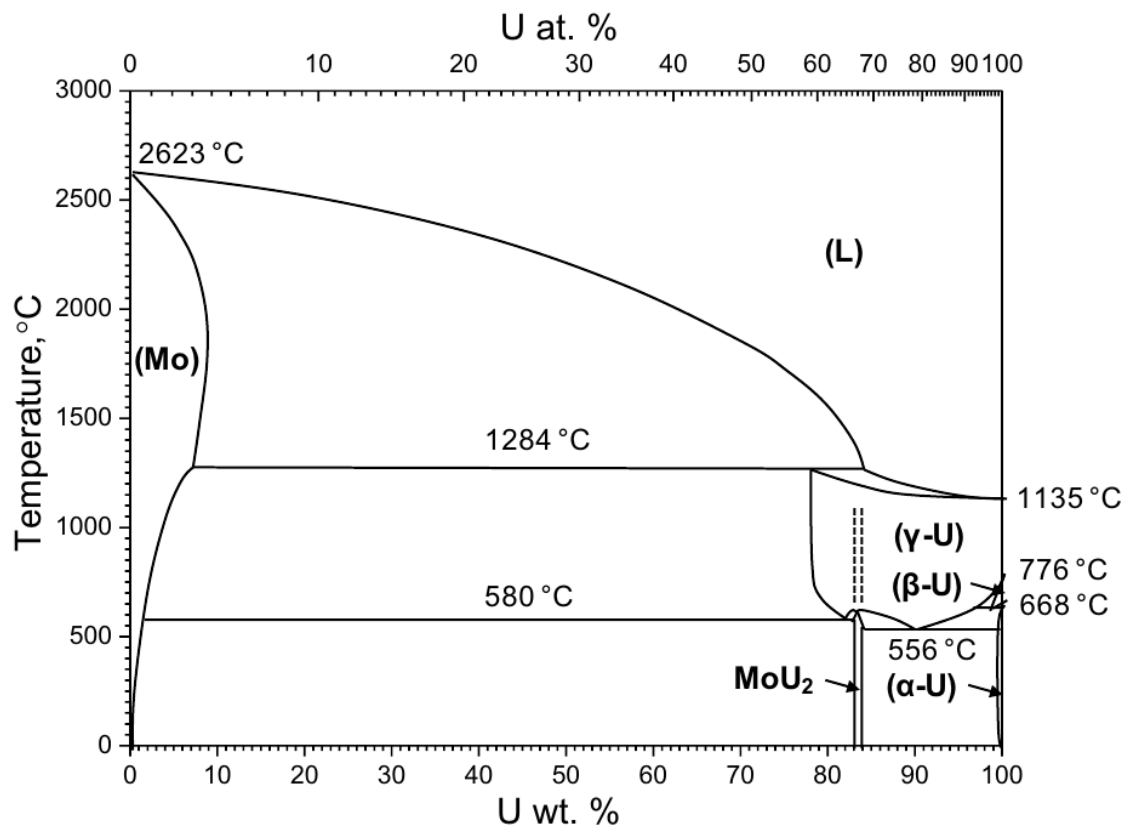


Figure 1. Phase diagram of uranium-molybdenum alloy [214].

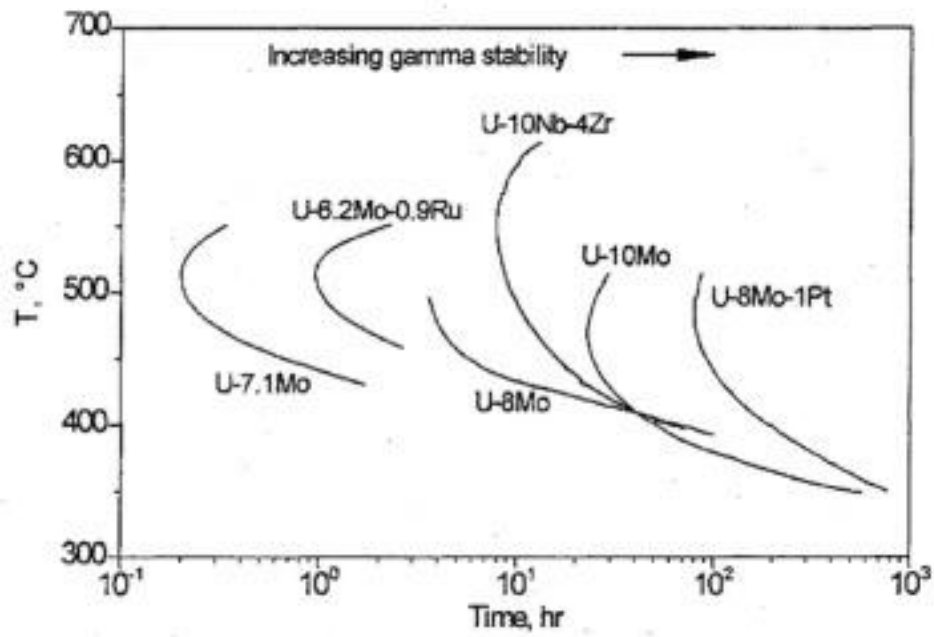
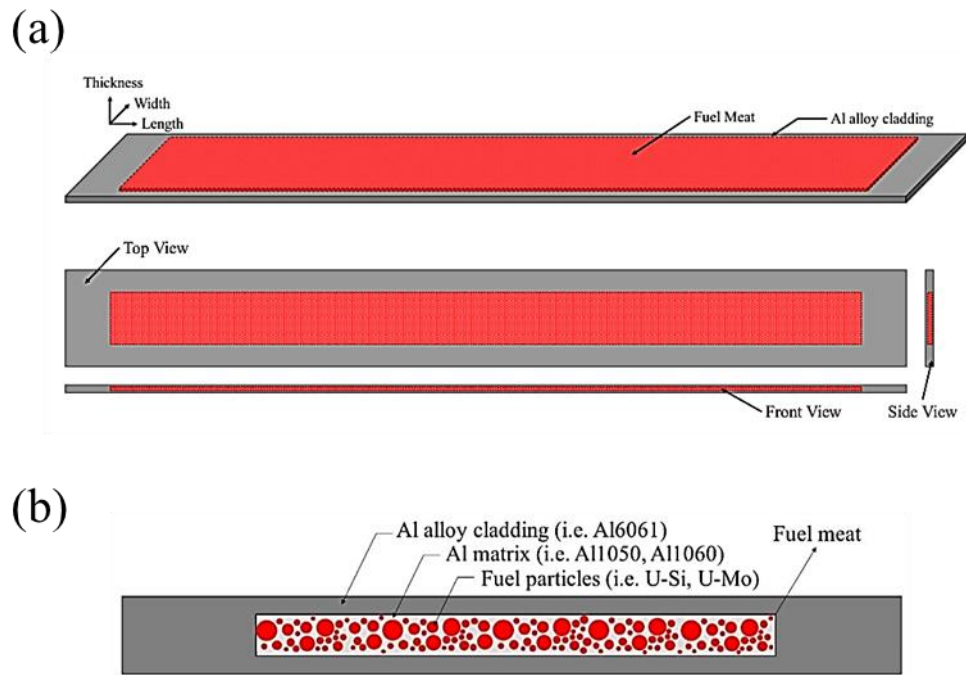


Figure 2. Time-Temperature-Transformation diagram for  $\gamma$ -U alloy fuel candidates [98].



**Figure 3. Schematic of commonly used plate-type dispersion fuel: (a) overview and (b) cross-sectional image [215].**

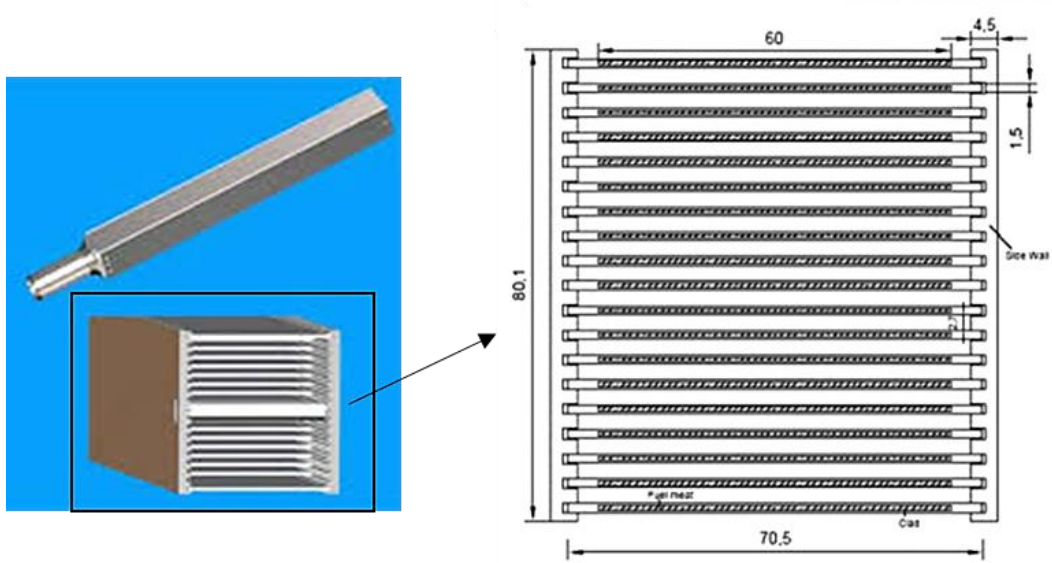
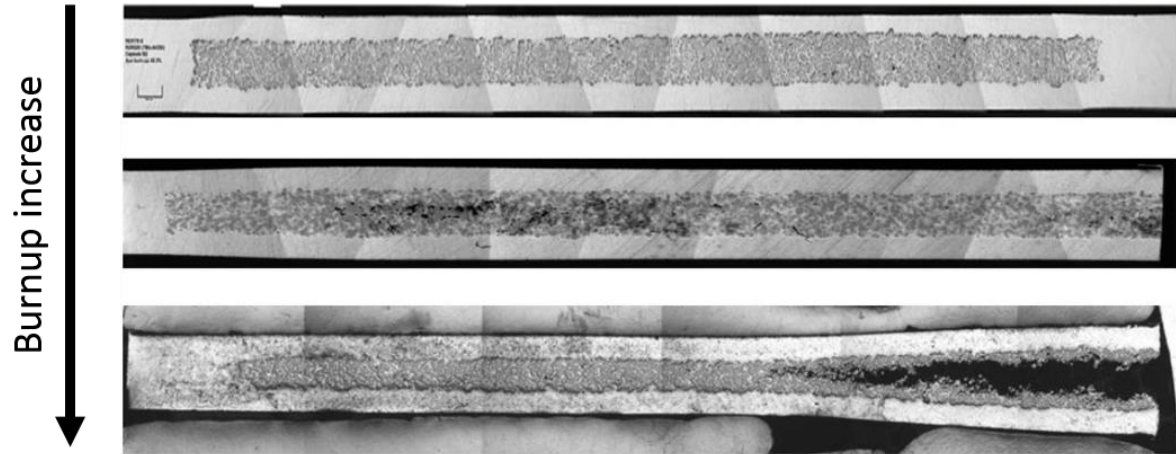
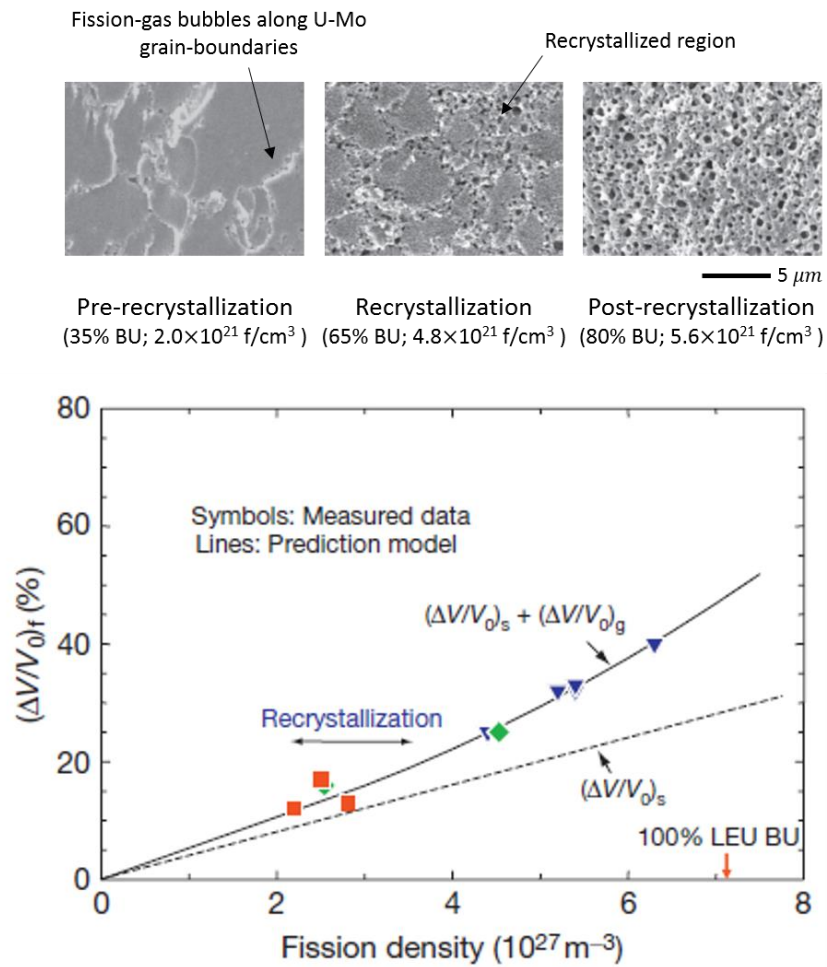


Figure 4. Normal fuel assembly loaded into research and test reactors [216].



**Figure 5. In-pile irradiation test results of U-Mo/Al dispersion fuel shows a severe swelling and even rupture with increasing the burnup [9].**



**Figure 6. Recrystallization (upper images) and swelling behavior (bottom graph) of irradiated U-10Mo/Al dispersion fuel plate as a function of fission density [8].**



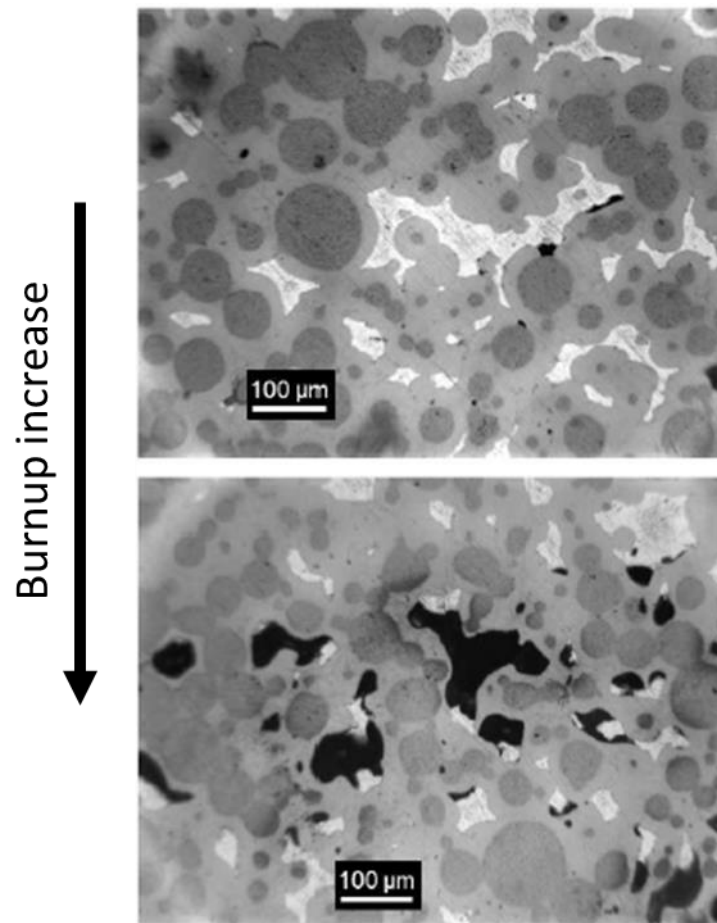
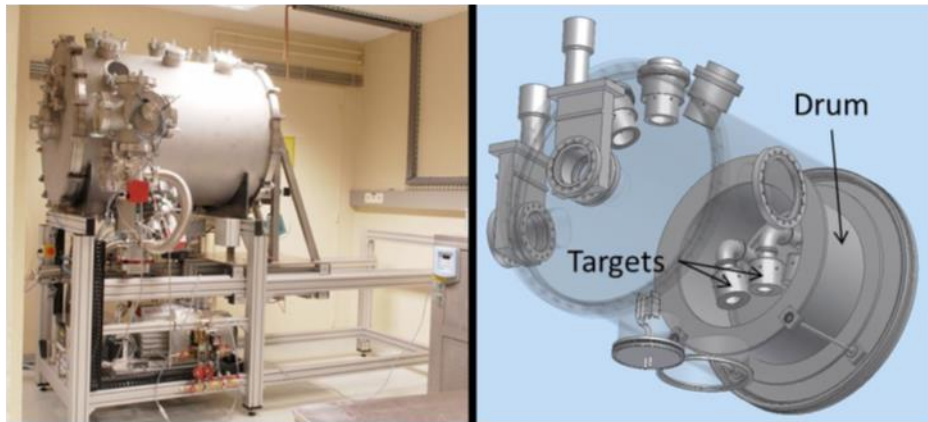


**Figure 7. U-Mo/Al dispersion fuels irradiated upto a high burnup shows fission gases are agglomerated into a large pore by snowploughing effect of U-Mo/Al interaction layer [9].**

(a)



(b)

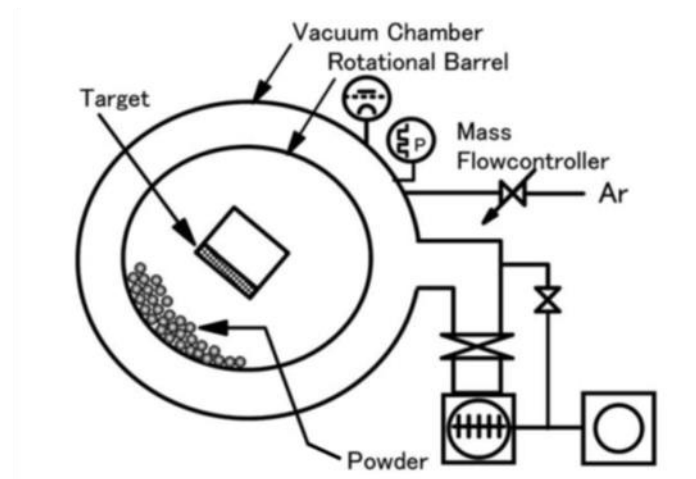
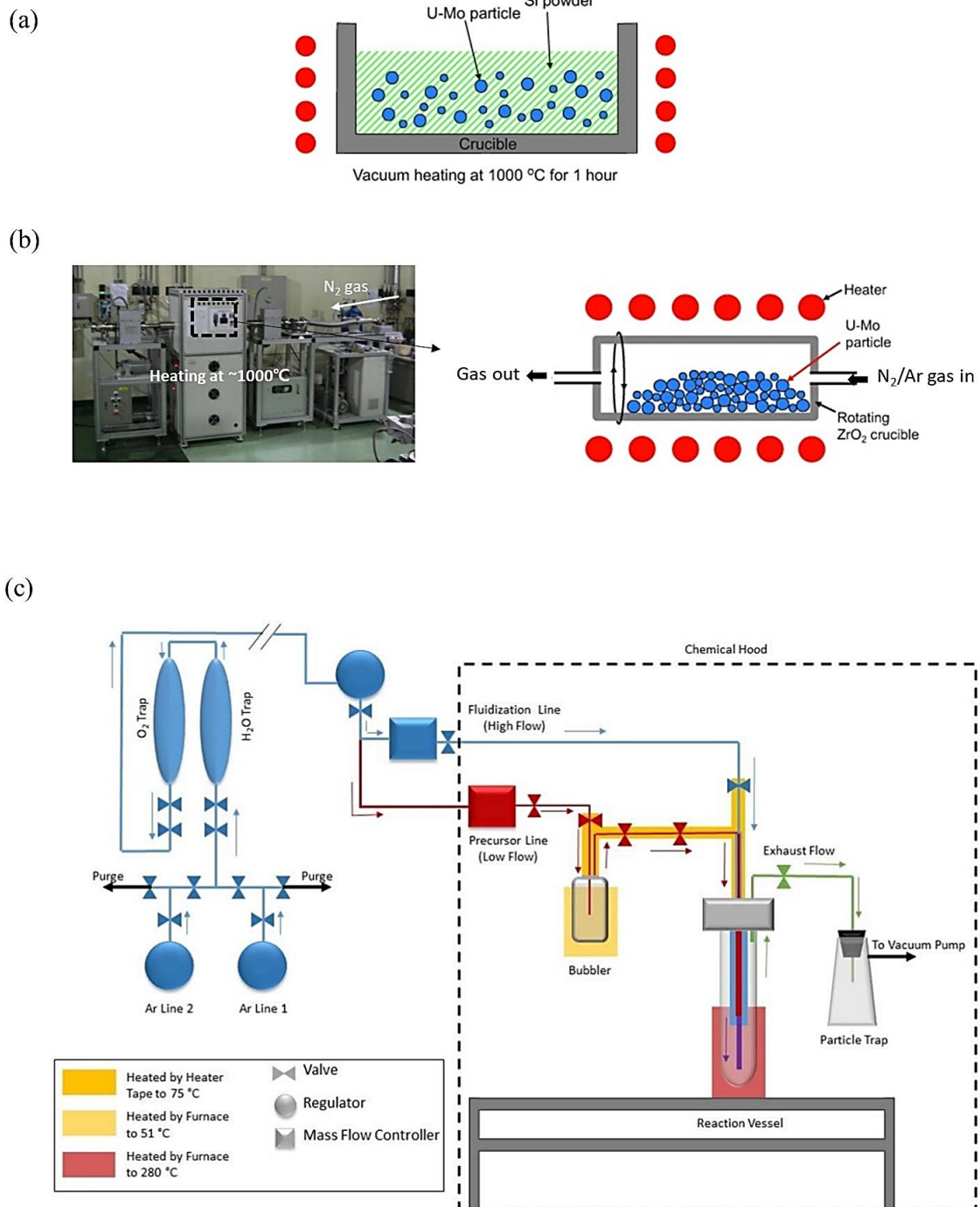
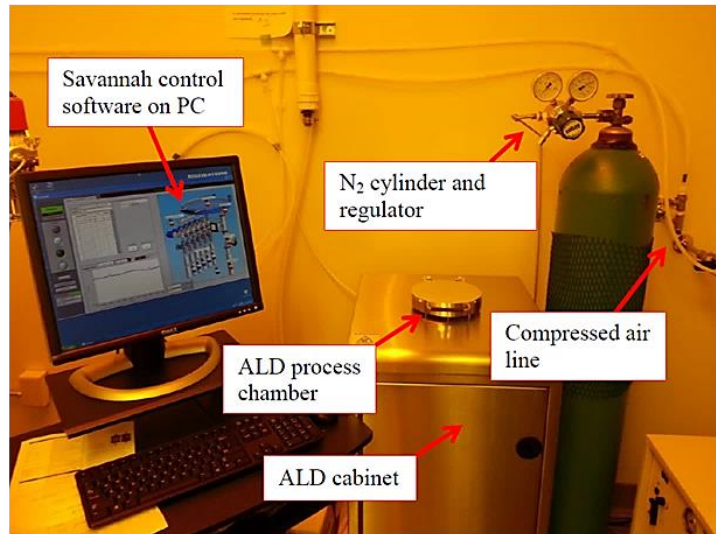


Figure 8. (a) Photo and schematic of the STEPS & DRUMS [97] and (b) schematic diagram of a general barrel sputter deposition system [217].



**Figure 9. Schematics and photo of three-type CVD systems fabricating a diffusion barrier coating on U-Mo dispersion fuel powders: (a) Pack-cementation for U-Si coating [78], (b) CVD with a tunable substrate mixer for U-N coating [77, 78], and (c) FB-CVD for ZrN coating [67].**

(a)



(b)

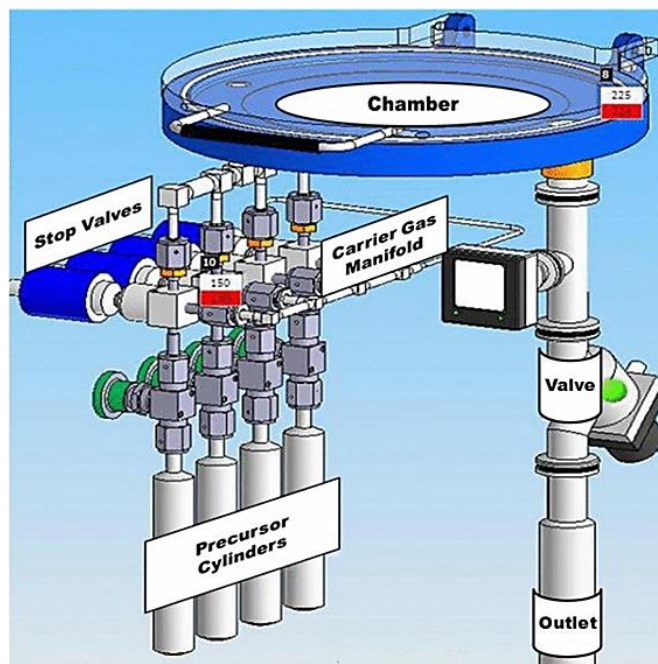
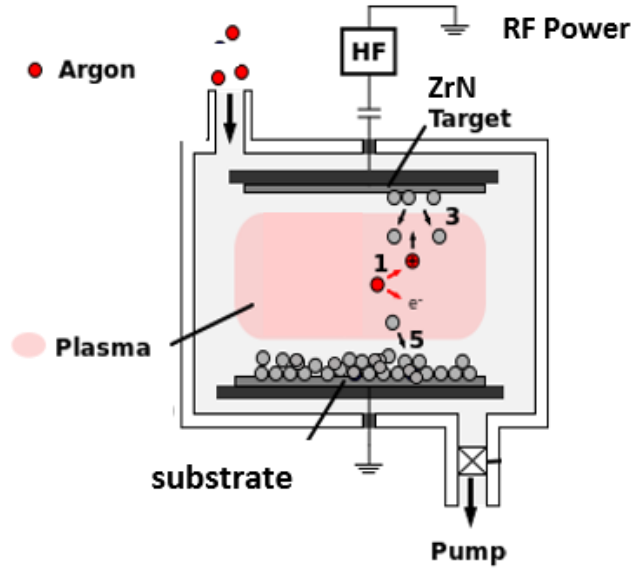


Figure 10. (a) Set-up and (b) schematic view of ALD Savannah system [218].

(a)



(b)

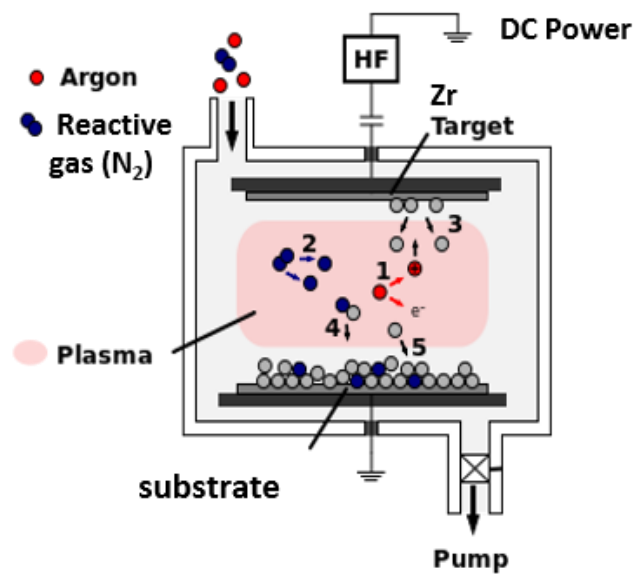
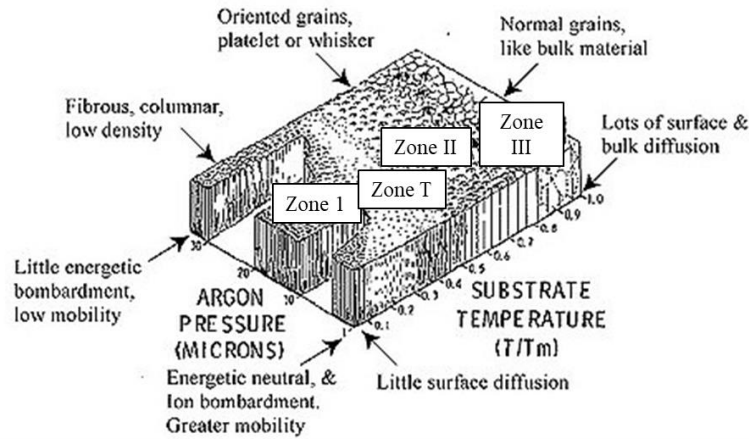
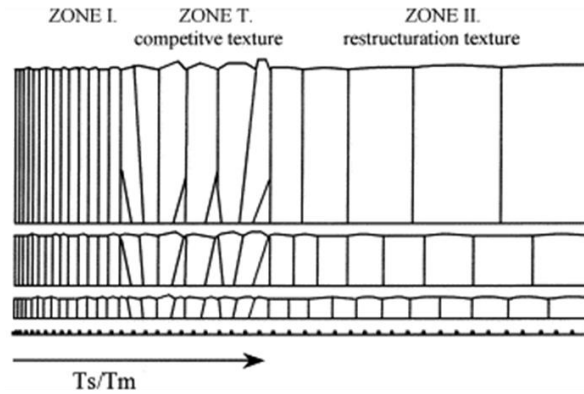


Figure 11. Magnetron sputtering systems for ZrN coating deposition: (a) non-reactive system (KAERI, used in this research) and (b) reactive sputtering (SCK·CEN).

(a)



(b)



(c)

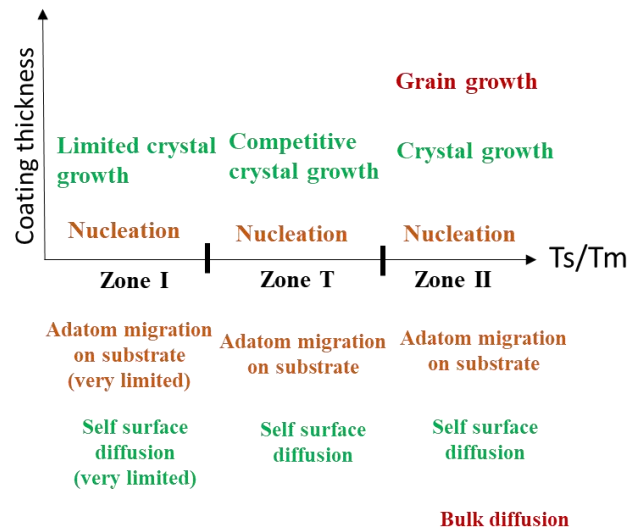
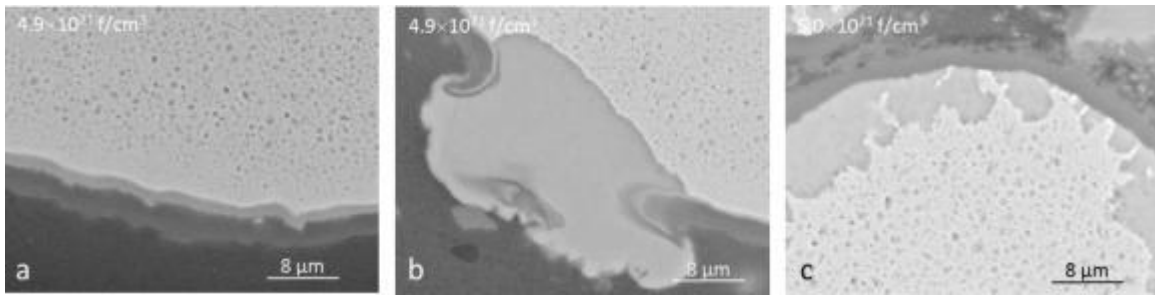


Figure 12. Thornton's structure zone model [177]: (a) coating morphologies as a function of deposition temperature and working pressure, and the (b) cross-section and (c) growth steps and corresponding dominant diffusion mechanism of Zone I, T, and II structures as a function of coating thickness [128].



**Figure 13. Three types of U-Mo/Al interaction layer observed in ZrN coated U-7Mo/Al dispersion fuel irradiated up to  $\sim 5.0 \times 10^{21}$  fission/cm<sup>3</sup>: (a) thin IL, (b) ‘erupting volcano’ shaped extensive IL near the coating crack, and (c) huge IL formed through the coating crack that once existed [36].**

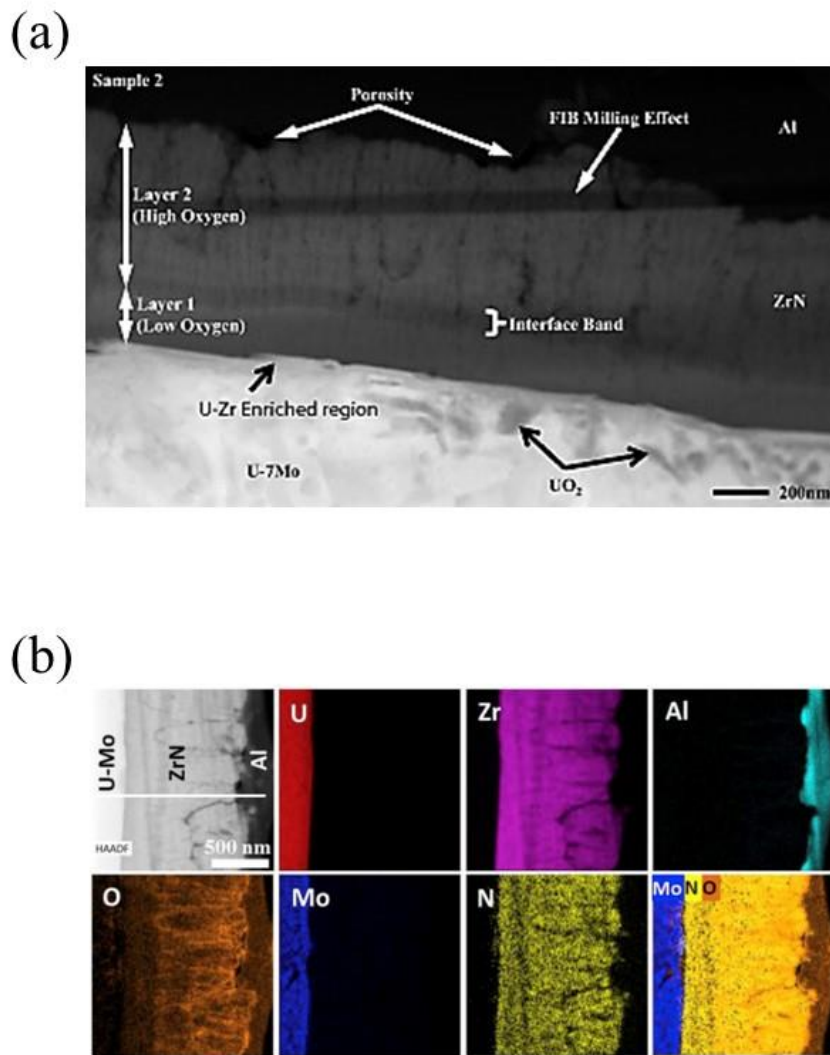


Figure 14. (a) TEM bright-field cross-sectional image and (b) TEM-EDS mapping image of a ZrN reactively sputtered coating layer on a U-7Mo powder [61].



Expected critical steps for structural integrity of ZrN coating

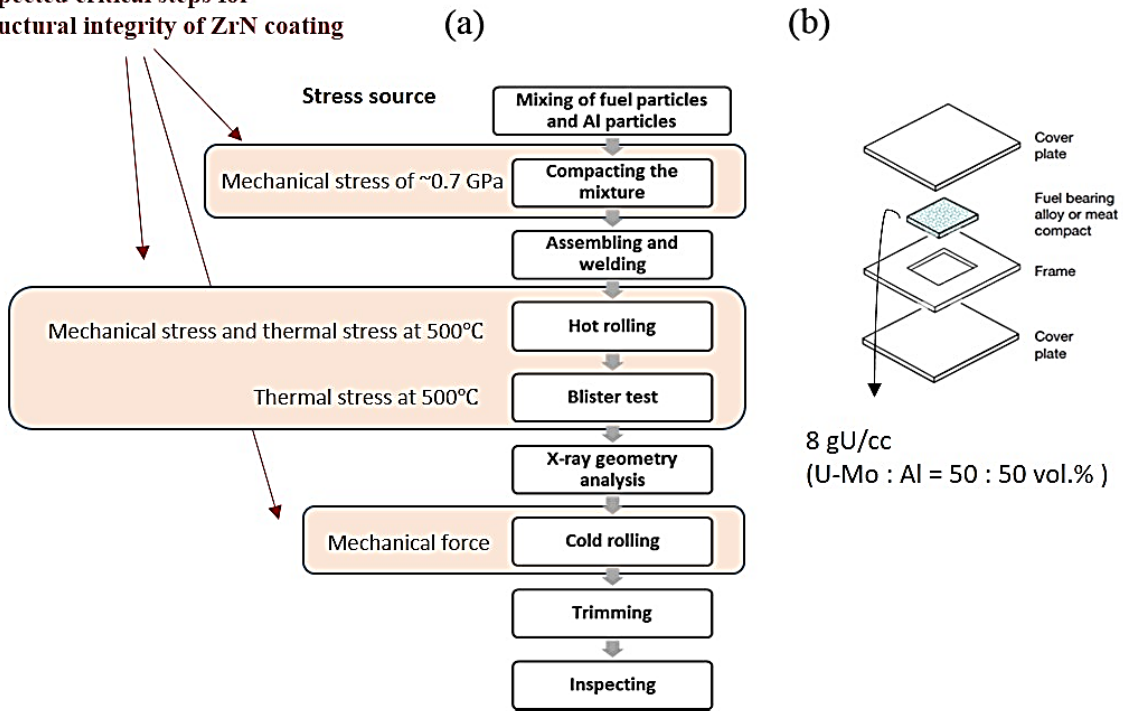


Figure 15. (a) Critical stress sources for ZrN coating damage during a general fabrication process of dispersion fuel plates and (b) exploded view of a U-Mo/Al dispersion fuel assembly with a uranium density of  $8 \text{ gU/cm}^3$  [8].

## Chapter 2. Experimental methods

### 2.1. Coating deposition

By using 45–90  $\mu\text{m}$ -sized U-7Mo powders of 50 g per deposition, a single coating layer of ZrN was deposited on the powders using a DC magnetron non-reactive sputtering machine depicted in Figure 16. The coating deposition system was equipped with a rotary drum to sufficiently agitate the U-7Mo powders inside the drum through the rotational motion during the entire deposition time, which is aimed to fabricate a homogeneous coating thickness over the U-7Mo powder. In addition, a rectangular planar target was chosen among various types of available targets (e.g., planar, circular, or tubular target) for a large sputtering area, which is normally required in line sputtering systems where substrates on some form of a conveyor belt, carrier, or drum (used in this research) linearly pass the target.

The deposition parameters of ZrN coating are listed in Table 6. These parameters excepting the deposition temperature are optimized values for a homogeneous thickness of ZrN coating on the U-7Mo powders. On the other hand, without external heating, the deposition temperature (substrate surface temperature) increases during the deposition by striking of accelerated Ar ions / atoms and coating atoms / molecules with the substrate surface. Thermodynamically, some of kinetic energies of the accelerated materials is converted into thermal energies. The deposition temperature corresponding to the substrate temperature during deposition, was measured at the surface of a U-7Mo ingot sample using a K-type thermocouple under the same deposition environment without a drum rotation. The measured deposition temperature was approximately 250°C.

### 2.2. Experimental techniques for coating characterization

#### 2.2.1. Scanning electron microscopy (SEM)

SEM is a type of microscopic electron visualization of the sample surface by scanning with a concentrated electron beam, as illustrated in Figure 17 (a). The reaction between the electron beam and sample surface causes their energy exchange, leading to the reflection of high-energy electrons, and the emission of secondary electrons by elastic and inelastic scattering. The reflected high-energy electrons and emitted secondary electrons can be recorded using back-scattered electron (BSE) and secondary electron (SE) detectors, respectively. These imaging (or detection) modes are determined depending on the detection purpose because BSE and SE inherently have different interaction volumes, as shown in Figure 17 (b), namely, a surface morphology analysis for SE image mode, and a composition and cavity

analysis for BSE image mode. Depending on the atomic number and density of a sample, the interacted sample volume, referred to as the interaction volume, is  $\sim 10$  nm for SE mode and  $< 2$   $\mu\text{m}$  for BSE mode in terms of depth from the sample surface. In addition, the resolution of conventional (or normal) SEM is approximately several nanometers. In this dissertation, SEM (VEGA3, TESCAN Co., Czech) applied at 30 kV under vacuum conditions was utilized to analyze the morphological characterization of the samples.

### 2.2.2. Energy-dispersive X-ray spectroscopy (EDS)

EDS, which is an accessory for SEM, is a commonly used analysis tool for the qualification and quantification of chemical elements of a sample using the emitted X-ray originating from the interaction between the sample and applied electron beam (see Figure 18 (a)). Incident electron beams energetically activate a sample surface from the ground state (or unexcited state) to an excited state, leading to X-ray emissions during the process of energy release. The intensity and energy of an emitted X-ray measured using EDS can be represented by an energy-dispersive spectrometer, as illustrated in Figure 18 (b). By interpreting the energy dispersive spectrometer, the elemental composition of the specimen can be figured out. Besides, by using EDS mapping (or element distribution images) function, the elemental composition distribution of specimens can be displayed as a television-like image showing the quality and quantity of sample elements as color and intensity of the image. EDS analysis can detect all elements except light elements (atomic number  $< 11$ ). In the case of major elements, a precision (defined as  $2\sigma$ ) of EDS analysis is better than  $\pm 1$  at.%. On the other hand, the general precision is normally  $\pm 2$  at. %.

In this dissertation, an EDS (INCA X-Act, Oxford Co., England) analysis was conducted using a 30 kV electron beam at a 15 cm working distance (i.e., distance between the final pole piece of the lens and the sample) to obtain a reliable count number (normally,  $>10,000$  per second). The measured EDS results were analyzed using the AZtec program (Oxford Co., England).

### 2.2.3. X-ray diffractometer (XRD)

#### 2.2.3.1. Principle and operation condition

X-ray powder diffraction (XRD) is a normally used analysis tool to enable a qualitative and quantitative analysis of the crystal structure of a sample, which is based on Bragg's law and a Rietveld refinement. An XRD analysis is applied to interpret the wave interference between a monochromatic incident X-ray beam and a sample structure. As shown in Figure 19 (a), a XRD machine is composed of the following simple components: an X-ray source, a sample holder, and an X-ray detector. X-rays are produced by generating electrons by heating a filament and then striking a target material with electrons accelerated through an applied voltage. The X-ray produced is filtered with several slits to obtain monochromatic X-rays (normally, CuK $\alpha$  radiation of a 1.5418Å wavelength), and then collimated to concentrate the X-rays before reaching the sample. The interaction between the incident X-rays and the sample surface generates a constructive interference and characteristic X-ray spectrum (Figure 19 (b)) if the sample lattice structure meets with Bragg's Law (Eq. (8)). Because the sample and detector are rotated at the same time, the intensity of the reflected X-rays is recorded over a wide  $2\theta$  angle range (generally, from  $\sim 5^\circ$  to  $80^\circ$ ). From the characteristic X-ray spectrum obtained, various types of structural information of the samples can be obtained, as written in in Figure 19 (b).

In this dissertation, composition and structural analyses of the samples were measured at room temperature using an XRD (ULTIMA IV, Rigaku Co., Japan) with Cu-K(a) radiation (at a wavelength of 1.5406 Å, an accelerating voltage of 40 kV, and a current of 30 mA). XRD patterns were recorded with a cover range of  $2\theta = 20\text{--}80^\circ$  with  $\theta$ - $2\theta$  mode, a  $0.02^\circ$  scan step, and a scan step time of 10 s. A 10-mm sized divergence slit and a 0.6-mm sized receiving slit were used. All measured XRD patterns were analyzed using the Rietveld method with the PDXL 2 software program (Rigaku Co., Japan).

### 2.2.3.2. Analysis equations for crystallographic properties

The interplanar spacing can be calculated using the following Bragg's law ([99], Figure 19 (a)).

$$d_{hkl} = \frac{\lambda}{2\sin\theta} \quad (9)$$

where  $d_{hkl}$  is the interplanar spacing of the corresponding (hkl) plane in nm (h, k, and l are the Miller indices),  $\lambda$  is the wavelength of the radiation beam (0.1506 nm for CuK $\alpha$  radiation), and  $\theta$  is the diffraction angle in radians.

The texture coefficient corresponding to the (hkl) orientation ( $TC_{(hkl)}$ ) of the ZrN coatings in this study is defined as [100]:

$$TC_{(hkl)} = \frac{I_{(hkl)}}{\sum I_{(hkl)}} \quad (10)$$

where  $I_{(hkl)}$  is the measured relative intensity of a (hkl) plane. From the  $TC_{(hkl)}$  of a sample, its distribution of crystal orientations can be identified. The larger  $TC_{(hkl)}$  is, the larger the abundance of crystallites oriented in the (hkl) direction.

The grain (crystallite) size (D) and equivalent microstrain ( $\eta$ ) can be expressed using Halder-Wagner equation [101, 102], which is given as follows:

$$\frac{\beta^2}{\tan^2\theta} = \frac{K\lambda}{D} \cdot \frac{\beta}{\tan\theta \cdot \sin\theta} + \eta^2 \quad (11)$$

where  $\beta$  is the diffraction-peak width, K is the shape coefficient, and  $\lambda$  is the wavelength of Cu-K $\alpha$  radiation, namely, 1.5406 Å. In this dissertation, K = 0.9, and the integral peak widths (i.e., the total peak area divided by the peak height) were used as  $\beta$ . By linearly plotting  $\beta^2/\tan^2\theta$  versus  $\beta/(\tan\theta \cdot \sin\theta)$ , D and  $\eta$  can be calculated using the slope of  $K\lambda/D$  and the intercept of  $\eta^2$ .

For the cubic unit cell of ZrN, the lattice constants can be obtained as follows:

$$\frac{1}{d_{hkl}^2} = \frac{h^2 + k^2 + l^2}{a^2} \quad (12)$$

where  $a$  is the lattice constant.

The density of the ZrN coatings was obtained as described below:

$$\rho = \frac{M}{A \cdot V} \quad (13)$$

where  $\rho$  is the coating density;  $A$  is the Avogadro constant,  $6.02 \times 10^{23}$ ;  $M$  is the molar mass; and  $V$  is the unit cell volume.

According to Hook's law, the stress ( $\sigma$ ) of a solid induced by the acting forces is linear to the Young's modulus ( $E$ ) and the macrostrain ( $\varepsilon$ ) of the solid as follows:

$$\sigma = E \cdot \varepsilon \quad (14)$$

In general, the macrostrain measured at room temperature originates mainly from the in-plane and out-of-plane residual stresses. For thin coatings, the residual out-of-plane stress is negligible (i.e.,  $\sigma_z = 0$ ), and it can thus be assumed that the macrostrain solely results from the biaxial residual in-plane stress. To simplify the stress calculation of the as-fabricated coatings in this dissertation, the coatings were assumed to be under equi-biaxial strain and stress. In this dissertation, for ZrN coatings, the in-plane residual stress in a certain direction (i.e., the  $x$  direction),  $\sigma_x$ , can be calculated by utilizing the macrostrain of the measured (200) diffraction plane of the ZrN coating ( $\varepsilon_{(200)}$ ) as follows:

$$\sigma_x = E \cdot \varepsilon_{(200)} \quad (15)$$

$$\text{with} \quad \varepsilon_{(200)} = \frac{d_{(200)} - d'_{(200)}}{d'_{(200)}}$$

where  $d_{(002)}$  and  $d'_{(002)}$  are the measured and standard lattice spacing for the (002) diffraction plane of the ZrN coating. It was assumed in this study that  $\nu$  is 0.25 and  $d'_{(200)}$  is  $2.285 \text{ \AA}$  [103]. The value of  $E$  was set as 114 GPa, which is the measured value of the ZrN coating fabricated through an RF magnetron non-reactive sputtering method using a ZrN target under 2.2 mTorr [104].

### 2.3. Annealing tests

Annealing tests were conducted to assess the influence of post-deposition annealing on the structural integrity of ZrN coatings on U-7Mo powders (Chapter 5). Two different annealing tests were applied. First, 45–90  $\mu\text{m}$ -sized U-7Mo powders coated with a ZrN single layer with various thicknesses of 0.3 to 3.5  $\mu\text{m}$  were annealed at 500°C for 2 h to estimate the influence of the coating thickness on the structural integrity of the coating. Second, 45  $\mu\text{m}$ -diameter U-7Mo powders coated with a ZrN layer with a mean thickness of 0.74  $\mu\text{m}$ , and 90  $\mu\text{m}$ -diameter powders coated with a ZrN coating layer with a mean thickness of 1.06  $\mu\text{m}$ , were annealed at various annealing temperatures of 300–700°C for 2 h, which aimed at investigating the effects of the annealing temperature on the structural failure of the coating. All annealing tests were conducted under high vacuum conditions of  $2.3 \times 10^{-5}$  Torr with a slow heating rate of 16.7°C/min. Immediately after an annealing test, the furnace was turned off and then slowly cooled without artificial cooling applied. The slow heating and cooling of the annealing tests aimed to prevent cracking of the coating triggered by a rapid change in temperature.

## 2.4. Sample preparation

### 2.4.1. U-7Mo powders

U-7Mo powders utilized in this research were fabricated by centrifugal atomization method at KAERI [105]. Among the as-fabricated U-7Mo powders, only 45–90  $\mu\text{m}$ -sized U-7Mo particles, classified by sieving, used in this study. As shown in Figure 20, 45–90  $\mu\text{m}$ -sized U-7Mo powders exhibited nearly-spherical shape and a mixed surface of smooth, wrinkle, and pitted surfaces. Additionally, it was identified from the XRD analysis result (Figure 21) that the powders were  $\gamma$ -U-7Mo phase containing a small amount of uranium dioxide ( $\text{UO}_2$ ) and uranium carbide (UC). It is predicted that a thin  $\text{UO}_2$  layer had been generated on the air-exposed surface of the oxidative powders during the fabrication and storage of the powders. In addition, it is guessed that UC intermetallic compound had been formed by the chemical reaction between the U-Mo melt and graphite crucible during the powder production.

### 2.4.2. Sample preparation for characterization

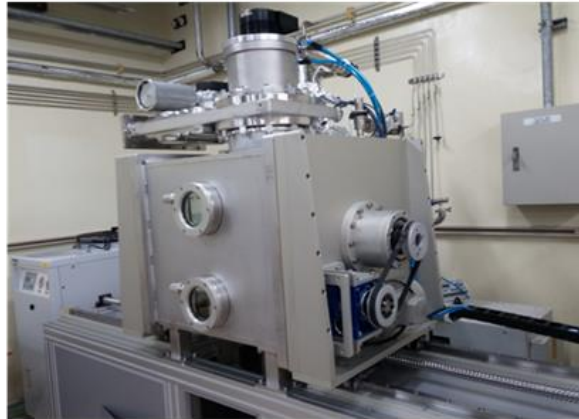
ZrN-coated U-7Mo powder samples were characterized using SEM, EDS, and XRD. For a surface morphological analysis utilizing SEM and EDS, the powder samples were fixed to a sample holder using sticky carbon-tape. In the case of a cross-sectional morphological analysis using SEM and EDS, the powder samples were prepared through the following steps: (1) mounting with hot mounting resin containing a small amount of a carbon conductor at 180°C for 4 min, (2) polishing using a 1,000 grit sanding disc to a 1  $\mu\text{m}$  diamond paste, and subsequently (3) cleaning using an ultrasonic cleaner for 10 min with ethanol and acetone. For the crystallographic XRD analysis, the powder samples were measured without preparation.



**Table 6. Deposition condition of ZrN sputtered coating.**

	ZrN coating
<b>Rectangular target (Purity)</b>	ZrN (>99.99%)
<b>Deposition time (hour)</b>	1 – 25
<b>Rotation speed of mixing drum (revolutions per minute, rpm)</b>	8
<b>Base pressure (Torr)</b>	$3 \times 10^{-5}$
<b>Working gas</b>	Ar
<b>Working pressure (Torr)</b>	$2.0 \times 10^{-3}$
<b>Applied power (kW)</b>	1.0
<b>Substrate-to-target distance (cm)</b>	17

(a)



(b)

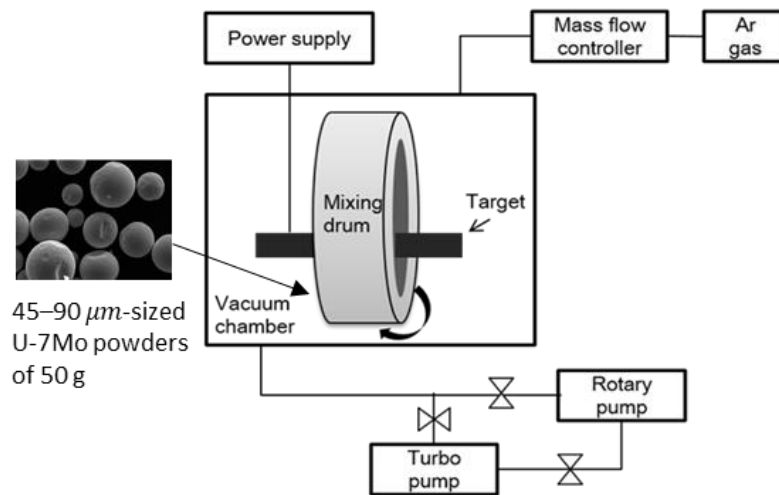
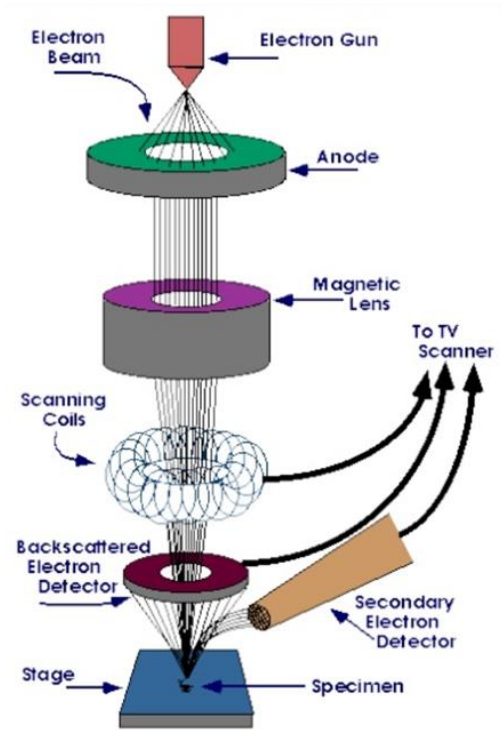


**Figure 16. (a) Photo and (b) schematic illustration of DC magnetron sputtering coating system used in this research.**

(a)



(b)

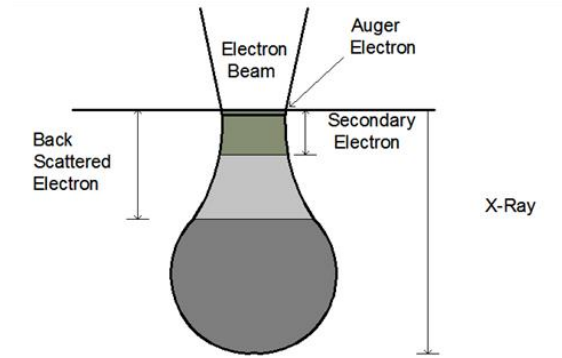


**Figure 17. Schematic drawings of (a) SEM and (b) interaction volume (detection volume) for an electron beam [212, 213].**

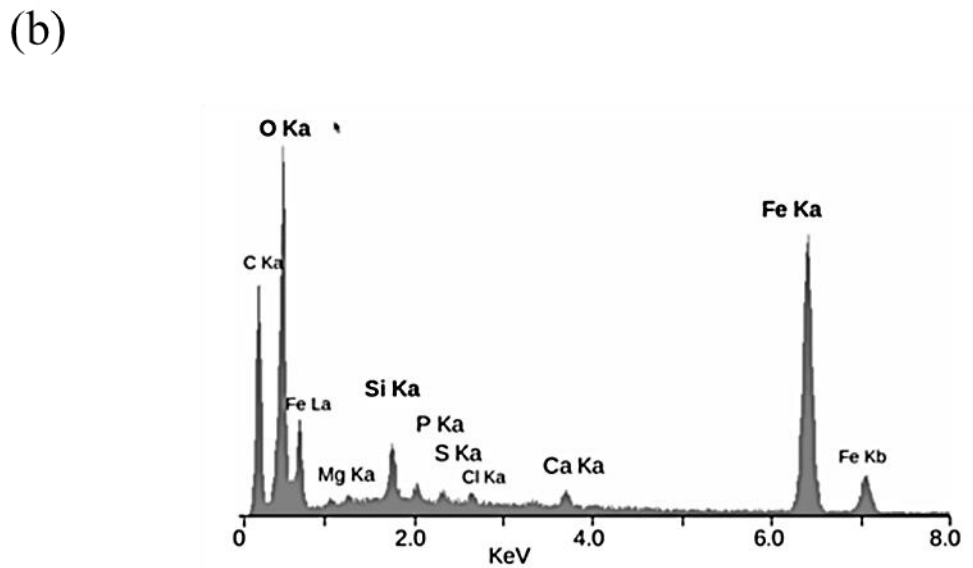
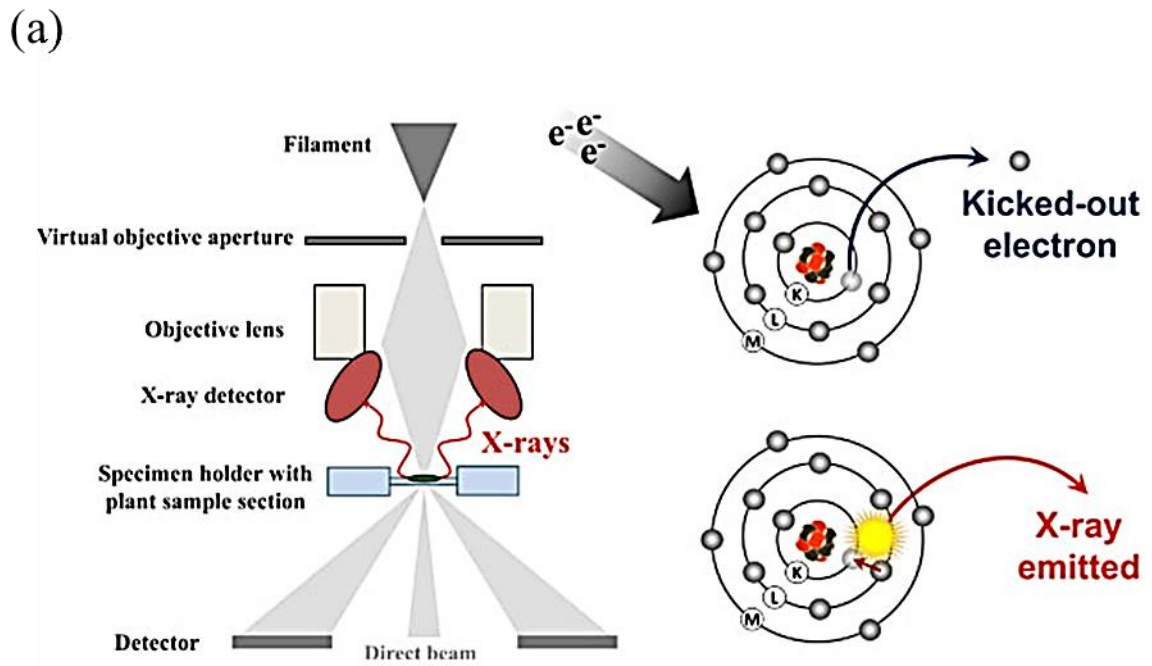
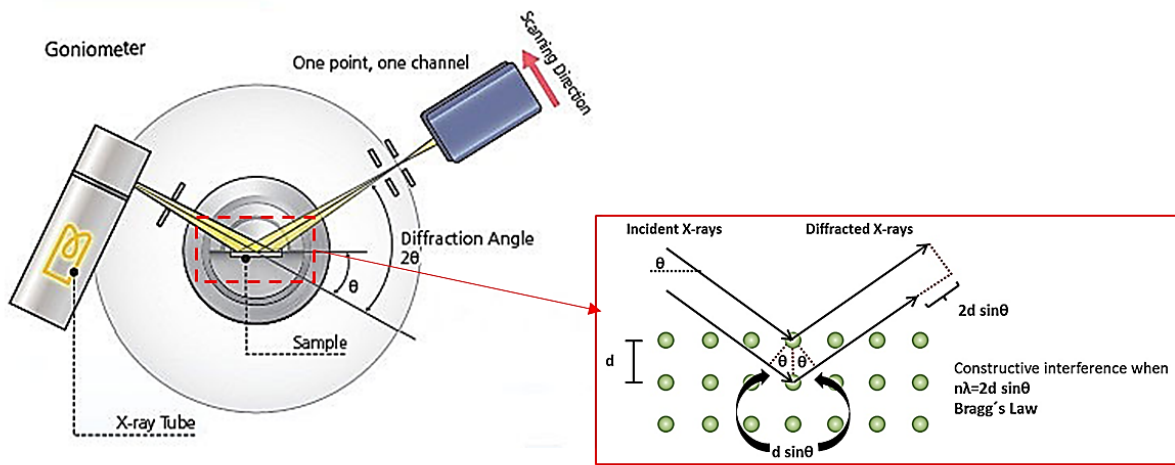


Figure 18. (a) EDS principle and (b) an EDS spectrum example [214, 215].

(a)



(b)

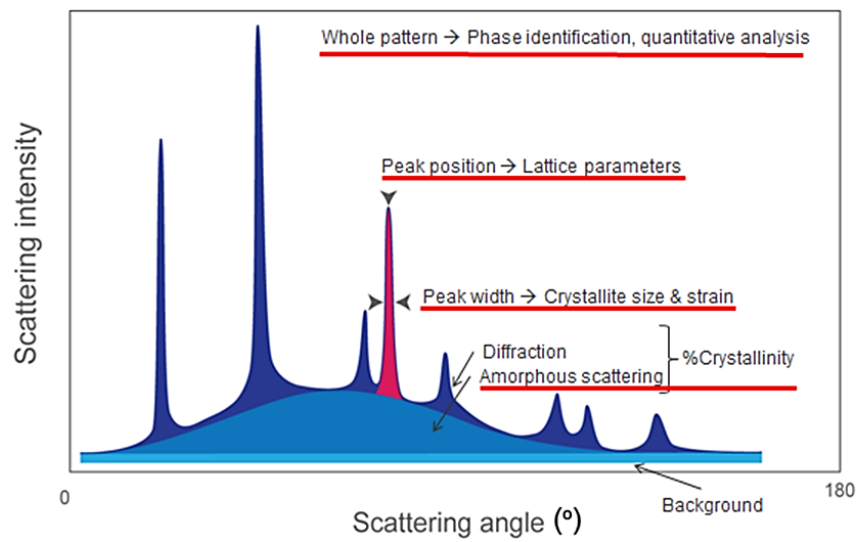
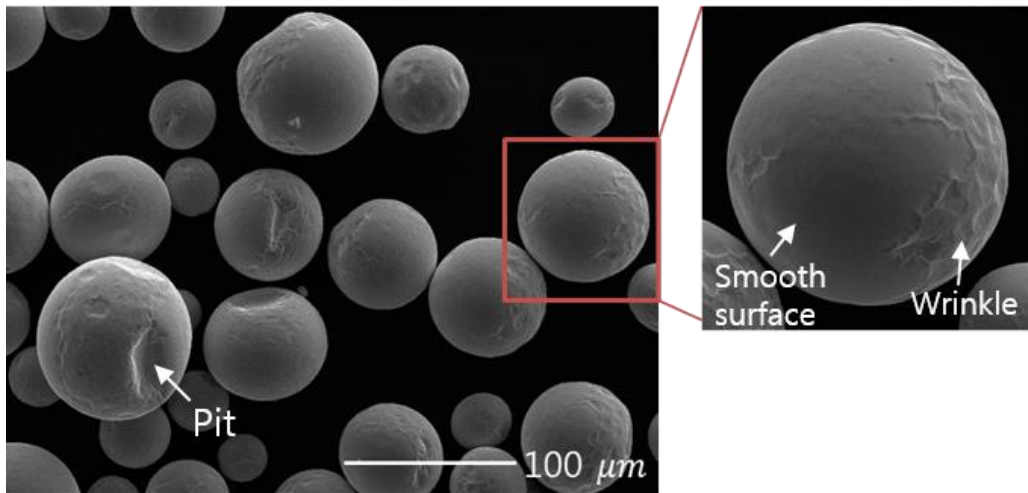
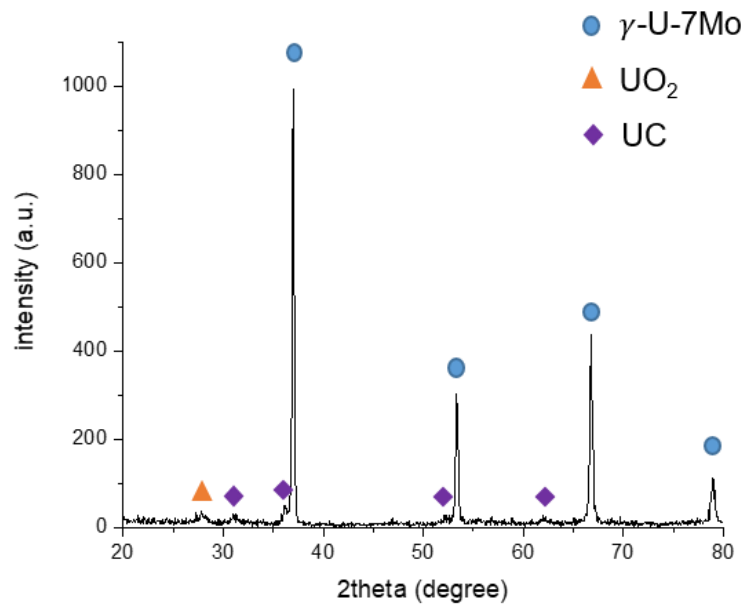


Figure 19. (a) Schematic representation of XRD experimental setup (left) and Bragg's law (right), and (b) XRD spectra [223].



**Figure 20. SEM SE top-view micrograph of 45–90  $\mu\text{m}$ -sized U-7Mo powders.**



**Figure 21. XRD profile of U-7Mo powders in the size range of 45–90  $\mu\text{m}$ .**

## **Chapter 3. Evolution of microstructure and residual stress of ZrN coating with coating growth**

Typically, the thickness of sputtered coatings affects the microstructure and residual stress which directly affect the mechanical characteristics including the fracture resistance, and thus play a critical role in determining the structural integrity during deposition and post-deposition processes (i.e., dispersion-fuel-plate fabrication). Particularly, if an excessive residual out-of-plane stress of an as-fabricated coating is induced in the process of being deposited, the mechanical failure (e.g., fatigue, creep, and brittle fracture) of the coating can occur even during deposition. Therefore, a comprehensive understanding of the evolution of microstructural and residual stress of the as-deposited ZrN coatings will be beneficial to understand the mechanical performance and structural failure behavior. However, there is also no work reported on the coating thickness effect on the microstructure and residual stress of ZrN coating on U-Mo powders.

In this chapter, ZrN coatings of various thicknesses ranging from mean 0.1 to 2.6  $\mu\text{m}$ , deposited on 45–90  $\mu\text{m}$ -sized U-7Mo powders by DC magnetron non-reactive sputtering technique, was characterized in terms of the microstructural properties and residual stress by using SEM, EDS, and XRD. Based the characterization results, the coating's structural integrity as well as diffusion barrier ability were estimated

### **3.1. Analysis results of as-deposited ZrN coatings**

#### **3.1.1. Coating thickness and deposition rate**

From the cross-sectional SEM image of Figure 22 and the EDS mapping image of Figure 23, it was evident that a U-7Mo powder was perfectly surrounded by a ZrN single coating layer with a uniform thickness. As an inherent limitation of EDS analysis, light atoms (atomic number < 11) such as nitrogen cannot be identified. As a result of the homogeneous coating thickness, the ZrN coated U-7Mo powder exhibited a constant brightness (intensity) over the powder in the stereoscopic SEM image of BSE mode (Figure 24). BSE images represent the mean composition over the several microns depth of the samples as an image intensity that increases with the average atomic number. Thus, the brightness of BSE images can provide information about relative coating-thicknesses.

As shown in Figure 25, the measured thickness of the as-fabricated ZrN coatings showed a linear function as a function of deposition time, while it deviated from the linear relation after the deposition time of 22 h. By plotting the coating thicknesses deposited for 1–22 h against the corresponding



deposition times, the deposition rate (i.e., the slope of the plot) of 2.5 nm/min was obtained. On the other hand, the ZrN coating deposited for 25 h exhibited an abnormally diminished mean thickness with a large standard deviation. This is suspected as a result of the inter-laminar delamination of the coatings on a part of the U-7Mo powders, as displayed in Figure 26. The delaminated coating surface predicted as the cross-sectional plane of the coating showed open voids between the coating columns. This suggests that an excessive internal stress had developed in the coating during deposition.

### 3.1.2. Morphology

By utilizing SEM, the morphology of the as-fabricated ZrN coatings with various thicknesses from mean 0.1 to 2.6  $\mu\text{m}$  was examined. In the case of the 2.6  $\mu\text{m}$ -thick ZrN coating, only the intact coating samples were selectively characterized to focus on the morphological evolution of the ZrN coating.

The fractured image of Figure 27 shows that the as-deposited ZrN coatings appear as a V-shaped columnar (or pillar) structure. This V-shaped column structure was in good agreement with the observed proportional relationship between the top dome size of coating columns and coating thickness (Figure 28). While the column domes could not be recognized in the SEM BSE top-view image for coatings up to 0.5  $\mu\text{m}$  thickness (possibly due to the dense structure without the column boundary gaps), the column width of tens of nanometers could be observed for the 0.8  $\mu\text{m}$ -thick coating. For coatings thicker than 0.8  $\mu\text{m}$ , the column width was from tens to hundreds of nanometers. Each the coating column was a bundle of fine nano-sized grains, as can be identified in the high magnification SEM BSE image of Figure 29.

Additionally, as displayed in Figure 28, the thick ZrN coating appeared porous due to macroscopic open-void-type defects such as hillock, crater, pinhole, and column boundary gap (i.e., open-voids along column boundaries), which is in contrast to the dense thin coating without those defects. As can be seen in Figure 30 (a), the hillock was a micron-sized agglomerate protruding from the coating surface, and is also referred to as nodule [106], peak [107], cone [107], or cauliflower defect [107] because of its shape. It was observed by SEM image analysis that the hillock was connected to the surrounding coating by a discontinuous plane, resulting in its weak adhesion with the coating. As a result, it easily spalled off from the coating, and eventually a micro-sized hole named crater is generated. As shown in Figure 30 (b), the crater was a macroscopic (1–3  $\mu\text{m}$  in the width) cone-shaped open-void sparsely distributed over the coating, while the pinhole was a nano-sized (0.05–0.5  $\mu\text{m}$  in the width) columnar open-void of a uniform distribution. On the other hand, as shown in Figure 28, the coatings thinner than 0.5  $\mu\text{m}$  were dense without an observable column-boundary gap (i.e., open-voids along column boundaries). However, the column-boundary gap seemed to increase with increasing coating

thickness after having been initially detected at 0.8  $\mu\text{m}$  thickness. From the observation, it can be suggested that the column boundary gap is a V-shaped long open-void. Likewise, the defects were observed in the surface of the coatings from a certain thickness: 0.5  $\mu\text{m}$  for hillock, and 0.8  $\mu\text{m}$  for crater, pinhole, and column boundary gap. Hence, it is deduced that a dense-to-porous structural transformation of the ZrN coating occurred at a thickness between 0.2 and 0.5  $\mu\text{m}$ .

### 3.1.3. Texture

Figure 31 is the XRD profiles of the 45–90  $\mu\text{m}$ -sized U-7Mo powders coated with a ZrN thin layer with different thicknesses. Excluding the substrate-related phases (i.e., U-7Mo,  $\text{UO}_2$ , and UC), only ZrN mono-phase was identified without the ZrN-associated oxide phase (e.g.,  $\text{ZrO}_2$ ) and other stoichiometric phases (e.g.,  $\text{Zr}_3\text{N}_4$ ). The ZrN reflection peaks at (111), (200), (220), (311), and (222) corresponded to  $2\theta \approx 34^\circ, 37^\circ, 57^\circ$ , and  $68^\circ$ , respectively, and were indexed to the NaCl structure of the International Centre for Diffraction Data (ICDD) card no. 00-035-0753 [103]. The crystal structure data of the coatings are listed in Table 7.

Curiously, sharper ZrN peaks were observed in the XRD profiles with the increasing coating thickness, which implied that the crystallinity (i.e., the degree of structural order) of the ZrN coating increased during its growth. The broader peak suggested that the corresponding crystallographic plane had a relatively extensive distribution of  $d$ -spacing rather than a single  $d$ -spacing owing to non-uniform lattice distortions triggered by the surface tension of nanocrystals and interstitial impurities. In contrast, the sharp peak implied that the corresponding plane was under uniform macrostrain.

On the other hand, the peak intensity provides information about the coating texture, i.e., the spatial distribution of the corresponding phase. The texture is usually characterized by the texture coefficient  $TC_{(hkl)}$  (see Eq. (9)), representing the probability of the corresponding (hkl) crystallographic-plane. As described in Figure 32, the 0.1  $\mu\text{m}$ -thick coating exhibited a single crystal structure with only the (002) plane, while the other coatings with a thickness greater than 0.1  $\mu\text{m}$  showed a similar texture, representing a polycrystalline structure of a random orientation with the most dominant (111) plane.

### 3.1.4. Lattice parameter and density

Figure 33 shows the measured lattice constant and calculated density of the ZrN coatings with various coating thicknesses. The lattice constant (lattice parameter) of the ZrN coatings was by using Bragg's law (Eq. (9)) and Eq. (12), and the coating density was calculated with the obtained lattice constant and known molar mass (105.23 g/mol for ZrN [103]) according to Eq.(13). The measured lattice constants (4.4247–4.5573 Å) of all the ZrN coatings were smaller than the standard value of 4.570 Å [103], which implied the contracted lattice structure in the z-axis direction (i.e., out-of-plane or growth direction of the ZrN coating). Thus, all of the calculated coating densities were greater than the standard value of 7.09 g/cm<sup>3</sup> for bulk ZrN [108]. However, it should be noted that the calculated densities are just a value that does not account for the observed coating defects such as hillock, pinhole, and column boundary gap.

### 3.1.5. Grain size and microstrain

Generally, the XRD peak width are determined not only by the crystallinity but also the average grain size and microstrain (lattice strain). These parameters were obtained by the Halder-Wagner method (Eq. (11)), which is a reliable and advanced method for nanostructured samples (grain size <100 nm). As presented in Figure 34, by constructing a linear plot of  $\beta^2/\tan^2\theta$  against  $\beta/(\tan\theta \cdot \sin\theta)$ , grain size (D) and microstrain ( $\eta$ ) were calculated by using the slope of  $K\lambda/D$  and the y-intercept of  $\eta^2$ . The obtained results presented in Figure 35 showed that the ZrN coatings, with the exception of the 0.1  $\mu\text{m}$ -thick coating, showed the grain size increase from 2 to 6 nm, but consistently zero microstrain with increasing the coating thickness. On the other hand, the 0.1  $\mu\text{m}$ -thick coating displayed an abnormally large grain size and microstrain, which is probably due to the measurement error originating from the highly non-uniform lattice distortion of the coating.

### 3.1.6. Residual stress

The as-fabricated ZrN coatings were evaluated in terms of the residual stress since it is an important parameter to determine their structural reliability during fabrication and irradiation. For thin coatings, their residual stress is typically measured by XRD analysis using the  $\sin^2\Psi$  method [101–104]. However, as the measurement technique can only be applied to the samples with a flat surface, it is inappropriate for our sphere-shaped samples. Instead, I performed a XRD analysis method using macrostrain, as described in Eqs. (14) and (15).

As can be identified in the XRD profile of Figure 31, all the peak positions corresponding to the (200) diffraction plane of the ZrN phase were shifted either left or right from the standard value indicated by a dotted line [103]. This indicated that all of the ZrN coatings possessed a negative or positive strain in the z-axis direction (known as out-of-plane direction) at the measurement temperature (i.e., room temperature). As can be seen in Eq. (15), the negative strain in the out-of-plane direction of the coating is a result of the positive transverse strain (i.e., a tensile in-plane stress). In contrast, the positive strain in the out-of-plane direction was attributed to a compressive in-plane stress. The residual stress in the x-direction ( $\sigma_x$ ), calculated according to Eq. (15) for the ZrN coatings, is illustrated in Figure 36. It was found that the obtained residual stress of the ZrN coatings changed from  $-2.1$  to  $0.3$  GPa depending on the coating thickness. The residual compressive stress was relaxed up to  $0.5 \mu\text{m}$  thickness, and a nearly neutral stress state was exhibited for the coatings with a thickness greater than  $0.5 \mu\text{m}$ .

## 3.2. Discussion

### 3.2.1. Microstructural evolution trends of the as-fabricated ZrN coating during growth

The EDS mapping (Figure 23) and XRD pattern (Figure 31) confirms that the as-deposited coatings ZrN single phase without other unexpected phases (e.g., Zr, ZrO<sub>2</sub>, Zr<sub>3</sub>N<sub>4</sub>) were successfully deposited under the chosen deposition conditions (Table 6).

It is well known that coating microstructure is determined by the deposition method and deposition parameters such as applied power, substrate temperature, deposition chamber pressure, working gas type, incidence angle of sputtered atoms/molecules, and distance between target and substrate. Consequently, they also affect the microstructure-dependent properties (e.g., chemical, thermal, and mechanical properties, residual stress) and functional performances (e.g., barrier capability, corrosion resistance, permeation rate of fission gases, fracture resistance) of the corresponding coating [62, 69, 105–111].

Typically, sputtered coatings exhibit a fine-columnar structure consisting of nano-sized crystallites because of the limited mobility of adatoms (i.e., movable atoms or molecules arriving at the substrate surface) due to the low deposition temperature (normally, ~300°C). According to Thornton's structure zone model (SZM) [70], the sputtered coatings deposited at low temperatures ( $T_h < 0.3$ ; where  $T_h$  is the ratio of the melting point of a coating material to the deposition temperature) show Zone I structure or Zone T structure depending on the Ar working pressure. The SZM is a practical guideline to categorize the morphology of magnetron-sputtered coatings as a function of  $T_h$  and working pressure (P). The deposition condition of the ZrN coating in this study (i.e.,  $T_h = 0.16$ ,  $P = 2$  mTorr) lies in the deposition environment of the Zone T structure (i.e.,  $T_h < 0.3$ ,  $P < 10$  mTorr).

At this deposition condition, the most effective diffusion-mechanism is surface diffusion for adatoms, and hence thermodynamically-stable grains mainly grow by trapping the relatively unstable neighboring grains during deposition, which is referred to as “competitive grain-growth” or “grain coalescence” [112–117]. Thermodynamically, the grain-growth naturally occurs by interatomic forces to decrease the total free-surface energy (or grain-boundary energy) of the coating system until the local grain size develops sufficiently and the grain boundaries are immovable [90]. During the competitive-growth of coatings with Zone T structure, the coating microstructure grown for a certain duration is various relying on the coating evolution level (i.e., the coating thickness). Consequently, Zone T structure shows a continuous change in the coating microstructure characterized with surface and cross-sectional morphology, texture, and grain size, and hence residual macroscopic stress during growth. consequently the coatings with Zone T structure generally exhibit a continuous change in the morphology, grain size, texture, surface topography, and so stress state during the coating growth [90].

Geometrically, energetically-favourable grains grow fast by capturing neighbouring adatoms is expected to form V-formed grains and grain columns (a grain column is a bundle of grains) where the grain-width increases proportionally with the coating thickness. This is in good accordance with the SEM examination results (Figure 27 and Figure 28) and the obtained grain-size trend (Figure 35) of the ZrN coatings. As seen in Figure 28, the coating grains also showed a V-shaped configuration with monotonically increasing column-dome size in proportion to the coating thickness. Since the grain-growth of the coating proceeded thermodynamically during deposition under the employed deposition conditions, the grain size was expected to be proportional to the time elapsed for grain-growth (i.e., deposition time), and thus the coating thickness [125]. The grain size of the ZrN coatings prepared in this study increased from 2 to 6 nm as the coating thickness increased from 0.2 to 2.6  $\mu\text{m}$ . This proportional relationship of the grain size and coating thickness was in good accordance with the experimental results of non-reactively sputtered ZrN coatings by Huang et al. [126]. These authors deposited ZrN coatings on a Si substrate by an ion plating machine under certain deposition conditions (Ar environment of 1–2 Torr pressure, negative substrate bias voltage of  $-60$  V, and gun power of 6 kW). The ZrN coating showed an increased in the grain size from 11 to 17 nm, as the coating thickness increased from 0.16 to 0.99  $\mu\text{m}$  thickness [126].

As can be seen in the surface topography of the ZrN coatings (Figure 28), the column-boundary gap (i.e., open void between columns) size, as well as the column-dome size, mostly increased with the increasing coating thickness. The first coating that allowed analysis was 0.8  $\mu\text{m}$  thickness. When the coating thickness was either less or equal to 0.5  $\mu\text{m}$ , the SEM BSE image did not reveal any coating columns separated by column boundaries, probably because of their fine dense structure without any detectable column boundaries. At the critical thickness of 0.8  $\mu\text{m}$ , it was suggested that the coating columns had developed a sufficient size (i.e., length and width) so as to cause the atomic shadowing effect, which refers to the flux of the sputtering material being blocked by already-grown coating columns during deposition. The blocked area is inhibited from coating growth, and eventually remains an open void surrounded by columns blocking the sputtering flux. It is worth noting that the U-7Mo powder substrate, with its convex curved surface, enhanced the atomic shadowing effect by decreasing the incident angle of sputtered atoms, and was consequently more likely to form intercolumnar voids under the deposition condition of the sputtering machine where the adatoms had limited mobility. Additionally, it was expected that the column-induced shadowed region, where coating growth was suppressed, would increase in proportion to the column size. Thus, in the case of the ZrN coatings consisting of V-shaped columns, the growth-suppressed region, i.e., column-boundary gap, and hence the roughness was proportional to the coating thickness. The surface image analysis of the ZrN coatings (Figure 28) revealed that the columns appeared as the long sharp V-shaped form distinguished by the column-boundary gaps starting from 0.8  $\mu\text{m}$  coating thickness. The non-reactively sputtered ZrN

coatings prepared in this study exhibited similar morphological characteristics as that of the reactively-sputtered ZrN coating [127]. The TEM transverse cross-sectional image analysis revealed that the reactively-sputtered ZrN coatings of thickness greater than 0.2  $\mu\text{m}$  exhibited a V-shaped columnar structure composed of very fine (diameter of tens of nanometers) grains, and sharp V-shaped columnar-boundary gaps [127].

Another thickness-dependent morphological change observed for the ZrN coating was the appearance of unique defects such as hillock, crater, and pinhole. As presented in Figure 28, the defects were suddenly detected over the surface of the coatings with thickness over 0.5  $\mu\text{m}$ . For sputtered coatings, the defect formation during deposition is inherently hard to prevent. Hillock is a micron-sized cauliflower-like defect protruded over coating. It is known that a hillock is a relaxation form of the induced highly compressive macrostress in the coating's in-plane direction (i.e., the direction perpendicular to coating growth direction). Typically, a sputtered coating tends to possess a compressive macroscopic stress due to the accumulation of lattice defects created by the collisions of high-energy Ar ions with growing-coating's surface during deposition. If the compressive macroscopic stress over coating exceeds a certain level, mass transfer of coating material starts along grain boundaries by surface diffusion mechanism in the out-of-plane direction of coating (i.e., coating growth direction), leading to generation of extruded hillock. In addition, the hillock weakly joining with adjacent grain-columns easily fall off from coating, and thus is likely to create an undesired micron-scale hole called "crater" (i.e., hillock-spalled form). The other defect, pinhole, is generated by the attachment of floating foreign materials called impurities on the surface of substrate and/or growing coating during deposition. The impurity physically affixed on substrate and growing coating with a weak adhesion strength is likely to be separated from the coating column on the impurity. The separated region becomes a fine-column-formed nanometer-scale open void. Based on their generation mechanisms mentioned above, the formation possibility of these defects is expected to rise with increasing the deposition time and hence coating thickness.

As presented in Figure 31 and Figure 32, the ZrN coatings showed a slight change in texture with increasing the coating thickness. The (200) crystal plane was remarkably dominant for the first 0.1  $\mu\text{m}$  coating thickness, and a similar orientation distribution with nearly random orientations (or weakly textured structure) was confirmed thereafter. From the almost consistent texture of the thick coatings (excluding the 0.1  $\mu\text{m}$ -thick ZrN coating), it was evident that the ZrN coating on the U-7Mo powder substrate had a quite stable growth pattern in spite of the high lattice mismatch between the ZrN coating and U-Mo substrate. Additionally, the weak textured structure of the coatings having a thickness greater than 0.1  $\mu\text{m}$  indicated that the orientation selection during grain coarsening was incomplete under the chosen deposition conditions. The strongest peak (i.e., predominant orientation) among ZrN crystallographic planes changed from (002) to (111) diffraction plane as the coating thickness exceeded

0.1  $\mu\text{m}$ . Generally, the texture of a coating changes toward diminishing the total energy of the coating/substrate system. According to the texture development models based on thermodynamics [113], [114], it is expected that the ZrN coating with NaCl structure would initially exhibit (002) as the dominant orientation with the lowest surface energy [128], and then evolve toward (111) orientation as the coating thickness increased. This texture change can be explained with the development of intrinsic stress. In a high intrinsic stress state, the coating growth with (111) plane is thermodynamically favorable because the elastic potential energy of NaCl-structured coatings is the lowest in the [111] direction [129].



### 3.2.2. Influence of residual stress on the structural integrity of ZrN coating

The residual stresses of the ZrN coatings (Table 7 and Figure 36), which lay in the range of – 2.1 to 0.3 GPa, were dependent on the coating thicknesses. The initial compressive residual stress decreased to a nearly neutral stress state for the coating with up to 0.5  $\mu\text{m}$  thickness, and thereafter, the neutral stress was seemingly sustained.

The residual stress of the as-fabricated ZrN coatings is closely associated with the microstructural evolution through a series of growth steps that include nucleation, island growth, island coalescing, and coating growth. Each of these growth steps produces either compressive or tensile stresses with various magnitudes. Compressive residual stresses typically originate from atomic displacement and densification. The atomic peening mechanism occurring in sputtering systems generates local compressive stresses over the coating [115, 122–129]. Atomic peening is the phenomenon that leads to a locally distorted lattice structure because of the striking of working gas atoms and sputtered atoms with high bombardment energy onto the growing coating surface. Compressive stresses are produced as a consequence of the bombardment-induced damages giving rise to the densification of grains [134] and grain boundaries [123]. A high-vacuum deposition environment (i.e., low working pressure) increases the bombarding energy of the sputtered coating material and produces compressive residual stress over the resultant coating [127, 129].

Additionally, adatom diffusion also induces compressive stress by the combination of two mechanisms, i.e., the incorporation of supersaturated adatoms into grain boundaries where the atomic packing density is relatively low, and the resulting volume shrink [122, 123, 130]. From the view of thermodynamics, these two mechanisms are naturally driven to decrease the free-surface (grain boundary) after complete closing all the gaps between the neighboring islands. The formation energy of an adatom on the coating surface is greater than that in the self-interstitial position of the grain boundary. The migration of the excess sputtered adatoms into the grain boundaries occurs only under the high-mobility conditions for adatoms such as high deposition temperature, negative substrate biasing, low working pressure, and high applied-voltage. These high-mobile conditions for adatoms promote the structural change from a disordered low-density structure to an ordered high-density structure (i.e., densification or subsequent volume shrink), which is accompanied by the slight enhancement of compressive stress.

On the other hand, the intercolumnar voids formed at higher film thicknesses by the atomic shadowing effect generate a tensile stress by exerting the interatomic attractive force. Regarding the influence of a void on internal stress, transition metal nitrides (i.e., ZrN, TiN, and TiZrN) deposited by DC unbalanced magnetron reactive sputtering have been empirically researched by Abadias and Guerin

[139]. These authors found that the intercolumnar void leads to higher tensile stress with increasing coating thickness, and a compressive-to-tensile stress transition occurs at a specific coating thickness [139]. In addition, Proost and Spaepen have reported that voids relax the aluminium compressive growth-stress during electron-beam evaporation deposition on Si and sapphire substrates in the temperature range of 170–400°C [140].

It has been suggested that the internal stress is determined by three kinetically competing mechanisms for stress formation, namely, atomic peening effect and excessive adatom diffusion into grain boundaries that lead to compressive stress, and void formation that causes tensile stress mainly at high thickness regions. The thickness-dependent residual stress change of the ZrN coatings in this chapter (Figure 36) can be explained as follows. For dense inner coatings (0.1–0.2  $\mu\text{m}$  thickness), compressive stress is generated mainly because of coating densification by bombardment-induced damages (i.e., atomic-peening effect) and the diffusion of excessive adatoms into the grain boundaries. As the coating thickness increased from 0.1 to 0.5  $\mu\text{m}$ , relaxation of compressive stress occurred. This may be because of the suppression of adatom diffusion toward grain boundaries, resulting from the existing compressive stress and the resulting increased chemical-potential at the grain boundaries. Moreover, the formed intercolumnar porosity from 0.8  $\mu\text{m}$  thickness (Figure 26) enhances the relaxation of compressive stress.

In mechanical engineering coating design, the developed residual stress should be considered to ensure the structural reliability of the coating during deposition and post-deposition processes (e.g., manufacturing, service time). The coating will fail if its stress, i.e., the sum of internal stresses or residual stress and external stress, exceeds its yield strength. Thus, the residual stress produced during the deposition of a coating is a key factor that determines its structural integrity during the post-deposition processes.

Moreover, depending on the sign, magnitude, and through-thickness distribution of the residual stress over coating, the coating can fail even during deposition. As can be seen in Figure 26, the ZrN coating deposited for 25 h showed an interlaminar-delamination behavior even though no artificial external stress was applied to the coating. Thus, the delamination was likely triggered by the residual in-plane stress in the coating. Generally, delamination is followed by the buckling induced by excessive compressive residual stress working in the in-plane direction. The generated local delamination can propagate along the plane parallel to the substrate surface, that is, coating/substrate interface or interlaminar plane, which is determined by the propagated plane. Uniform compressive stress beyond adhesion strength induces the delamination propagation into the interface of substrate and coating, whereas the non-uniform tensile stress causes interlaminar delamination because of interlaminar shear stress (i.e., the variation of residual in-plane stress) exceeding the interlaminar shear strength. As column-boundary gaps were observed over the delaminated ZrN coating surface as can be seen in Figure

26, it can be suggested that the interlaminar delamination occurred along the coating plane at least 0.8  $\mu\text{m}$  away from the substrate surface, based on the images of the coating surface (Figure 28). Therefore, considering the measured residual stress evolution (Figure 36) together with the predicted delaminated plane (at least 0.8  $\mu\text{m}$  from the substrate surface) of the ZrN coating, it is suspected that the interlaminar delamination was produced by the interlaminar shear stress along the coating plane at a distance of 2.2  $\mu\text{m}$  from the substrate surface. With respect to the coating plane, the outer-coating layer had a compressive stress, whereas the inner-coating layer possesses a tensile stress. Consequently, the outer layer was buckled and then delaminated because of interlaminar shear stress exceeding the interlaminar shear strength. This delamination phenomenon limited the thickness of the ZrN coating that can be deposited. The ZrN non-reactive sputtered coating in this study can be deposited is 2.2  $\mu\text{m}$ .

### 3.2.3. Optimum thickness of ZrN coating based on the analyzed microstructure

It is well known that coating microstructure determines the properties and functional performance including diffusion barrier ability. As already mentioned, the ZrN coating with the Zone T structure prepared in this study showed a continuous microstructural change depending on the coating thickness. Therefore, I attempted to assess the ideal ZrN coating thickness that would exhibit the greatest diffusion barrier capability based on the observed structural characteristics of the coatings.

The most important condition for good barrier performance is that the ZrN coating must have a microstructure without any macroscopic defects (e.g., crater, hillock, column boundary gap, pinhole, etc.), large grains (i.e., low grain boundary density), and narrow lattice spacing (i.e., compacted d-spacing). The macroscopic defects and grain boundary can facilitate material diffusion by allowing surface diffusion and grain boundary diffusion of solid materials, respectively. In addition, the lattice spacing of the diffusion barrier coatings is inversely proportional to the activation energy for the volume diffusion of materials. Thus, a larger lattice spacing implies lower diffusion barrier performance.

In the present study, various macro-/mesoscopic defects appeared over the surface of the ZrN coatings with a thickness greater than 0.5  $\mu\text{m}$  (Figure 28), which was also identified in our previous research [62]. As the grain size of the ZrN coating increased with the increasing thickness (Figure 35), the density of the grain boundary was decreased. Additionally, the lattice spacing (i.e., lattice constant) decreased to the lowest value of 4.5247  $\text{\AA}$  up to an initial thickness of 0.2  $\mu\text{m}$ , increasing sharply up to the coating thickness of 1.0  $\mu\text{m}$ , and then slightly decreased afterwards (Figure 33). The rate of diffusion into and through a material increases in the order bulk diffusion < grain boundary diffusion < surface diffusion. Thus, judging the diffusion barrier capacity of the ZrN coating based on its microstructure, it would seem that the 2.6  $\mu\text{m}$ -thick coating with the largest grain size and lowest grain boundary density was the best in spite of the relatively large lattice spacing and macroscopic defects appearing over the coating thickness range of 0.5–2.6  $\mu\text{m}$ .

However, in order to properly function as a diffusion barrier, the ZrN coating should be structurally intact during the post-deposition processing (i.e., dispersion-fuel-plate fabrication). Generally, a dispersion fuel plate is fabricated through a sequence of steps including compacting, assembling, welding, hot-rolling, blister test, cold-rolling, trimming, and inspecting. These processes can damage the coating on the U-Mo powders because mechanical or thermal external forces are applied. Moreover, fracture behavior of coatings is generally dependent on coating thickness itself and thickness-dependent coating microstructure which significantly affect the mechanical properties, including fracture strength. It has been demonstrated by experiment and finite element simulation in our previous study [62] that the fracture behavior of non-reactively sputtered ZrN coating on U-7Mo

powders relies on the coating thickness at 500°C (i.e., a typical heat-treatment temperature of fuel fabrication), where a tensile thermal in-plane stress is motivated in the coating because the annealing temperature is higher than the deposition temperature (250°C) and the thermal expansion coefficient of the coating is lower than that of the U-7Mo substrate. The simulation results indicated that the ZrN coatings of thicknesses 740 and 731 nm respectively for 45 and 90 μm-sized U-7Mo powders were vertically cracked through the whole coating thickness (called through-thickness cracking) at 500°C, which was in good agreement with the corresponding experimental results. It was supposed that the through-thickness cracking was triggered by crack propagation from the surface crack generated in the porous outer coating layer starting from the 0.5 μm coating thickness. Normally, the porous outer coating layer with macroscopic defects is easily fractured as compared to the dense inner coating layer owing to its low packing density, which leads to the degradation of its fracture resistance. The resulting surface crack through the porous outer-layer can trigger through-thickness cracking by working as a crack tip where induced-stresses are concentrated. From the above thermal cracking result of the ZrN coating, it can be concluded that the porous outer-layer starting from the 0.5 μm coating thickness facilitates the through-thickness cracking during the fabrication processes of dispersion fuel plates.

The produced through-thickness cracks as well as the macroscopic defects significantly shorten the life time of the corresponding diffusion barrier coating by activating the surface diffusion mechanism of the materials. Generally, the diffusivity from the surface via the through-thickness crack is several orders of magnitude higher than the diffusivities corresponding to volume diffusion and grain boundary diffusion through the intact dense coating structure. The image analysis results of a heavy ion irradiation test [60] and an irradiation test [36] showed that a partial of the 1 μm-thick reactively-sputtered ZrN coatings in as-fabricated dispersion fuel plate samples were damaged locally, which was verified by an abnormally huge local IL at the interface of the U-Mo powder and Al matrix. The PIE results of the irradiated sample showed a massive IL with an “erupting volcano” shape in the fuel region irradiated by up to  $5.2 \times 10^{21}$  fissions/cm<sup>3</sup> [36]. It was speculated that through-thickness cracking of the ZrN coating had occurred during manufacture [37, 57].

There are three main diffusion mechanisms, namely, solution diffusion, Knudsen diffusion, and molecular diffusion, by which gases pass through porous solids depending on the pore size of the porous solids. Solution diffusion commonly takes place in the macroporous structure and the permeating gases diffuse through the macroscopic pores in a similar manner to the surface diffusion of a solid. In the case of a mesoporous structure with long pores that are 2–50 nm in diameter, Knudsen diffusion is prominent [141]. On the other hand, molecular diffusion primarily takes place in a microporous structure with small capillary pores of <2 nm diameter [142]. The kinetics of gas penetration increase in the order solution diffusion < Knudsen diffusion < molecular diffusion. On comparison of the sizes of the observed defects of the ZrN coatings, the crater is equivalent to the macropore, the pinhole and the

column-boundary gap are correlated to the mesopore, and the grain boundary can be considered as the micropore. The defects increase the gas penetration speed by allowing solution diffusion (crater), Knudsen diffusion (pinhole and the column-boundary gap), and molecular diffusion (grain boundary). It has been reported that the 1  $\mu\text{m}$ -thick ZrN reactively-sputtered coating has a porous outer-layer with tens of nanometer-sized column-boundary gaps starting from the 0.2  $\mu\text{m}$  coating thickness, and the porous outer-layer exhibits a much higher oxygen composition than the dense inner-layer [61]. Likewise, it can be expected that the through-thickness crack, which corresponds to a mesoscopic pore, also accelerates gas migration by acting as the most dominant gas path for the ZrN coating, and thus undesirably promotes the coating corrosion and the migration and coalescence of fission gases. The gas coalescence may accelerate the breakaway swelling of dispersion fuels.

Therefore, the main limitation for the practical application of the non-reactively sputtered ZrN coating in U-Mo/Al dispersion fuels is the through-thickness cracking of the coating triggered by the porous outer-layer with a relatively low fracture resistance. From the SEM surface image of the ZrN coatings (Figure 28), it was concluded that the most suitable thickness for the ZrN coating was between 0.2 and 0.5  $\mu\text{m}$ , where the coating structure was dense without any macro-/mesoscopic defects.

**Table 7. Summary of measured crystallographic properties of ZrN coatings.**

Deposition time	Mean thickness	Grain size	Lattice strain	$I_{111}/(I_{111}+I_{200}+I_{220}+I_{311}+I_{222})$	Lattice constant	Calculated density	Residual stress
(h)	( $\mu\text{m}$ )	( $\text{\AA}$ )	(%)		( $\text{\AA}$ )	( $\text{g/cm}^3$ )	(GPa)
1	0.1	66	0.23	0	4.5413	7.46	3.0
2	0.2	18	0	0.31	4.5247	7.54	1.1
4	0.5	27	0	0.41	4.5337	7.50	2.2
7	0.8	36	0	0.38	4.5533	7.40	4.4
10	1.0	30	0	0.39	4.5573	7.38	4.8
15	2.2	43	0	0.36	4.5527	7.41	4.2
25	2.6	64	0	0.43	4.5501	7.42	4.0

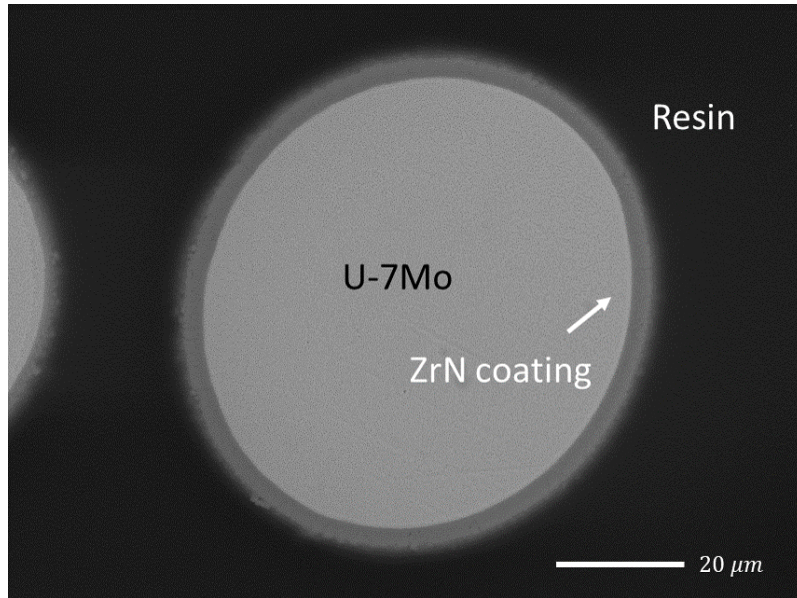


**Figure 22. SEM BSE cross-sectional image of mean 2.2 μm-thick ZrN coating on a U-7Mo powder.**



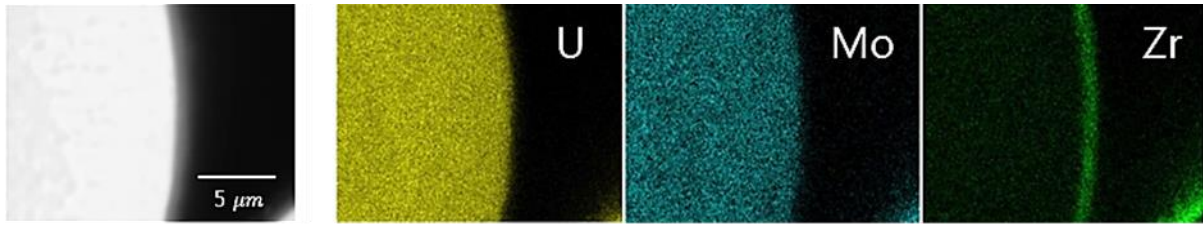


**Figure 23.** EDS mapping image of mean 2.2 μm-thick ZrN coating on a U-7Mo powder.

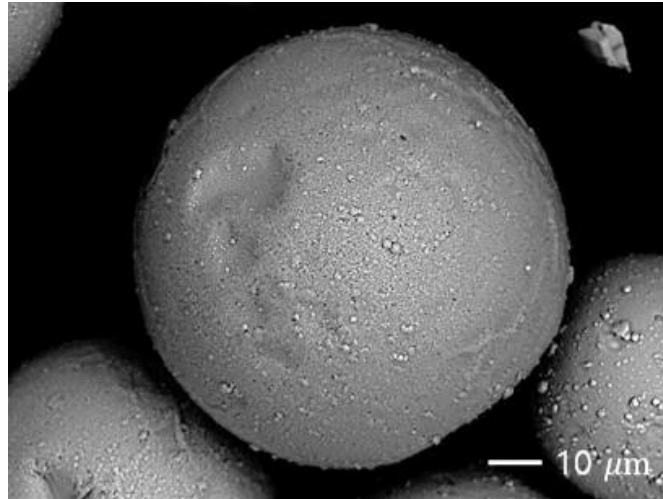


**Figure 24. SEM BSE top view image of U-7Mo powders coated with a mean 2.2  $\mu\text{m}$ -thick ZrN layer.**

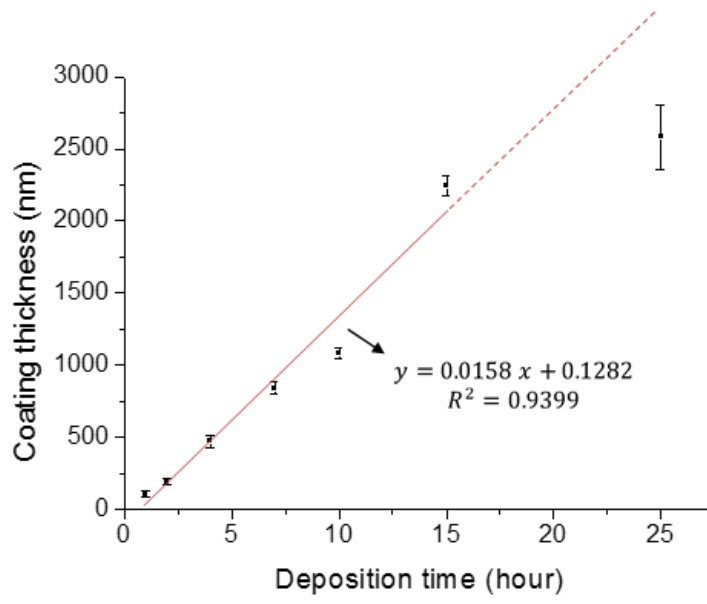
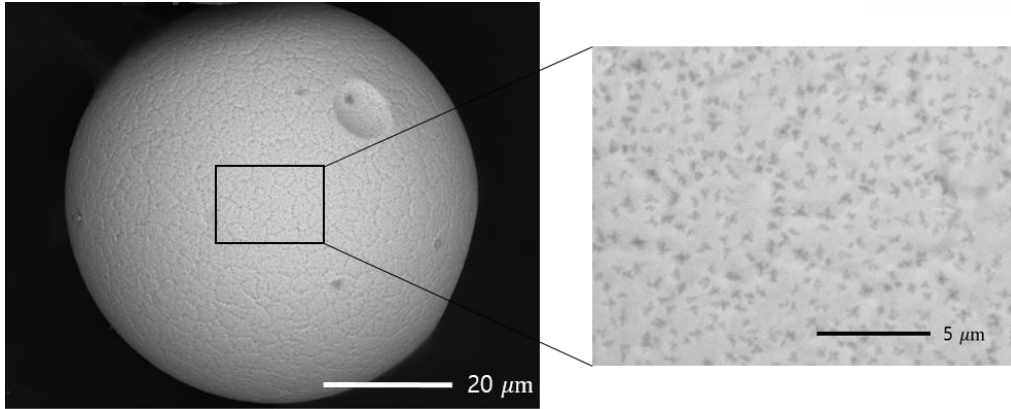
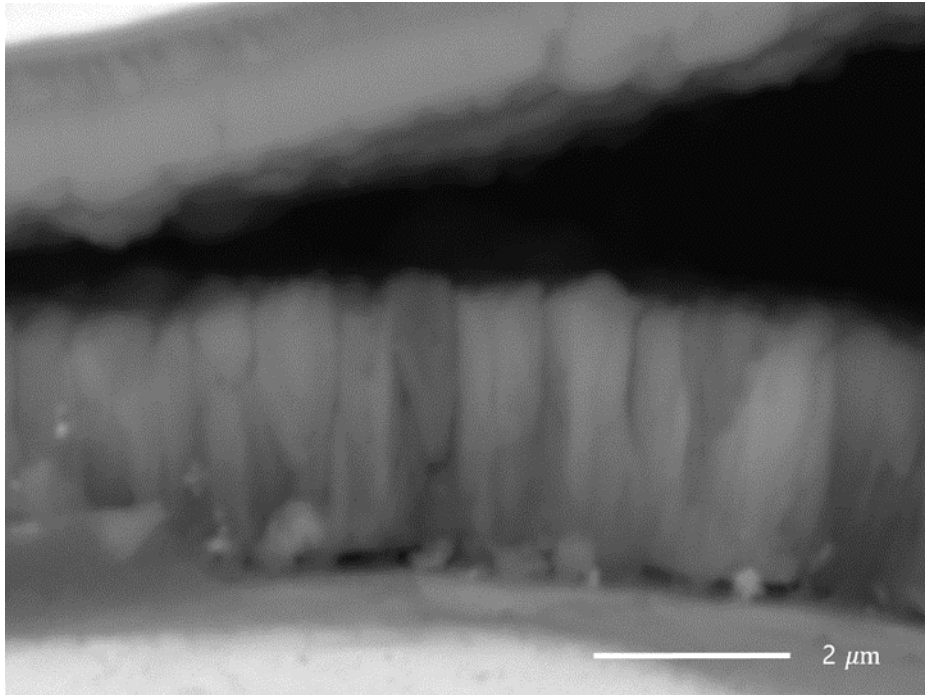


Figure 25. Plot of coating thickness against deposition time.



**Figure 26. Top view SEM BSE image of a mean 2.6 μm-thick ZrN coating showing laminar spallation.**



**Figure 27. SEM BSE fractured cross-sectional image of a 2.7 μm-thick ZrN coating.**

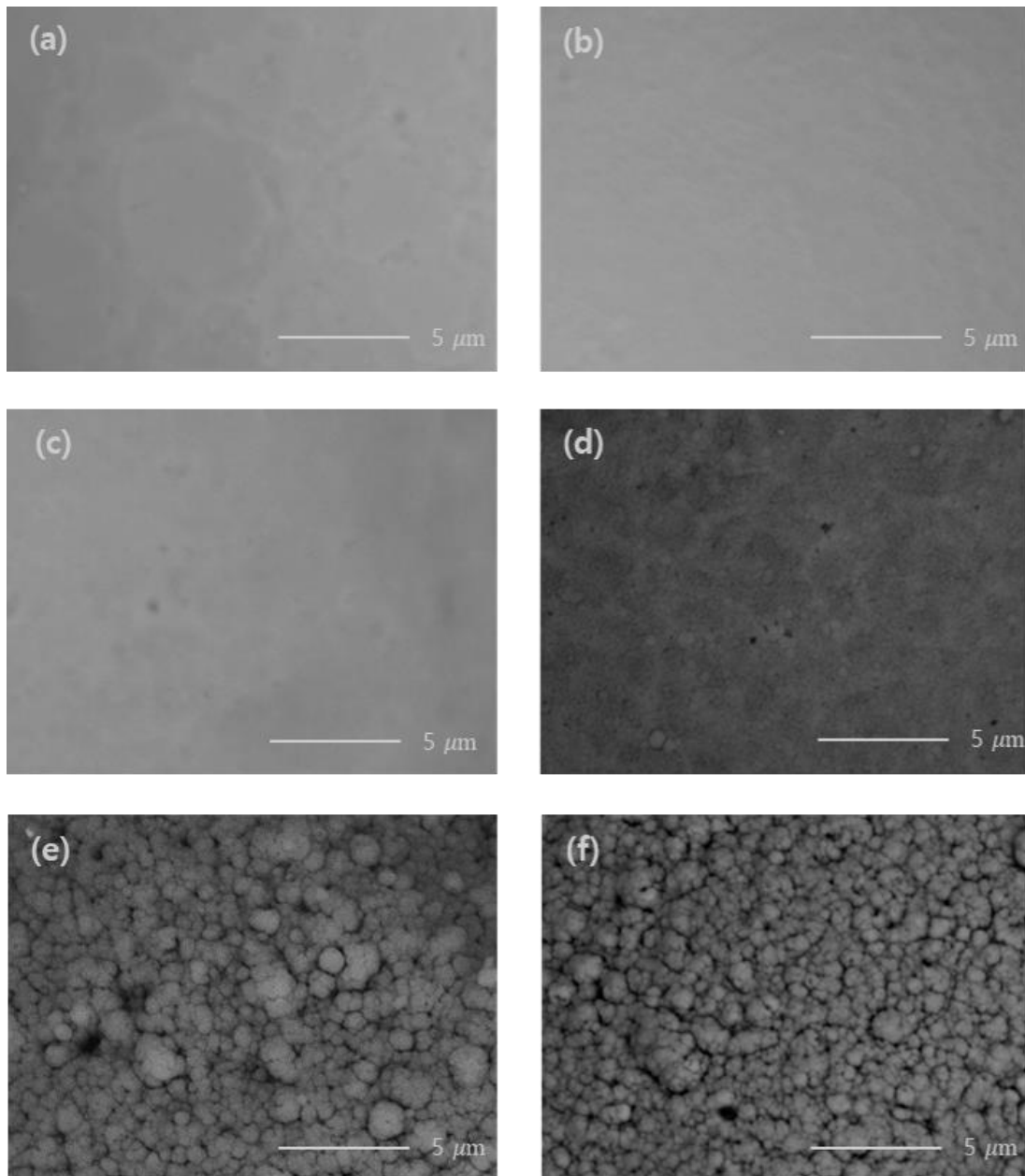


**Figure 28. SEM BSE top-view images of mean (a) 0.1, (b) 0.2, (c) 0.5, (d) 0.8, (e) 2.2, and (f) 2.6  $\mu\text{m}$ -thick ZrN coatings.**

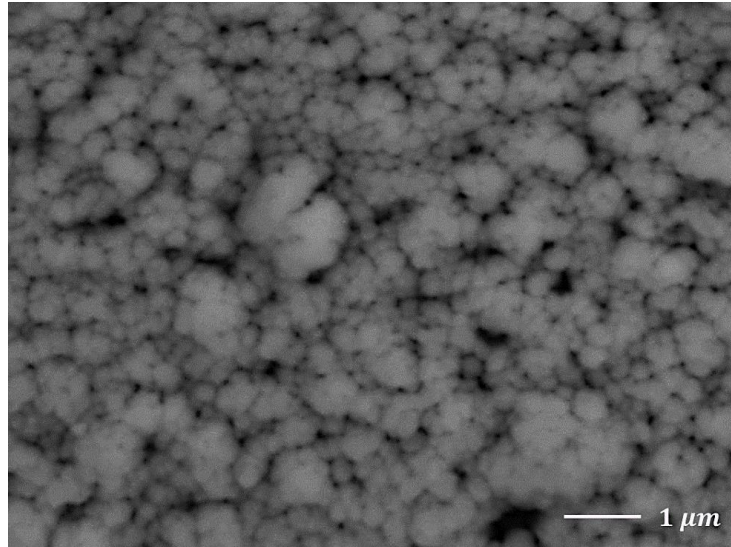


**Figure 29.** High magnification SEM BSE top-view image of a mean 2.6  $\mu\text{m}$ -thick ZrN coating.

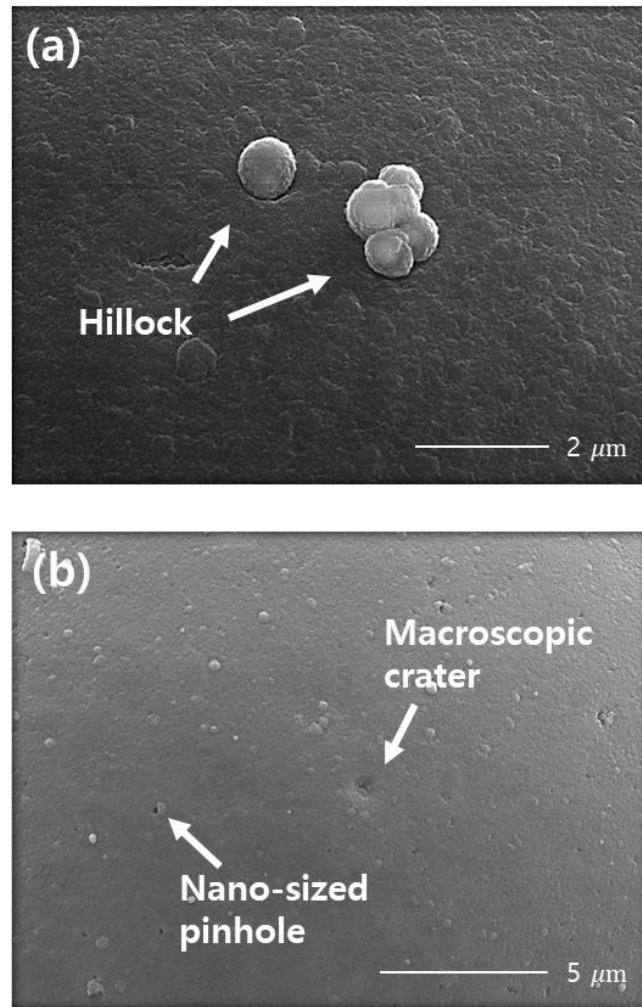


**Figure 30. Defect types detected in SEM SE top-view image of mean 0.8  $\mu\text{m}$ -thick ZrN coatings: (a) hillock and (b) pinhole & crater.**



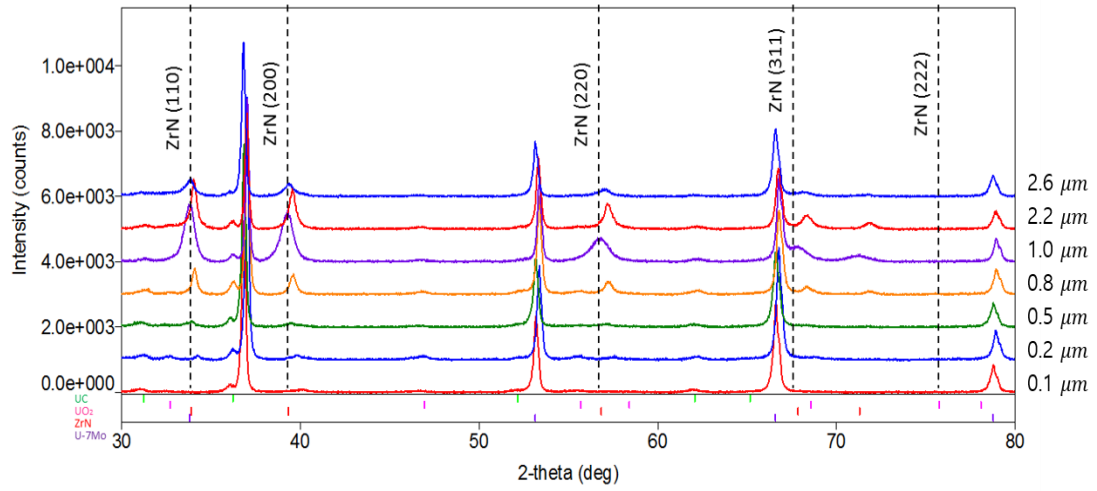


**Figure 31. XRD profiles of U-7Mo powders deposited with ZrN coatings of different thicknesses.**

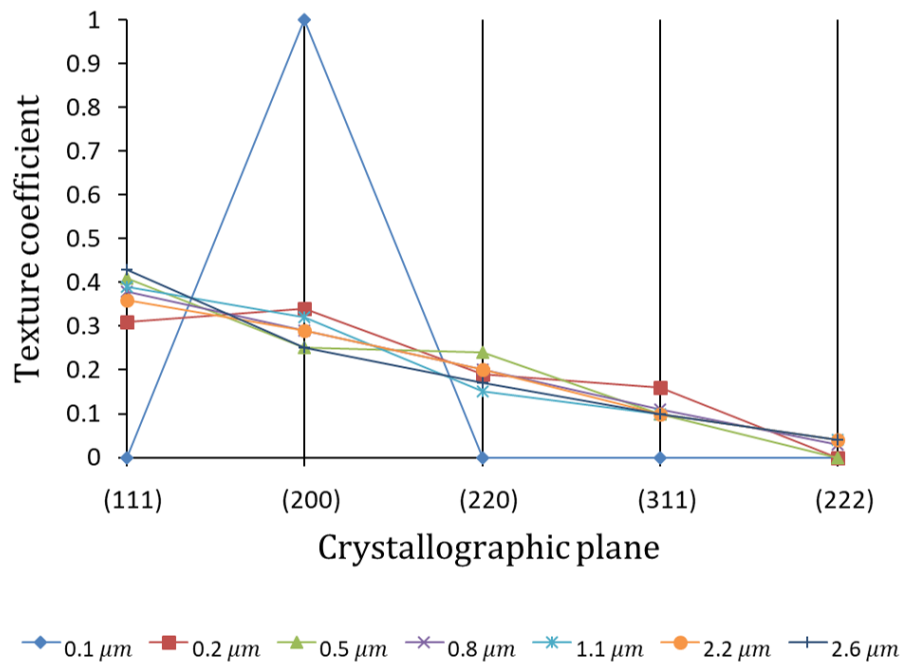


**Figure 32. Texture coefficient of ZrN coatings as a function of coating thickness.**

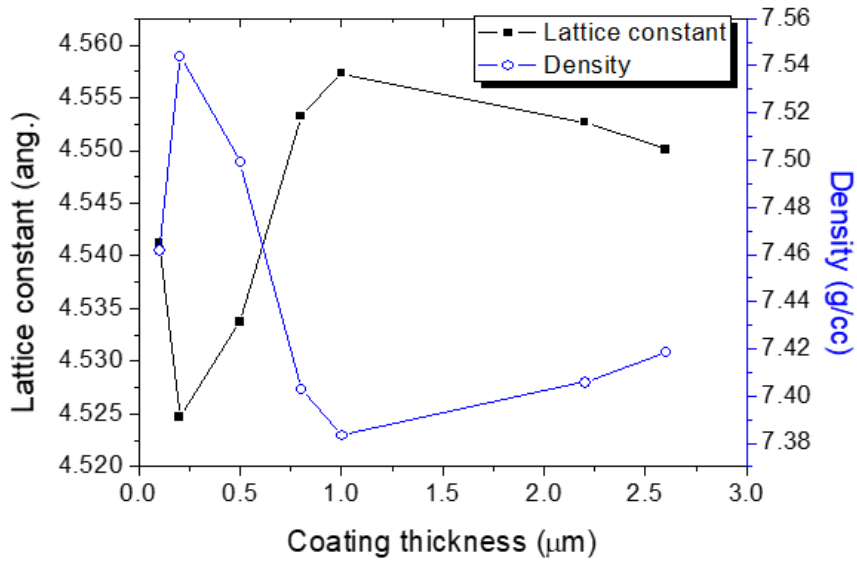


Figure 33. Lattice constant and calculated density of ZrN coatings with different thicknesses.

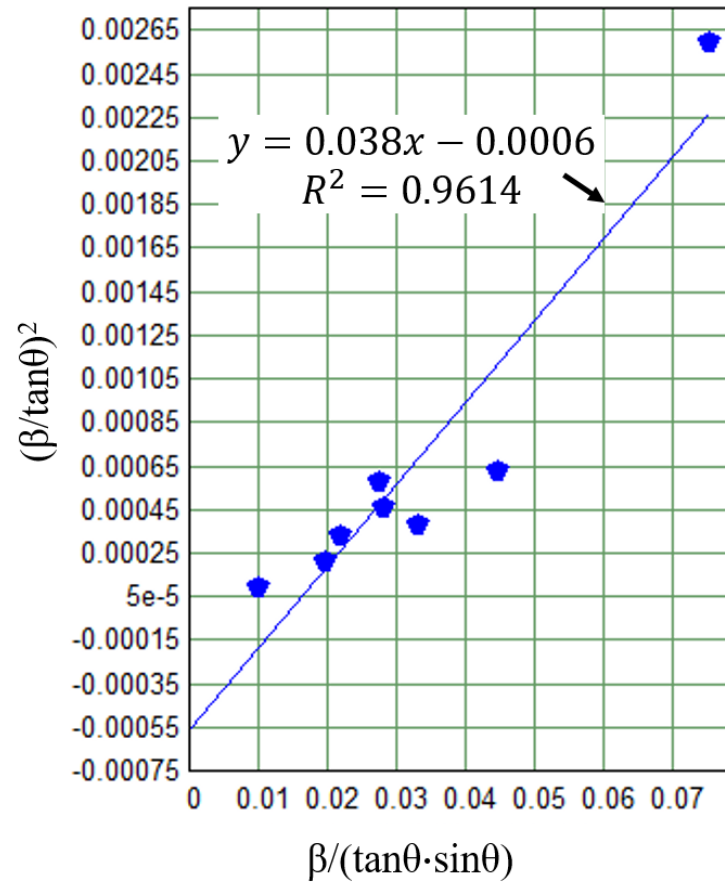


Figure 34. Halder-Wagner plot with slope of  $K\lambda/D$  and y-intercept of  $\eta^2$ .

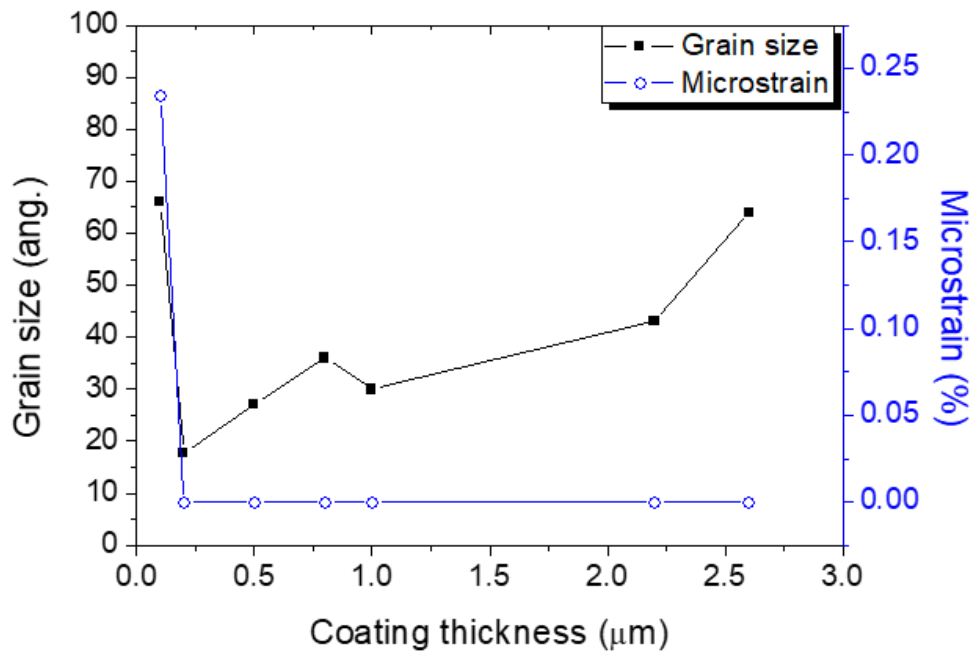


Figure 35. Grain size and lattice strain obtained by Halder-Wagner plotting.

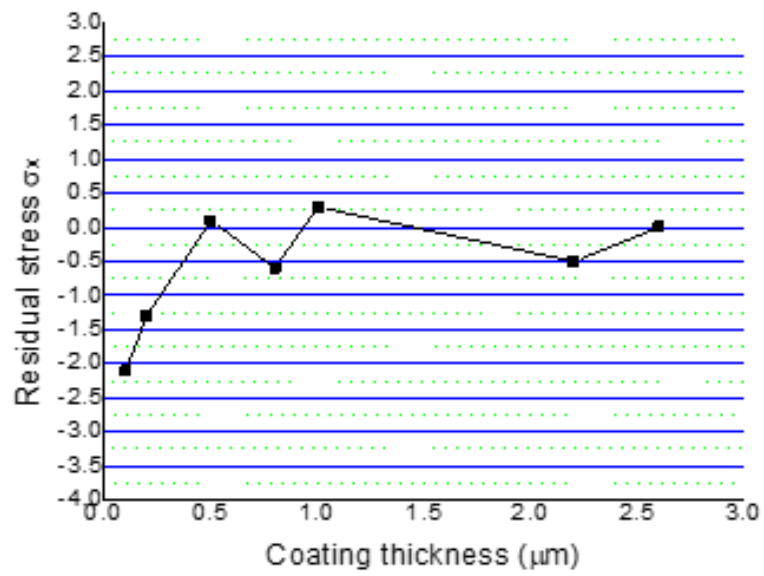


Figure 36. Residual stress evolution of ZrN coatings.

## Chapter 4. Effect of U-7Mo substrate size on thickness and microstructure of ZrN sputtered coatings

For diffusion barrier coatings, their structural homogeneity properties is a required characteristic because the coating structure has a great effect on their structure-based properties including the fracture resistance and diffusion barrier performance. However, it was reported that ZrN coatings, deposited on U-7Mo powders with different sizes (normally, 45–90  $\mu\text{m}$ ) by a RF reactive magnetron sputtering machine (called “STEPS & DRUMS”), showed a large variety of the coating thicknesses [62, 68, 75]. In the case of mean 1  $\mu\text{m}$ -thick ZrN coatings, the coating thickness varied from 2 to 4 times [62, 68, 75]. It was supposed that the coating thickness variation was attributed to the non-uniform size of the U-7Mo substrate powders or a measurement error originating from the different observation planes for each the coated powder [68]. I identified by empirical researches that various sputtered coatings (e.g., Mo, Zr, Ti, and ZrN coatings) deposited on 45–90  $\mu\text{m}$  U-7Mo powders showed various coating thicknesses depending on the U-7Mo powder size. Unfortunately, there is no existing study on the dependence of ZrN coating thickness on the U-7Mo substrate size.

This chapter is aimed to investigate the dependence of ZrN coating microstructure on U-7Mo substrate size. As-fabricated ZrN coatings on U-7Mo powders of various sizes were examined in terms of the microstructural properties by using SEM, EDS, and XRD. Based on the examination results, the fracture resistance and diffusion barrier ability of the coatings were estimated. In addition, a new semi-analytical model to predict ZrN coating thickness from the substrate size was established by studying the friction behavior of U-7Mo powders and the structure and coating deposition mechanisms of the used coating deposition machine.

### 4.1. Examination results of ZrN coatings

#### 4.1.1. Coating thickness

A single layer of average 0.9  $\mu\text{m}$ -thick ZrN coating was successfully deposited on 45–90  $\mu\text{m}$ -sized U-7Mo atomized-powders by a DC magnetron non-reactive sputtering machine. Figure 37 is the EDS mapping analysis results of the ZrN-coated U-7Mo powders. Zr-atom distribution in the EDS results identifies that the ZrN coating perfectly surrounds a U-7Mo powder with a homogenous thickness. On the other hand, nitrogen atoms of the ZrN coating layer were not noticed owing to a EDS's detection limit (i.e., atomic number >11). As well as the EDS results, a uniform thicknesses of the ZrN coating over a U-7Mo powder was confirmed by the coating thickness measurements. Per the coated powder, the coating thickness was randomly measured at 4 points in SEM SE cross-sectional

images of  $\sim 2 \times 10^4$  magnification. The coating thicknesses measured in one coated powder was nearly the same. Their deviation was smaller than the measurement error (typically,  $< 50$  nm) of the used conventional SEM.

However, as displayed in Figure 38, even though all the coatings had been deposited on the powders simultaneously, the ZrN coatings on the 45–90  $\mu\text{m}$ -sized U-7Mo powders varied in thickness with the substrate powder size. Per specimen, its coating thickness was randomly measured 20 times at one site per the ZrN-coated U-7Mo powder in the cross-sectional SEM SE images of  $2 \times 10^4$  magnification. This high magnification permits the coating thickness's accurate measurement with a high nanometer accuracy. But, it should be noted that the measured thicknesses is not the true thicknesses if the polished plane (i.e., observation plane) of a powder specimen does not intercept its equator. Accordingly, to minimize measurement errors caused by observation planes other than the equatorial plane, mounted ZrN-coated powders were polished until the cross-section sizes of the powders observed in the exposed plane were within a certain size range. In order to reach the equator of each 45, 53, 63, 75 and 90  $\mu\text{m}$ -sized U-7Mo powder, the powders of  $< 45$ , 45–53, 53–63, 63–75, and 75–90  $\mu\text{m}$  in size range were polished until the powders of the maximum size (i.e. 45, 53, 63, 75, and 90  $\mu\text{m}$ , respectively) were seen in the polished plane. The powders of  $< 45$   $\mu\text{m}$  were present in a very small quantity. As well as the coating thickness, the deposition rate, calculated by dividing the measured average coating thickness by the total deposition time, also depended on the substrate size. The thickness and deposition rate of the ZrN coatings increased as the substrate size increased. The measured average coating thickness of 90  $\mu\text{m}$ -sized powders was approximately twice as thick as that of 45  $\mu\text{m}$ -sized powders, which is in good accordance with the previously reported results [61, 81]. Keiser [61] observed that ZrN coatings with an average thickness of 1  $\mu\text{m}$ , deposited on average 70  $\mu\text{m}$ -sized U-7Mo atomized powders by a RF magnetron non-reactive sputtering machine, exhibited a variety of thicknesses ranging from 0.8 to 1.5  $\mu\text{m}$ .

The coating thickness increase with the substrate size could be reconfirmed in the SEM BSE surficial images of Figure 39. Generally, BSE image analysis is a very useful analysis method that provides high-resolution compositional information of samples, since local points in a sample consisting of higher mean-atomic-number materials within a few micrometer depth appear relatively darker (lower intensity) in the BSE image. Therefore, in the case of ZrN (i.e., coating material) is lesser in mean-atomic-number than U-7Mo (i.e., substrate material), it can be predicted that larger powders showing darker color in the BSE image of Figure 39 have a relatively thicker coating layer.



#### 4.1.2. Surface topology

Figure 40 identifies that the ZrN coating's morphological features notably change with the U-7Mo substrate size. With increasing the substrate size, the grain column size, roughness, and the size and areal fraction of meso-/macroscopic defects of the ZrN coating increase, and hence the coating's packing density decreases. As displayed in Figure 41, the density and area fraction of meso-/macroscopic defects observed over the ZrN coating surface increased with increasing the U-7Mo substrate size. The quantitative values of the defects were obtained by measuring them in the corresponding coating's SEM BSE top-view images using the ImageJ image analysis software.

The change of all the coatings's morphological features can be explicated as a consequence of evolution of the ZrN coating structure in the process of the coating growth. As already mentioned, the ZrN coatings in this chapter are theoretically predicted to be Zone T structure, which was experimentally identified as shown in Figure 40 and Figure 42. In addition, as explained in section 3.2.1, the formation possibility of these defects is expected to rise with increasing the deposition time and hence coating thickness.

#### 4.1.3. Crystallographic characteristics

To investigate crystallographic features of as-deposited ZrN coatings on U-7Mo powders with different sizes, the as-deposited powders of 45–90  $\mu\text{m}$  size were divided into 4 size groups of 45–53, 53–63, 63–75, and 75–90  $\mu\text{m}$  by sufficiently sieving the 45–90  $\mu\text{m}$ -sized powders for at least five minutes. Subsequently, each the size group were measured by a conventional XRD. Since conventional XRD normally has an analysis depth (i.e., penetration depth) normally in the range of 1 to 10  $\mu\text{m}$ , that is, XRD can measure the entire ZrN coatings in the coating-thickness direction. However, it should be noted that XRD inherently provides only the nanometer-scale structure information of samples.

As shown in Figure 43, all the ZrN XRD peaks were somewhat shifted to the smaller or larger  $2\theta$  angle as the substrate size increased. According to Bragg's law, a peak position is directly associated with the lattice constant (lattice parameter, crystal spacing, or d-spacing) of the corresponding crystallographic plane. Once the crystal spacing of a crystal plane become narrow or wide by its expansion or compaction, the  $2\theta$  angle position of the corresponding peak become shifted to a smaller or larger  $2\theta$  angle position than the standard position. Figure 44 presents that obtained lattice-constant of the ZrN coating reduces with increasing the substrate size. From the peak position change with the substrate size, it can be deduced that a compressive-to-tensile residual stress transition of the coating occurs.

As well as the  $2\theta$  angle position, the peak width of the ZrN coating also changed with the substrate size. As the substrate size increased, the width of all the ZrN peaks reduced, which is referred to as “peak sharpening”. The peak sharpening implies a rise in the crystallinity (degree of structural order) of corresponding crystal plane.

According to Halder-Wagner method (Eq. (11)), peak width of XRD profile is governed only by grain size and microstrain [101, 102, 132]. The Halder-Wagner method is a reliable method if the grain size of samples is below 100 nm. The grain sizes and microstrains of the ZrN coatings calculated by utilizing Halder-Wagner method are displayed in Figure 45. The grain size of the coating increases as the U-7Mo substrate size increases. Generally, in the environment activating surface diffusion, grain growth is thermodynamically driven to decrease the free surface energy (called grain boundary free energy) of the coating system until the grain size increases enough to make the grain boundaries stationary. Actually, the ZrN coatings in this study exhibited that their average grain size is in proportion to their coating thickness, which is consistent with an earlier Volmer-Weber island growth model called cone-growth model and an experimental result by Aryal [144]. Aryal experimentally demonstrated that the grain size of Mo magnetron sputtered coatings continuously increased with increasing the coating thickness, irrespective of power source types of used deposition machines (RF and DC) [144]. Besides, with increasing the U-7Mo substrate size, the coating’s microstrain increased (Figure 45).

## 4.2. Impacting factors for coating microstructure

As an impact factor determining the microstructure of sputtered coatings, there are coating thickness [115, 133, 144–150], deposition rate [145, 147, 148, 151, 152], material, shape, and surface roughness of substrate [151–156], deposition temperature [147, 153, 157, 158], background gas [144, 159], and substrate movement during deposition. These factors competitively influence the microstructure of sputtered coatings. In this research, the ZrN coating was various in the thickness and deposition rate depending on the U-7Mo substrate size. Thus, it can be guessed that the observed various microstructures of the ZrN coatings a consequence of their various coating thicknesses and deposition rates depending on the substrate size (0.55 to 1.17  $\mu\text{m}$  for the coating thickness and 1.30 to 2.78 nm/min for the deposition rate).

Many reports have experimentally revealed that the thickness of sputtered coatings is meaningfully influential on their structural characteristics [115, 133, 144–150]. Huang et al. [126] investigated ZrN coatings with various thicknesses of 0.16–0.99  $\mu\text{m}$  deposited by an ion plating machine on Si substrates. As the coating thickness increased, some microstructural changes of the ZrN coating were observed; an increase in lattice constant, the surface roughness, and grain size, and a reduction in the packing density and residual compressive stress. When comparing our results with the results of Aryal and Huang et al., the microstructural-evolution trends our results are in excellent agreement with the corresponding reference results. However, a disagreement of the coating's lattice constant evolution trend between our result and the corresponding reference were found.

The other impact factor for the microstructure of the ZrN coating, deposition rate, can also affect the microstructure of sputtered coatings. It has been experimentally demonstrated that sputtered coatings show an increase in the roughness, grain size, and crystallinity with increasing the deposition rate [162, 163]. Kashyout [162] evaluated the influence of deposition rate on the microstructure of Mo coating deposited by a magnetron sputtering machine. As the deposition rate of the Mo coating increased, its grain size notably increased. Chen et al. [163] investigated the effect of deposition rate on the microstructure of Ti sputtered coatings deposited on Si substrates. As the deposition rate increase from 3 to 87.6 nm/min, the roughness, crystallinity, and grain size slightly increased. Likewise, the microstructural-change trends as a function of the two impact factors (coating thickness and deposition rate) are generally consistent with our results.

### 4.3. Effect of structure on the diffusion barrier capability of ZrN coating

As already noted, ideal diffusion barrier coatings require a uniform in the thickness and microstructure [71]. According to Eq. (11) of ' $x = \sqrt{Dt}$ ' (where  $x$ , and  $t$  are the thickness, and lifetime of a diffusion barrier coating, respectively, and  $D$  is the diffusivity of a passing material through the coating.), the lifetime ( $t$ ) of a diffusion barrier coating is linear to the coating thickness ( $x$ ). For the ZrN coating in this chapter, the coating of 45  $\mu\text{m}$ -sized U-7Mo powders with a thickness of one half of the coating of 90  $\mu\text{m}$ -sized U-7Mo powders theoretically exhibits the functional failure two times faster when assuming that the diffusivity ( $D$ ) is constant. Conversely speaking, only near the thin ZrN coating on small U-7Mo powders, an IL between U-7Mo powder and an Al matrix can be formed unexpectedly early.

Additionally, the diffusivity ( $D$ ), which is the other determinant factor for the lifetime of a diffusion barrier coating ( $t$ ), is determined by the coating microstructure. To achieve a low  $D$  for the high diffusion-barrier-capability of diffusion barrier coating, they need a dense structure without any macroscopic defects accelerating the diffusion of solid materials in the coating. The ZrN coating in this research exhibited that all the coatings excluding the coating of 45  $\mu\text{m}$ -sized U-7Mo powders possessed macroscopic defects (e.g, crater, pinhole, and columnar boundary) over the coating. These defects, working as a high diffusivity path for solid atoms, considerably degrades the diffusion barrier performance of the coating. Moreover, the defects can cause to newly generate a high-diffusivity path (that is, the coating crack) for solid materials by acting as a crack tip and/or reducing the coating's compacting density and hence fracture resistance.

Therefore, to improve the reliability and effectiveness of the ZrN coating in a U-7Mo/Al system, improvement of the coating's structural uniformity and a dense ZrN coating layer without macroscopic defects are required. It is predicted that the structural uniformity of the coating can be increased by using a more narrow size-range of U-7Mo substrate powders. In addition, a dense ZrN coating layer that does not include macroscopic defects can be obtained by further optimizing the deposition parameters and/or limiting the coating thickness less than the "critical thickness" in which the defects begin to be observed.

#### 4.4. Established semi-analytical model describing ZrN coating thickness as a function of U-7Mo substrate size

On the basis of an existing experimental-based model for sputtering yield's angular distribution [163–165], a semi-analytical model representing the thickness of the as-deposited ZrN coating layers as a function of the U-7Mo substrate size has been newly established by pondering the geometry and working principle of the used deposition machine and the friction phenomenon of the U-7Mo substrates inside the rotary drum equipped in the deposition machine.

Figure 37, Figure 38, and Figure 39 shows that the as-deposited ZrN coatings exhibited a uniform thickness over a U-7Mo powder, however, the coating thickness was different depending on the substrate size. The used U-7Mo powders in the 45–90  $\mu\text{m}$  size range showed various size ranges: 53–63, 63–75, and 75–90  $\mu\text{m}$  of  $\sim 30$  wt.%, respectively, and 45–53  $\mu\text{m}$  of  $\sim 7.5$  wt.%. By sieving the 45–90  $\mu\text{m}$  sized U-7Mo powders of 100 g, the powder size distribution was gained. Excluding the size, their other characteristics of the U-7Mo substrate powders such as surface roughness, morphology, and chemical composition were the same. However, all the U-7Mo powders showed the same shape (i.e., nearly-perfect spherical shape) and surface morphology (i.e., a mixed surface of smooth, pitted, and wrinkled surfaces). Moreover, the XRD phase analysis result of Figure 43 shows that all the U-7Mo powders also possess the same composition:  $\gamma$ -U(Mo) containing a small quantity of other phases such as  $\text{UO}_2$  and UC.

At first, during the coating deposition, the position and movement of the substrate powders inside the rotary drum equipped in the used coating machine (Figure 16) were confirmed. The powders are predicted to roll down in the rotary drum because rolling down tend to occur rather than sliding down. Therefore, the sliding movement of the U-7Mo powders in the rotary drum can be negligible for simplification. Accordingly, a U-7Mo powder in the rotary drum can be theoretically assumed to roll down consistently at the fixed location where the rolling friction ( $F_r$ ) is equal to the gravitational force ( $mg \cdot \sin\alpha$ ) (Figure 46), which can be expressed as follows:

$$mg \sin \alpha = F_r \quad (16)$$

$$\text{with} \quad F_r = \frac{b}{r} N = \frac{b}{r} mg \cos \alpha$$

where  $m$  is the mass of a U-7Mo powder,  $g$  is the gravitational acceleration (i.e.,  $9.8 \text{ m/s}^2$ ),  $\alpha$  is the angle in-between the target and powder,  $F_r$  is the induced rolling-friction,  $N$  is the normal force at the location where the powder rolls down,  $b$  is the coefficient of rolling friction, and  $r$  is the radius of U-7Mo

powder. It was assumed that the rolling powder in the force equilibrium state. Eq. (16) can be converted into a simplified equation as follows:

$$\cot \alpha = \frac{D}{2b} \quad (17)$$

where D corresponds to the diameter of a U-7Mo powder in  $\mu\text{m}$ . Due to the observed nearly-spherical shape of the U-7Mo powders and the negligible thickness of the ZrN coatings compared to the substrate size, the diameter of the coatings can be assumed to be the same with the powder size. Additionally, the b determined by the surface conditions of the powder and the drum was presumed to be the same for the coated and non-coated U-7Mo powders because it was experimentally confirmed that the 45–90  $\mu\text{m}$  sized U-7Mo powders of 50 g rolled down at an almost same position whether the powders were coated or not. Moreover, it was also empirically confirmed that the U-7Mo powders of 50 g were rolled down at an almost fixed position irrespective of the drum speed in the range of 4–8 revolutions per minute.

Besides, when pondering the geometrical configuration of the coating machine utilized in this research (Figure 46), the emission angle of coating vapors,  $\theta$ , can be represented as a function of  $\alpha$  angle by utilizing the following trigonometric formulas:

$$d = \frac{R \cdot \sin \alpha}{\sin(\pi - \theta)} = \frac{R \cdot \sin \alpha}{\sin \theta} \quad (18)$$

$$d^2 = h^2 + R^2 - 2Rh \cdot \cos \alpha \quad (19)$$

where h is the distance from the target to drum center of the used coating machine.

The following equation can be achieved by substituting Eq. (18) into Eq. (19),:

$$\theta = \arcsin \left( \sqrt{\frac{R^2 \cdot \sin^2 \alpha}{h^2 + R^2 - 2Rh \cdot \cos \alpha}} \right) \quad (20)$$

By utilizing the known geometries of the coating machine ( $h = 9$  cm,  $R = 17$  cm),  $\theta$  angle can be expressed as:

$$\theta = \arcsin\left(\sqrt{\frac{676 \cdot \sin^2\alpha}{757 - 486 \cdot \cos\alpha}}\right) \quad (21)$$

It has been revealed by experiments [163–165] and a simulation [174] that sputtered atom's angular distribution,  $Y(\theta)$ , expressing the sputtering yield of target material as a function of angular emission angle, is fitted well to a cosine power law expressed as:

$$Y(\theta) = Y_{max} \cdot \cos^n\theta \quad (22)$$

where  $Y_{max}$  is the greatest sputtering yield at  $\theta = 0^\circ$  in no dimension,  $\theta$  is the emission angle of coating materials ejected from the target,  $n$  is the dimensionless fitting parameter relying on the deposition parameters such as power source, applied power, type and flux of working gas, substrate movement, and target-to-substrate distance. It was revealed that the empirical results of silicon and germanium sputtered coatings was well fitted to Eq. (22) [163, 164]. Based on the deposition process of sputtered systems, the coating thickness's angular distribution is predicted to follow a cosine power law in the case that the deposition condition is same in regard with all the  $\theta$  angles. Indeed, it was experimentally revealed that the coating-thickness's angular distribution of aluminum, copper, lead, and platinum magnetron sputtered coatings followed a cosine power function [175].

Excluding the emission angle at the location of the U-7Mo powders, it can be supposed that there are several deposition parameters influencing their resulting coating thickness of coatings based on the deposition mechanism and geometry (Figure 46) of the used coating machine as follows: 1) the pile-up behavior of U-7Mo powders inside the drum; 2) the spatial deposition environment of chamber; 3) the incident angle of sputtered target-atom flux; and 4) the dynamics of the U-7Mo powders. In the respect with all the  $\theta$  angle, these factors are the same or very similar, hence they can be negligible.

Accordingly, because the powder rolling position in the drum can be assumed to depend solely on the powder size, the thickness distribution  $T(\theta)$  of the as-deposited ZrN coating in this chapter is governed moajorly by the sputtering yield (Eq. (22)), and thus follows a cosine function as describes below:

$$T(\theta) = T_{max} \cdot \cos^n \theta \tag{23}$$

where  $T_{max}$  is the greatest thickness of the ZrN coating at  $\theta = 0^\circ$ . As shown in Figure 48, the measured values (marked as points in the graph) of the ZrN coating fits well to Eq.(23). From the fitting, n and  $T_{max}$  were obtained as 4.86 and 1.63  $\mu\text{m}$ , respectively.

Finally, by substituting Eqs. (17) and (21) into Eq. (23), the the ZrN coating's thickness can be expressed as a function of the U-7Mo diameter,  $D$ , as follows:

$$T(\theta) = T_{max} \cdot \cos^n \left( \arcsin \left( \sqrt{\frac{676 \cdot \sin^2 \alpha}{757 - 486 \cdot \cos \alpha}} \right) \right) \tag{24}$$

with  $\alpha = \arctan \left( \frac{21.0}{D} \right)$

where n is 4.86 and  $T_{max}$  is 1.63  $\mu\text{m}$ .



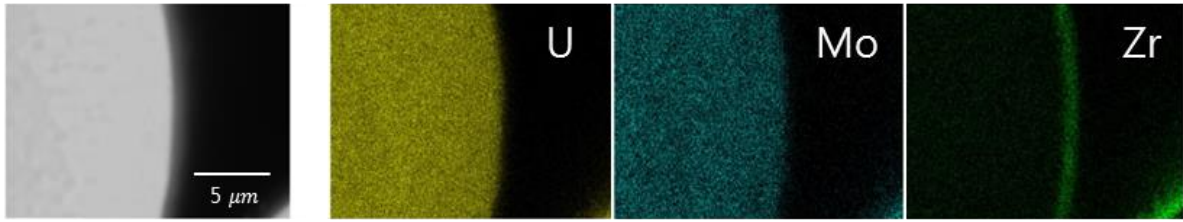


**Figure 37.** Cross-sectional EDS mapping images of a ZrN-coated U-7Mo powder [63].

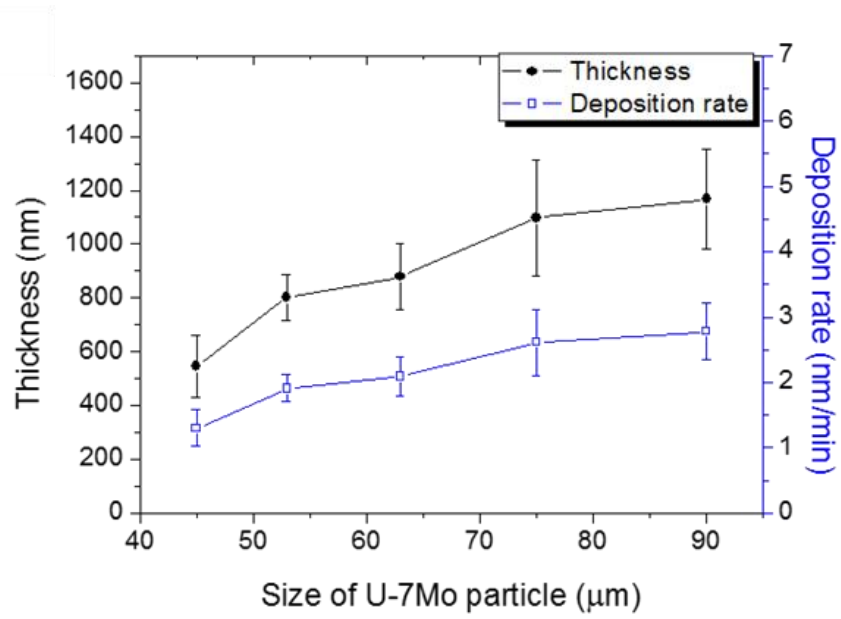


**Figure 38.** Measured thickness and deposition rate of ZrN coatings on U-7Mo powders of various sizes [63].

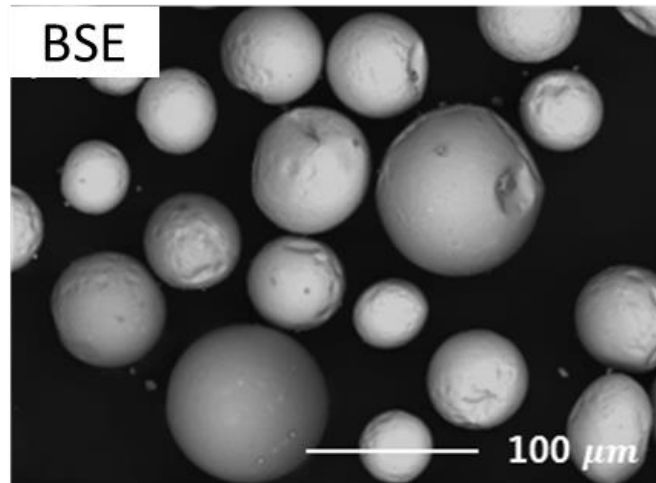


**Figure 39. SEM BSE top-view image of 45–90  $\mu\text{m}$ -sized U-7Mo powders coated with a ZrN single layer [63].**

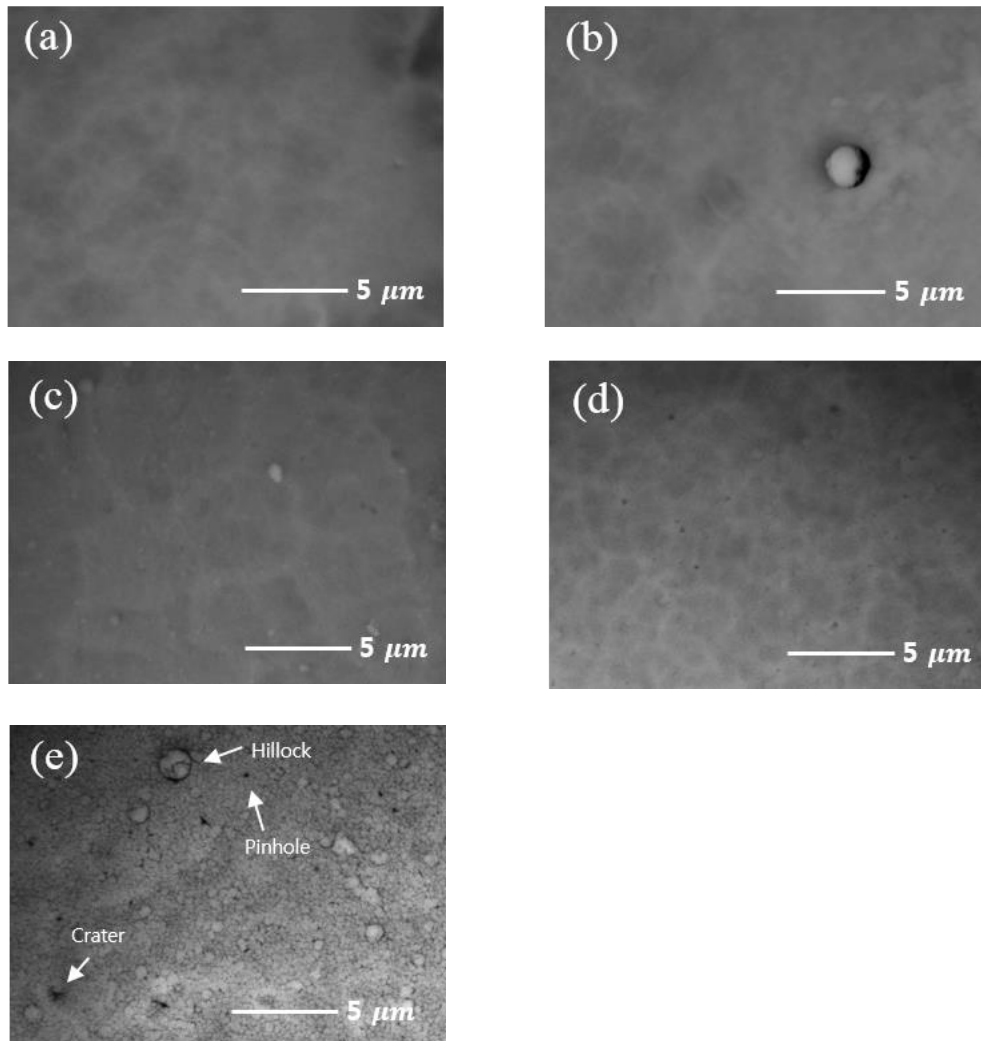


**Figure 40.** SEM BSE top-view micrographs of ZrN coatings on different sizes of U-7Mo powders: (a) 0.55  $\mu\text{m}$ -thick coating for 45  $\mu\text{m}$ -diameter U-7Mo powders, (b) 0.80  $\mu\text{m}$  for 53  $\mu\text{m}$ , (c) 0.88  $\mu\text{m}$  for 63  $\mu\text{m}$ , (d) 1.10  $\mu\text{m}$  for 75  $\mu\text{m}$  and (e) 1.17  $\mu\text{m}$  for 90  $\mu\text{m}$  [63].

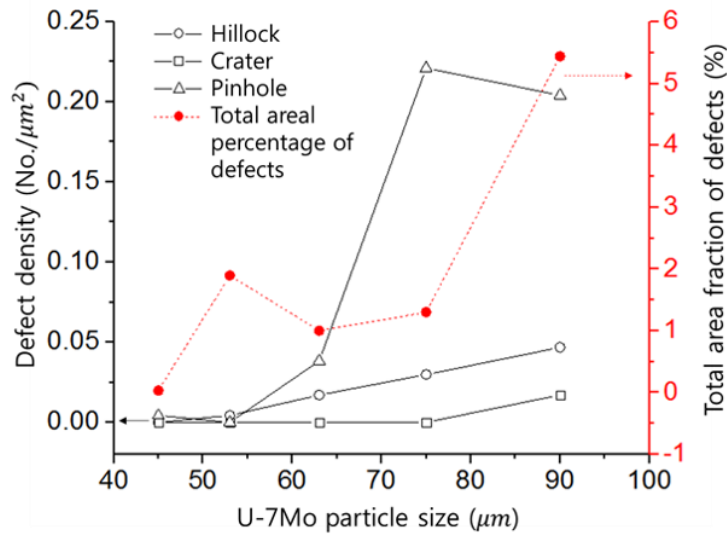
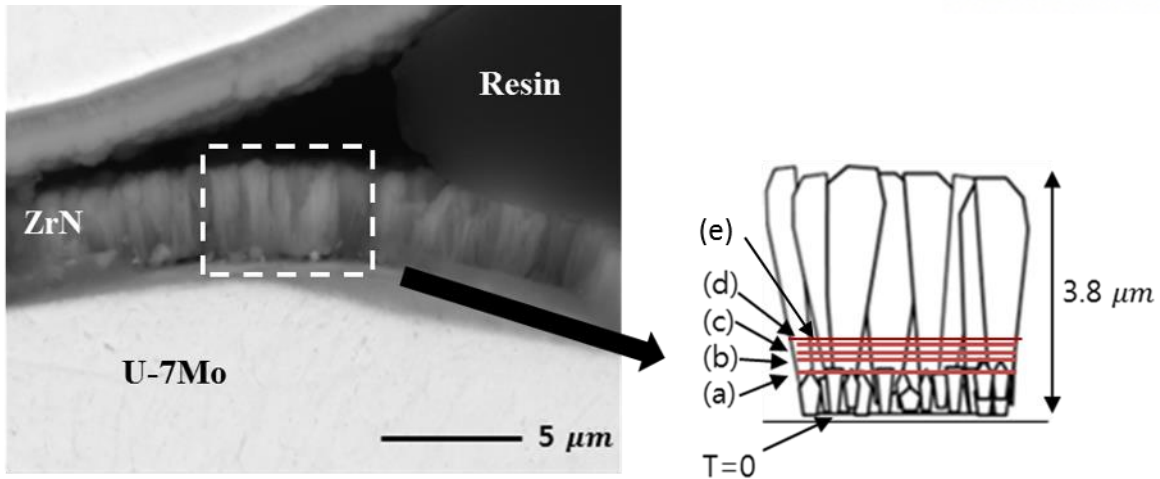


Figure 41. Measured density and total area fraction of surface defects formed in ZrN coatings [63].



**Figure 42. SEM BSE fractured cross-sectional micrograph (left) and schematic cross-section (right) of a 3.8 μm-thick ZrN coating layer on a U-7Mo powder [62]. In the schematic, (a) 0.55 μm-thick coating for 45 μm-diameter U-7Mo powders, (b) 0.80 μm for 53 μm, (c) 0.88 μm for 63 μm, (d) 1.10 μm for 75 μm and (e) 1.17 μm for 90 μm are displayed [63].**

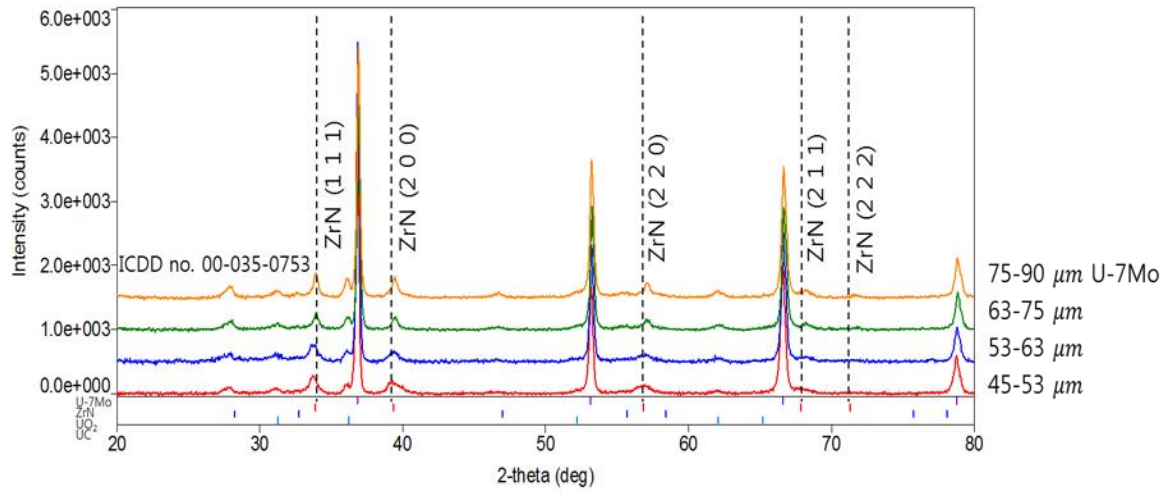


Figure 43. XRD patterns of ZrN-coated U-7Mo powders as a function of the powder size [63].

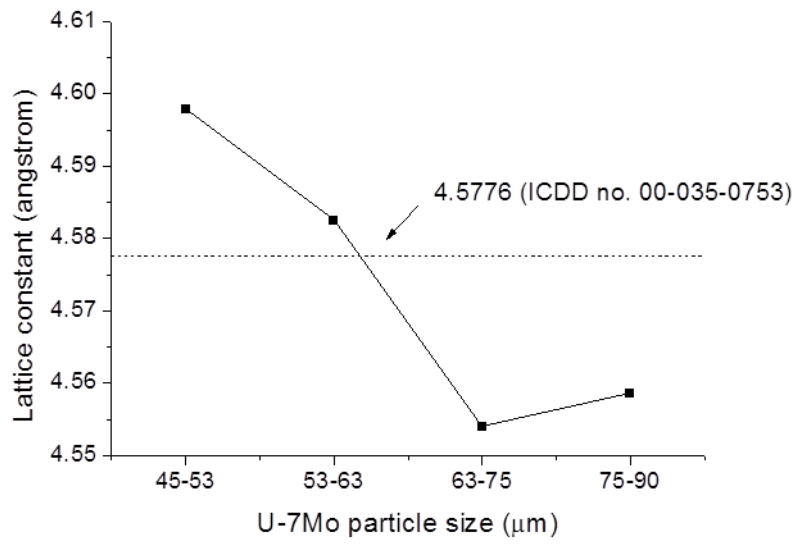


Figure 44. Lattice constants of ZrN coatings on U-7Mo powders of various sizes [63].



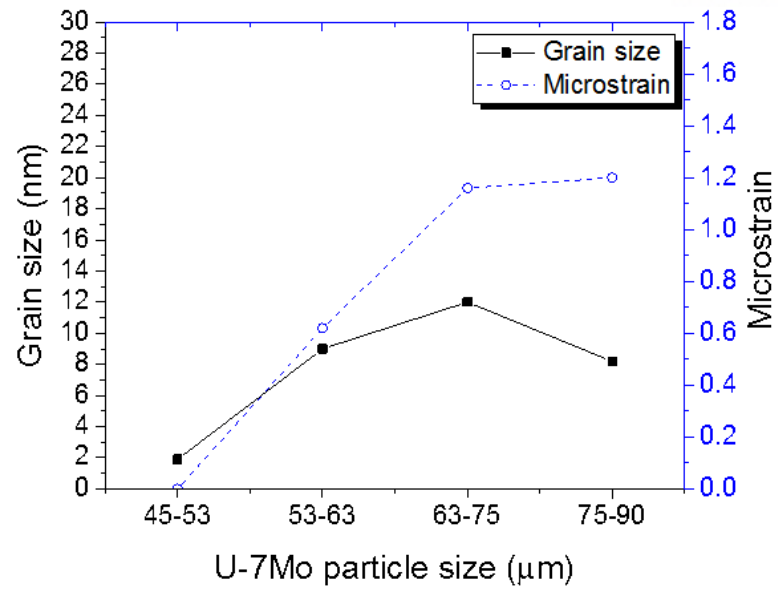


Figure 45. Grain size and microstrain of ZrN coatings on U-7Mo powders of different sizes [63].

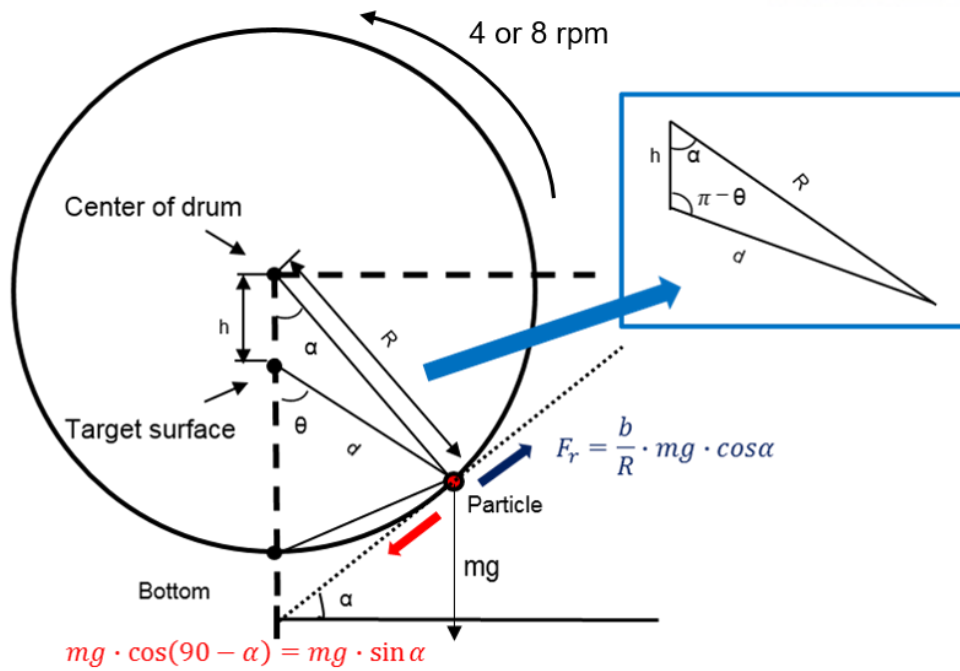
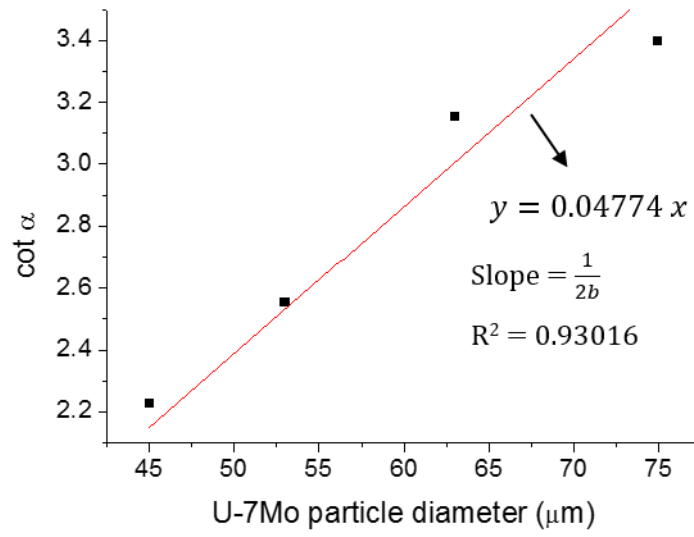
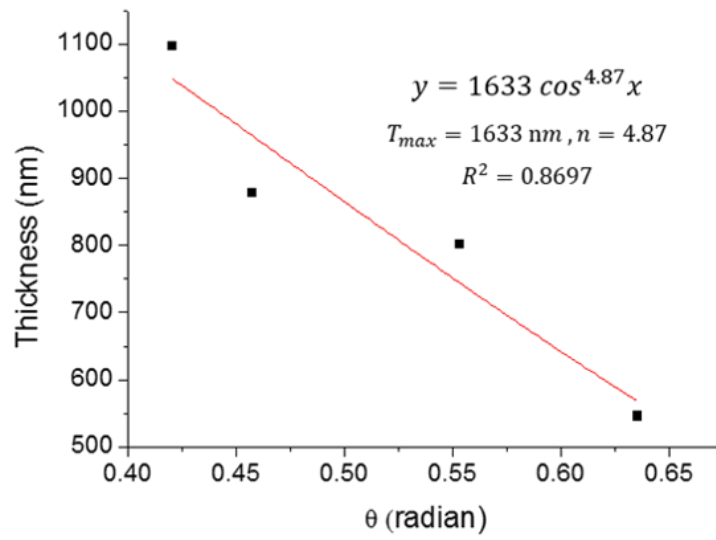


Figure 46. Forces acting on a U-7Mo powder which are displayed in a schematic diagram of the used coating machine [63].



**Figure 47. Linear plot of measured  $\cot\alpha$  values (represented by individual data points) versus U-7Mo powder diameter [63].**



**Figure 48. Fitting the measured values for ZrN coatings to the cosine power law of Eq. (23) [63].**

## **Chapter 5. Effect of coating thickness, U-Mo substrate size, and annealing temperature on structural failure of ZrN coating on U-Mo powders at a high post-deposition processing temperature**

In this chapter, I focused on experimentally and numerically estimating the structural integrity of a ZrN coating layer at high processing temperature of multiple heat-treatments of dispersion fuel plate manufacturing. It should be noted that a portion of ZrN coating must experience the loss of structural integrity by other stress sources such as compacting pressure (~60 ton for full-sized dispersion fuel plates) and rolling pressure, but no data is available to quantify the fracture of the ZrN coating by compaction and rolling processes. Thus, this chapter is designed to investigate the possibility of mechanical failure of ZrN coating during the heating processes as a preliminary study based on the coating microstructure. For two different size of U-7Mo fuel powders, a ZrN single layer with different thicknesses was deposited for the parametric studies to check the relationship between the microstructure and structural integrity of the ZrN coatings at a certain temperature.

### **5.1. Characterization of as-deposited ZrN coatings with different thicknesses**

#### **5.1.1. Morphology**

The as-fabricated ZrN coating on the U-7Mo powders was examined by SEM and EDS. As displayed in Figure 49, it was reviewed that almost the powders were surrounded by a ZrN single coating layer with a uniform thickness. In addition, it was found that the U-7Mo powders used in this study were almost spherical which implies that their size is identical to their diameter. However, each the ZrN coating exhibited a variety of coating thicknesses depending on U-7Mo substrate size as noted in chapter 4. This is because that large U-7Mo powders rotates in a static position with a low emission angle (an ejected angle of sputtered atoms or molecules from target surface) during the deposition process, as demonstrated in the previous chapter (Chapter 4). With reducing the emission angle, the coating thickness increased according to a certain cosine power equation.

Table 8 shows the measured thicknesses of the ZrN coatings on each 45 and 90  $\mu\text{m}$ -diameter U-7Mo powders. The coating thickness was measured by using SEM SE cross-sectional images of  $10^4$  magnification. In order to measure the true coating thickness in the equator of each 45 and 90  $\mu\text{m}$  diameter U-7Mo powder, the U-7Mo powders of 45–53  $\mu\text{m}$  and 75–90  $\mu\text{m}$  diameter range respectively were separated by sieving, and then polished until the greatest powder diameter (45  $\mu\text{m}$  and 90  $\mu\text{m}$  for the 45–53  $\mu\text{m}$  and 75–90  $\mu\text{m}$  powders, respectively) was observed in the polished plane. The coating

thicknesses of each the 45 and 90  $\mu\text{m}$ -diameter powders were randomly measured 10 times at one spot per coated powder in SEM SE cross-sectional micrographs. For the ZrN coated spherical U-Mo powders, compared to SE cross-sectional images, BSE reflective cross-sectional images is prone to display over-estimated coating thicknesses because the deeper penetration depth (up to several micrometers) of BSE with greater energy allows to exhibit even the side of samples. As a result, ZrN coating layers is likely to appear thicker in BSE micrographs than in SE micrographs. The measured thicknesses of the as-fabricated ZrN coatings showed that the coating thickness increases almost linearly with the deposition time, which is a consequence of the constant deposition rate in the PVD deposition machine. Besides, coated U-7Mo powders with same deposition time showed that large (90  $\mu\text{m}$ ) sized powder has a thicker coating than small (45  $\mu\text{m}$ ) sized powder.

The low magnification BSE image of Figure 50 clearly re-confirms that U-7Mo substrate size affected the coating layer thickness of ZrN coatings. The brightness variation of the coated powders indicates different coating thicknesses depending on the powder size since the brightness of BSE images is proportional to the average atomic number within several micrometer-depth from the sample surface. Since ZrN is composed of much lighter atoms than U-7Mo, powders with thicker coating layers look relatively dark in BSE images. Hence, the larger size powders had generally thicker coatings, which validates the relationship between the substrate size and ZrN coating thickness measured in cross-sectional images (see Table 8).

As seen in Figure 51, the ZrN coating has a V-formed columnar structure. Generally, coating morphology is determined by the deposition parameters [177–183]. According to Thornton's structure zone model [177], the ZrN coating in this study is believed to have Zone T-structure with dense fibrous columnar structure, as mentioned before. The coating's stop-view micrograph as exhibited in Figure 52 showed Zone T structure of V-shaped columnar structure. In addition, the coating's porosity size and column boundary gap width increased as the coating grew.

From Figure 51, two different structures depending on deposited coating thickness were observed in the ZrN coating layer; a much denser structure for the inner layer up to  $\sim 0.5 \mu\text{m}$  thickness from the substrate surface and a relatively porous structure for the outer layer above  $\sim 0.5 \mu\text{m}$  thickness due to presence of the column boundary gaps (i.e., porosities between the coating columns). This dense-to-porous structural transition can be identified also in Figure 52. The column boundary gap started to be detected by SEM from ZrN coatings with a certain thickness between 0.49 and 0.73  $\mu\text{m}$ . The porosities formed above the thickness are suggested to be a result of "shadowing effect", which is defined as being the vapor flux by target atoms within the growing coating layer being geometrically blocked by adjacent pre-formed columnar structures. This shadowing effect causes the decrease of the coating density by the porosity formation between columns, and it is accelerated in proportion to the coating column width and height [177]. Additionally, the spherical morphology of the U-7Mo substrate

induces a variation in the angle of incidence for the vapor flux, and it produces a microcolumnar-structured coating with a more complex and porous (less dense) morphology [170, 171, 173].

Moreover, a defect growth induced by stress evolution in coatings lowers the physical density of the coatings. As shown in Figure 52, the density of defects such as hillocks and crater over ZrN coatings changed with the coating thickness. The hillock is a result of mass transportation for the relaxation of compressive stress over a coarse columnar-shaped coating [174, 175]. Since the compressive stress increases with coating growth, the formation of the hillocks becomes favorable in the coating layer thicker than a certain coating thickness [184]. This hillock is likely to be detached from the coating owing to its poorly-adhesion and leads to the formation of the craters.

By examinations, the critical thickness was found to be 0.5  $\mu\text{m}$  in this study. I examined the ZrN coatings deposited on 45–90  $\mu\text{m}$  for 4 h, the coatings on large U-7Mo powders exhibited surface partial cracks. From observation of 30 powders in top view SEM images, the coatings on the U-7Mo powders larger than 53  $\mu\text{m}$  size showed surface cracks over the coatings. Since the coating thickness was proportional to the U-7Mo size, I considered the coating thickness of 53  $\mu\text{m}$ -sized U-7Mo powder as the critical thickness. In order to measure the thicknesses of 53  $\mu\text{m}$ -sized U-7Mo powder, 45–53  $\mu\text{m}$ -sized powders assorted by sieving method were mounted, and then polished until the equator of 53  $\mu\text{m}$ -sized powders was shown in the polished plane (the observation plane). After that, the coating thickness of 53  $\mu\text{m}$ -sized powders was randomly measured 10 times at one point per powder. The measured average value of the critical thickness was 0.52  $\mu\text{m}$ , approximately 0.5  $\mu\text{m}$ .

### 5.1.2. Grain size and microstrain

by using Halder-Wagner method (Eq. (11) and Figure 54), the grain size and isotropic microstrain of the ZrN coating can be calculated. The obtained grain sizes of ZrN coating layer deposited for 2, 4, 7, 10, 13, 15, and 25 h were 4.9, 3.4, 3.6, 3.8, 3.9, 4.0, and 6.4 nm respectively, while all the ZrN coatings with various coating thicknesses showed zero microstrain. The grain sizes and microstrains showed no noticeable changes after annealing at 300–700°C. The annealing-induced grain size change in this study is in good agreement with the experimental results by Chiech et al. in Ref. [187].

## 5.2. Experimental examination of heat-treated ZrN coating

### 5.2.1. Effect of coating thickness and substrate size (coating diameter) on ZrN coating failure

According to classical theory for thin spherical shells of which diameter-to-thickness ratio is greater than 20, a tensile hoop stress induced over the thin shells is linear to the diameter-to-thickness ratio. It has been experimentally proved that the thickness of a thin coating as well as its morphology works as important factor for its mechanical properties [79, 80, 82, 180]. In this study, ZrN-coated U-7Mo powders with different coating thicknesses and diameters were heated at 500°C for 2 h. The heating results for the coating's mechanical failure behavior are summarized in Table 9 for the powders with minimum (45  $\mu\text{m}$ ) and maximum (90  $\mu\text{m}$ ) sizes. Per sample, surficial and cross-sectional SEM BSE micrographs 20 times were analyzed. Through-thickness cracking of a ZrN coating layer was observed in the ZrN coatings of which thickness was larger than 0.74 and 1.04  $\mu\text{m}$  for 45 and 90  $\mu\text{m}$ -sized powders, respectively. The surface cracks were observed in surficial images, but not in cross-sectional images, which means that the surface crack length is less than the resolution (normally, 5 nm) of the utilized conventional SEM.

The pattern of formed cracks is dependent on produced stress state. Figure 55 shows that vertical cracks generated between columns produced the crack channelling of a polygonal pattern through their interconnection. This polygonal crack pattern is believed as a result of the isotropic tensile stress of the biaxial or in-plane direction of the coating layer which surpasses the fracture strength. Once the isotropy of the in-plane or biaxial stress increases, the crack pattern generally changes from linear to polygonal shape [189].

Moreover, the generated coating cracks can propagate into the interface between the substrate and coating layer, and/or even the substrate inside. As presented in Figure 56, the partial ZrN coating above 1.7  $\mu\text{m}$  showed de-bonding (known as "cohesive failure") accompanying cracks. The weak adhesion system between the metal (i.e., U-Mo) and nitride (i.e., ZrN) is highly likely to be separated even by a low shear stress [190]. The shear stress in proportion to the CTE mismatch between the substrate and coating is concentrated at their interface, which is similar to the value at the free edge [183, 184]. The free edge stress at the cracks acts as an extra stress at the interface, and thus plays an key role to determine the interfacial integrity of the coating. Once the stress at the free edge of cracks exceeds coating toughness and interface toughness, interfacial edge cracking and even delamination of the coating can be accompanied by coating cracking [185, 186]. However, the investigation of the interfacial edge cracking associated with free edge stress is beyond the scope of this study due to the lack of data.



### 5.2.2. Effect of heat-treatment temperature on ZrN coating failure

The tensile thermal stress in the ZrN coating can cause microcracking over the coating, and this microcracking behavior is extremely reliant on the heat-treatment temperature. In order to assess the heating effect on cracking behavior of the ZrN coating, I utilized the U-7Mo powders containing a ZrN coating layer deposited for 7 h, of which thickness was considered as a critical thickness for coating failure at a normal processing temperature of 500°C. The annealing results of the ZrN coating at different temperatures from 300° to 700°C are shown in Figure 57 and summarized in Table 10. Per sample, the creation of through-thickness crack was confirmed by 20 measurements in the cross-sectional and surficial SEM BSE micrographs. The through-thickness coating cracking began from 500°C for ZrN-coated U-7Mo powders with 45 and 90 μm sizes.

Figure 58 shows that the measured linear crack density (number of cracks per unit length) of the heated ZrN coatings is slightly reliant on the heat-treatment temperature. When considering the error bars corresponding to each sample standard deviation, the linear crack density seems constant after crack formation was initiated at a specific strain in 500°C environment. The crack density was determined by the intercept method. In this method, the number of cracks intercepting a drawn straight line is divided by the total length of the line. In this study, a 30 μm-long line was randomly drawn in SEM BSE top-view images of 5000 magnification and then cracks intercepting the line were counted. The measurement was repeated 20 times with different line orientations on several fields of the SEM BSE top-view images.

### 5.3. Stress analysis of heat-treated ZrN coating by finite element simulation

#### 5.3.1. Stress development

When a stress exerted over a coating layer exceeds a critical mechanical strength, the coating fails by fracture. In the case of the ZrN coating in this study, the fracture strength is equivalent to UTS due to the brittleness of ZrN. The stresses formed in the coating layer can be decomposed down into intrinsic stress and thermal stress [186–188]. The intrinsic stress is induced by the formation of crystallographic flaws during deposition process, while the thermal stress results from the differences in CTEs between the U-7Mo substrate and the ZrN coating.

The intrinsic stress of as-deposited coatings is dependent on their homogeneous temperature corresponding to their deposition temperature. As noted before, the intrinsic stress is normally in compressive owing to generated lattice defects caused by bombardment of high-energy Ar positive ions. However, at a high deposition temperature, the lattice defects are easily recovered through their atomic diffusion to sinks such as free surface, dislocation, and grain boundary [197]. As a result, the lattice defects can be removed without detectable changes in morphology, grain size, and texture. Furthermore, nanocrystalline coatings including the ZrN coating in this research have a large number of grain boundaries, working as a sink. Hence, the grain boundary relaxation may be promoted. Additionally, it was demonstrated that the onset temperature for the defect recovery of non-reactively sputtered TiN coatings decreased with compressive biaxial stress which can be a driving force for the defect recovery [198]. At a great compressive stress ( $< 5$  GPa), the TiN coating was recovered even below 250°C. Thus, it is supposed that the deposition temperature of 250°C in this study induced the annihilation of the generated defects over growing ZrN coatings with high compressive stress during deposition, which leads to the zero microstrain of the coating layer. From XRD analysis result in this study, I could prove the zero microstrain of all as-deposited ZrN coatings.

Therefore, I regarded the thermal stress resulting from CTE mismatch as the major source of the coating cracking during annealing. Once the annealing temperature is higher than the deposition temperature (250°C), a high magnitude of tensile thermal stress will be induced in the ZrN coating owing to its lesser CTE than that of U-7Mo. Consequently, the ZrN coating' elongation occurs in the hoop direction, and can eventually be cracked, because brittle compound coatings cannot withstand the relatively larger dimension change of the metallic substrate beneath the coating [199].

### 5.3.2. Failure criterion

During the annealing process, the induced thermal stresses within the ZrN coating on spherical U-7Mo powder can be decomposed into the hoop stress component in tension, and radial stress in compression. I employed the maximum normal stress theory [200] in which the failure criterion is that a brittle material fails if the maximum principal stress exceeds the fracture strength, irrespective of other existing components of the stress tensor. Considering the dimensions of the substrate and the coating layer, the thin-wall theory was employed to understand which stress component is the maximum principal stress in the ZrN-coated powder system. In the coating layer, the hoop stress of a thin spherical coating is about 30 times greater than the radial stress according to the thin-wall theory for spherical geometry. Thus, I focused on the hoop stress as the maximum principal stress.

In addition, the failure (i.e., through-thickness cracking) criterion for a ZrN coating should be defined differently depending on the coating thickness owing to its significant microstructural change at the critical thickness. In other words, the coating's failure criterion depends on the creation of surface coating cracks during heat-treatment, and this is discussed in the following subsections.

#### 5.3.2.1. Failure of coating thinner than critical thickness

The fracture criterion for the ZrN coatings below the critical thickness 0.5  $\mu\text{m}$  is regarded as the UTS because no crack tips were observed due to their dense structure. Unfortunately, there is no accessible experimental value of the UTS for ZrN coating considering nano-scale grains. Instead, the UTS for ZrN coating was obtained by using the UTS-Vickers hardness relationship, in which the ratio of Vickers hardness to UTS is typically 3.45 [193–195].

It is well known that mechanical properties including Vickers hardness are largely dependent on microstructure. Thus, the UTS for the ZrN coating from Vickers hardness was calculated with additional consideration of the coating microstructure in order to improve the reliability of the calculated UTS. Some microstructural factors influencing the UTS should be considered. Specifically, grain size considerably influences hardness and thus UTS. The hardness increases with reducing the grain size based on classical Hall-Petch equation expressed as:

$$H = H_0 + kd^{-1/2} \quad (25)$$

where  $H$  is the hardness,  $H_0$  is the hardness in the absence of grain boundary,  $k$  is the strengthening coefficient (a positive constant specific to each material), and  $d$  is the grain size. However, in the case of nanocrystalline materials consisting of fine grain (<10 nm in size), it has been empirically

demonstrated that hardness decreases with a decrease in grain size, which is named “inverse Hall-Petch effect” [196–200]. That is, the slope of the Hal-Petch plot ( $k$ ) is a negative constant. Qi et al. [209] revealed that ZrN nanostructured coating deposited by magnetron sputtering showed the transistion from classical Hall-Petch effect to inverse Hall-Petch effect at the critical grain size of 16 nm. In the case of small grain sizes from 11 to 16 nm for the ZrN coating, the slope of Hall-Petch plot ( $k$ ) was  $-41.1 \text{ GPa nm}^{1/2}$ . In this study, each the nano-hardness considering the measured grain sizes of ZrN coatings thinner than the critical thickness was gained by extrapolating the Hall-Petch plot by Qi et al.. Then, UTS values represented in Table 12 were obtained by using the ratio of UTS to Vickers hardness that is 3.45. For ZrN coatings thinner than the critical thickness  $0.5 \mu\text{m}$  without surface cracks, their mechanical integrity was assessed by comparing the calculated hoop stress with the UTS.

### 5.3.2.2. Failure of coating thicker than critical thickness

The partial surface cracks were observed at the surface of mean  $0.5 \mu\text{m}$ -thick (defined as critical thickness) ZrN coating heated at  $500^\circ\text{C}$ , as already mentioned. Despite of the isotropic hoop stress, the heat-treatment test results of the  $0.5 \mu\text{m}$ -thick ZrN coating layer showed a surface cracking at the outer coating layer. This indicates that the porous coating outer layer has a lower fracture strength than the dense inner layer. The generated surface crack is likely to work as a crack tip where a local stress is concentrated. Therefore, an alternative failure criterion considering the crack tip is necessary to be defined instead of UTS.

In this context, the tip of the surface cracks along the columnar grain boundaries, which were observed in the microstructure analysis on the coating surface, is believed to be an initiation site where cracks start to propagate, and eventually lead to coating failure by thickness-through cracking. For the fracture of brittle material with a fine crack by mode I fracture, the crack is known to induce the stress concentration at the crack tip. For the case of the ZrN coating with surface cracks, the local stress concentration is induced at the crack tip region. According to Griffith's fracture criterion [210] for a brittle material, fracture strength that is the stress when a crack starts to propagate from a existing crack tip and then fracturing occurs can be expressed as the following equation:

$$\alpha_f = 2E\gamma/\pi c \quad (26)$$

where  $\alpha_f$  is the fracture strength,  $E$  is the Young's modulus,  $\gamma$  is the surface energy, and  $c$  is the crack tip length. In this study, the length of the crack tip is was calculated under the assumption that the ZrN coating layer possesses linearly-long crack tips parallel with the coating growth direction. Subsequently, the length of crack tip was obtained as follows:

For  $t_{\text{ZrN}} > 0.5 \mu\text{m}$ ,

$$c = t_{\text{ZrN}} - t_0 \quad (27)$$

where  $t_{\text{ZrN}}$  is the thickness of ZrN coating layer, and  $t_0$  is the maximum coating layer thickness in the absence of crack formation, that is equivalent to the critical thickness (i.e.,  $0.5 \mu\text{m}$ ) determined based on the examination results.

### 5.3.3. Modelling of finite element simulations

To assess the fracturing (i.e., through-thickness cracking) behavior of the ZrN coating, the hoop stress calculated by using ABAQUS program was compared to the different fracture criterion that are determined by the presence of the crack within the ZrN coating layer. The material properties utilized for the ABAQUS simulation are listed in Table 11. It was assumed that the U-7Mo substrate and the ZrN coating are in thermal equilibrium during heat-treatment. The predefined field for temperature for all finite elements was set to the heat-treatment temperatures. Multi-step ABAQUS simulation was conducted to calculate: (1) the residual stress formed by the misfit of linear CTE between the substrate (U-7Mo) and coating layer (ZrN) during the deposition at  $250^\circ\text{C}$ , and (2) the hoop stress that is induced by the misfit during annealing. Since thermal expansion of the U-7Mo and the ZrN is the main source of the stress generation, coupled thermo-mechanical analysis was applied for the simulation.

Two steps were implemented by ABAQUS as follows:

- 1) In the first analysis step for the residual stress, ZrN coated U-7Mo powder is cooled from the deposition temperature of  $250^\circ\text{C}$  to room temperature ( $25^\circ\text{C}$ ). In this cooling step, residual stress is induced in the ZrN coating layer in a compressive manner.
- 2) In the next step for the thermal stress during annealing, the ZrN coated U-7Mo powder is heated up to a given heat-treatment temperature ( $300\text{--}700^\circ\text{C}$ ). The FE simulations for both U-7Mo and ZrN are performed under the assumption that they are in thermal steady-state.

The ZrN coating deposited on the U-7Mo powder was regarded as a spherical shell for the consideration of large-strain deformation. In order to prevent shear and membrane locking, a continuum shell element, which consists of eight nodes with reduced integration (S8RT), was utilized. Its mechanical behaviors are determined by classical theory for thin shells, and shear flexible theory for thick shells. The constituent law for U-7Mo/ZrN models in the rectangular coordinate is expressed by thermo-elastic deformation model, which is given as:

$$\begin{aligned}
 \varepsilon_x &= \frac{1}{E}[\sigma_x - \nu(\sigma_y + \sigma_z)] + \alpha T \\
 \varepsilon_y &= \frac{1}{E}[\sigma_y - \nu(\sigma_x + \sigma_z)] + \alpha T \\
 \varepsilon_z &= \frac{1}{E}[\sigma_z - \nu(\sigma_x + \sigma_y)] + \alpha T \\
 \gamma_{yz} &= \frac{1}{G}\tau_{yz}, \quad \gamma_{zx} = \frac{1}{G}\tau_{zx}, \quad \gamma_{xy} = \frac{1}{G}\tau_{xy}
 \end{aligned} \tag{28}$$

where the subscript on the right side of symbols is the notation for the coordinate, E and  $\nu$  are Young's modulus and Poisson's ratio,  $\alpha$  is the diagonal component of the Cauchy stress tensor matrix,  $\gamma$  is the shear component of the stress tensor matrix,  $\sigma$  is the stress, T is the temperature, G is the shear modulus,  $\varepsilon$  is the shear strain, and  $\tau$  is the thermal expansion coefficient.

## 5.4. Finite element simulation results

Two different simulations to calculate the thermal stress in the ZrN coating layer were performed: (1) simulations for different coating thicknesses with respect to two different diameters (45 and 90  $\mu\text{m}$ ) of U-7Mo powders at the same heat-treatment temperature, and (2) simulations for different heat-treatment temperatures with the fixed coating layer thickness and diameter. The results are stated in the following subsections.

### 5.4.1. Effect of coating thickness and diameter on the coating failure

For investigating the coating thickness effect on the fracturing behavior of a ZrN coating layer, FE simulations were conducted for different thicknesses of 45 and 90  $\mu\text{m}$ -diameter U-7Mo powders at 500  $^{\circ}\text{C}$  for 2 h. The calculation results for the residual stress, the thermal stress, and employed fracture criterion are summarized in Table 12. In Figure 59, the calculated hoop stresses for the different coating layer thicknesses and substrate sizes (i.e., coating diameters) are shown together with the fracture criterion which is UTS or theoretical fracture strength. According to classical theory for thin spherical shells, the hoop stress induced over the ZrN coating is uniform along the coating thickness, and is in proportion to the radius-to-thickness ratio of the coating. Additionally, the fracture criterion alters from the UTS to the fracture strength if the coating thickness is larger than the critical thickness of 0.5  $\mu\text{m}$ . According to Griffith fracture criterion [210], fracture strength is inversely proportional to the length of crack tip. Hence, in the case of ZrN coatings above the critical thickness, the thicker the coating layer and the larger the U-7Mo powder size are, the easier the crack creation is induced in the coating layer.

By comparing calculated hoop stress with fracture criterion (Table 12), coating failure was evaluated to happen as through-thickness cracking. In the case that the coating thickness was larger than 0.74  $\mu\text{m}$  for the U-7Mo powder with 45 mm diameter and 0.73  $\mu\text{m}$  for the U-7Mo powder with 90  $\mu\text{m}$  diameter, the coating failure is predicted to occur at a heat-treatment temperature of 500 $^{\circ}\text{C}$ . These numerical calculation results for crack creation by FE simulations are almost in line with the experimental examination results (Table 9).

As a diffusion barrier coating of SELENIUM full-sized fuel plates, a 1  $\mu\text{m}$ -thick ZrN coating together with 0.6  $\mu\text{m}$ -thick Si coating have been chosen and studied [37, 40, 56, 57, 67]. When considering the experiment and simulation results of this study, it is suspected that the 1  $\mu\text{m}$  thickness for the ZrN coating is too thick to maintain the structural integrity during the heat treatment processes (commonly at 500 $^{\circ}\text{C}$ ) of dispersion fuel plate manufacturing.

#### 5.4.2. Heat-treatment temperature effect on coating failure

In order to estimate the effect of the heat-treatment temperature on induced thermal stress of the ZrN coatings, FE simulations were performed for ZrN coatings with each fixed thickness on U-7Mo powders of 45 and 90  $\mu\text{m}$  diameters at different heat-treatment temperatures from 300°C to 700°C for 2 h. The calculated hoop stress results were compared to the theoretical fracture strength for the ZrN coating, as shown in Table 13 and Figure 60. Due to the fixed morphology (e.g., the thickness and microstructure of the ZrN coating and U-7Mo size) of samples, the fracture strength of each the coated U-7Mo powders with 45 and 90  $\mu\text{m}$  diameter is the same irrespective of the given heat-treatment temperature.

By comparing the hoop stress with the fracture strength, the coating cracking is theoretically predicted to occur at temperatures higher than 500°C and 400°C for ZrN-coated U-7Mo powders with 45 and 90  $\mu\text{m}$ -diameter, respectively. For most of the samples, the temperature when the calculated hoop stress exceeded the theoretical fracture strength is equivalent to the temperature when the coating fracture by crack propagation was examined in the heat-treatment experiments. This means that the FE simulation has well evaluated the possibility of cracking of the coating layer under the given conditions.

The FE simulation demonstrated that general heat-treatment temperature of 500°C produces forces to generate through-thickness cracks over the ZrN coatings. Figure 60 identifies that low heating heat-treatments below 400°C are required in order to maintain the structural integrity of the ZrN coatings.



**Table 8. Measured thicknesses of ZrN coatings on U-7Mo powders as a function of deposition time and U-7Mo powder size [62].**

Deposition time - (h)	45 $\mu\text{m}$ -sized U-7Mo powder ( $\mu\text{m}$ )	90 $\mu\text{m}$ -sized U-7Mo powder ( $\mu\text{m}$ )
2	$0.25 \pm 0.02$	$0.36 \pm 0.02$
4	$0.49 \pm 0.04$	$0.73 \pm 0.04$
7	$0.74 \pm 0.05$	$1.06 \pm 0.08$
10	$1.05 \pm 0.03$	$1.58 \pm 0.08$
13	$1.39 \pm 0.16$	$1.87 \pm 0.05$
15	$1.72 \pm 0.13$	$2.50 \pm 0.23$
25	$2.53 \pm 0.33$	$3.46 \pm 0.33$

**Table 9. Observed mechanical failure behavior of ZrN coating on U-7Mo powder as a function of coating thickness and powder size (coating diameter) [62].**

U-7Mo powder size	Coating layer thickness	Observed failure type	Measured through-thickness cracking*
( $\mu\text{m}$ )	( $\mu\text{m}$ )		(Y/N)
45	0.25	–	N
	0.49	Surface crack	N
	0.74	Through-thickness crack	Y
	1.05	Through-thickness crack	Y
	1.39	Through-thickness crack	Y
	1.72	Through-thickness crack	Y
	2.53	Through-thickness crack	Y
90	0.36	–	N
	0.73	Surface crack	N
	1.06	Through-thickness crack	Y
	1.58	Through-thickness crack	Y
	1.87	Through-thickness crack	Y
	2.50	Through-thickness crack	Y
	3.46	Through-thickness crack	Y

\* Coating cracking was determined by 20 measurements per sample. If coating cracks in a sample were found in more than 80% of measurements, it is labelled “Y.” Otherwise, it is labelled “N.”

**Table 10. Examined mechanical failure behavior of ZrN coating on U-7Mo powder as a function of annealing temperature and powder size (coating diameter) [62].**

U-7Mo powder size ( $\mu\text{m}$ )	Coating layer thickness ( $\mu\text{m}$ )	Annealing temperature ( $^{\circ}\text{C}$ )	Observed failure type	Measured through-thickness cracking* (Y/N)
45	0.74	300	-	N
		400	Surface crack	N
		500	Through-thickness crack	Y
		600	Through-thickness crack	Y
		700	Through-thickness crack	Y
90	1.06	300	-	N
		400	Surface crack	N
		500	Through-thickness crack	Y
		600	Through-thickness crack	Y
		700	Through-thickness crack	Y

\* Coating cracking was determined by 20 measurements per sample. If coating cracks in a sample were found in more than 80% of measurements, it is labeled “Y.” Otherwise, it is labeled “N.”

**Table 11. Material properties used in the FEA simulation [62].**

<b>Material</b>	<b>UMo [212]</b>	<b>ZrN</b>
<b>Mechanical property</b>		
<b>Young's modulus (GPa)</b>	85	450 [103]
<b>Poisson's ratio</b>	0.34	0.25 [103]
<b>Thermal property</b>		
<b>Linear thermal expansion coefficient (10<sup>-6</sup> m/m-K)</b>	17.3	7.4 [47]
<b>Thermal conductivity (W/m-K)</b>	35.7 <sup>a</sup>	20.5 <sup>b</sup> [96]
<b>Surface property</b>		
<b>Surface energy (J/m<sup>2</sup>)</b>	-	2.95 [213]

<sup>a</sup> At 500°C.

<sup>b</sup> At room temperature.

**Table 12.** Calculated hoop stress by ABAQUS and estimated coating fracture for different ZrN-coating thickness of 45 and 90  $\mu\text{m}$ -sized U-7Mo powders annealed at 500°C [62].

U-7Mo powder size ( $\mu\text{m}$ )	Coating layer thickness ( $\mu\text{m}$ )	Residual stress of as-deposited ZrN coating (GPa)	Calculated hoop stress by ABAQUS during annealing (GPa)	Theoretical fracture strength (Fracture criterion) (GPa)	Theoretical expectation of through-thickness cracking of ZrN coating (Y/N)
45	0.25	-1.35	2.36	4.00	N
	0.49	-1.30	2.25	7.04	N
	0.74	-1.24	2.15	1.88	Y
	1.05	-1.17	2.04	1.24	Y
	1.39	-1.11	1.93	0.97	Y
	1.72	-1.06	1.84	0.83	Y
	2.53	-0.94	1.64	0.65	Y
90	0.36	-1.37	2.39	3.36	N
	0.73	-1.32	2.31	1.91	Y
	1.06	-1.28	2.24	1.23	Y
	1.58	-1.23	2.14	0.87	Y
	1.87	-1.20	2.08	0.79	Y
	2.50	-1.14	1.98	0.65	Y
	3.46	-1.06	1.83	0.53	Y

**Table 13.** Calculated hoop stress by ABAQUS and estimated coating fracture for ZrN coatings on 45 and 90  $\mu\text{m}$ -sized U-7Mo powders annealed at various given temperatures [62].

U-7Mo powder size	Coating layer thickness	Annealing temperature	Residual stress of as-deposited ZrN coating	Calculated hoop stress by ABAQUS during annealing	Theoretical fracture strength (Fructure criterion)	Theoretical expectation of through-thickness cracking of ZrN coating
( $\mu\text{m}$ )	( $\mu\text{m}$ )	( $^{\circ}\text{C}$ )	(GPa)	(GPa)	(GPa)	(Y/N)
45	0.74	300	- 1.24	0.37	1.88	N
		400	- 1.24	1.19		N
		500	- 1.24	2.15		Y
		600	- 1.24	2.69		Y
		700	- 1.24	3.23		Y
90	1.06	300	- 1.32	0.39	1.23	N
		400	- 1.32	1.27		Y
		500	- 1.32	2.28		Y
		600	- 1.32	2.84		Y
		700	- 1.32	3.41		Y

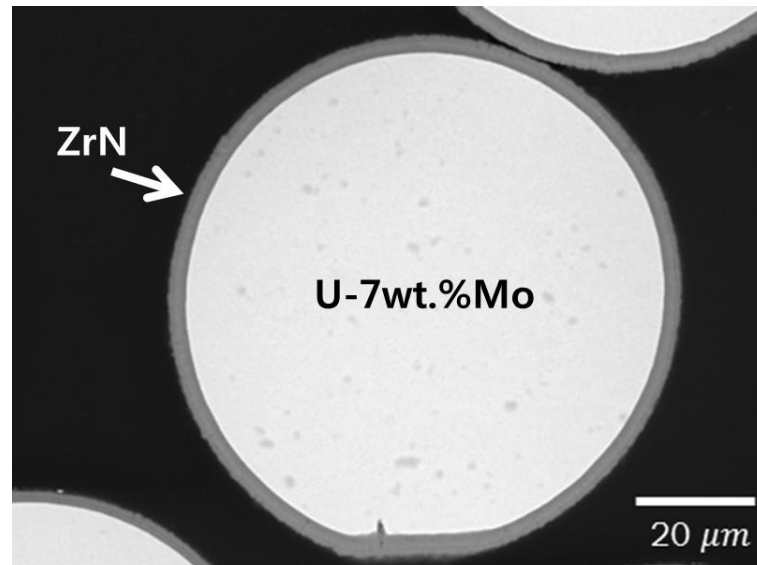


**Figure 49.** SEM BSE cross-sectional micrograph of ZrN coatings on U-7Mo powders [62].

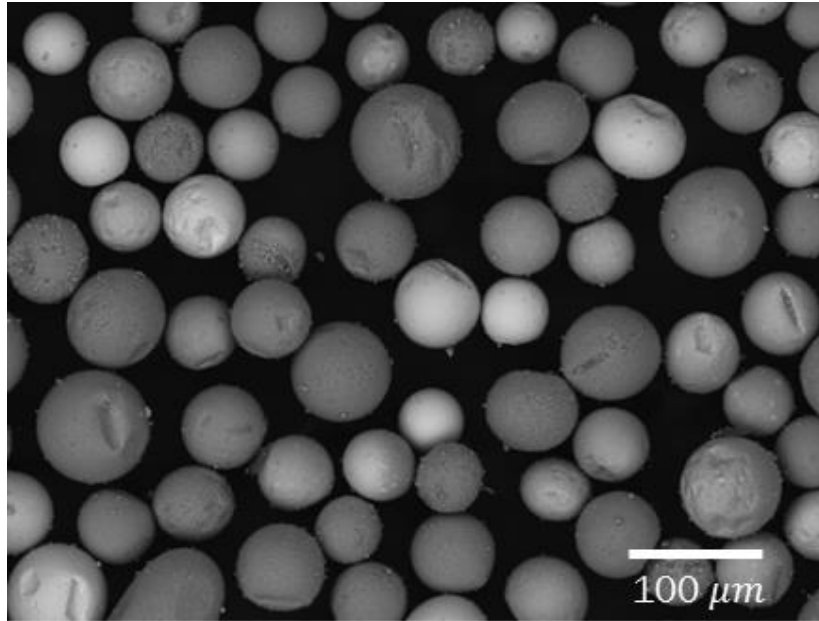


**Figure 50.** SEM BSE top-view image of ZrN-coated U-7Mo fuel powders [62].



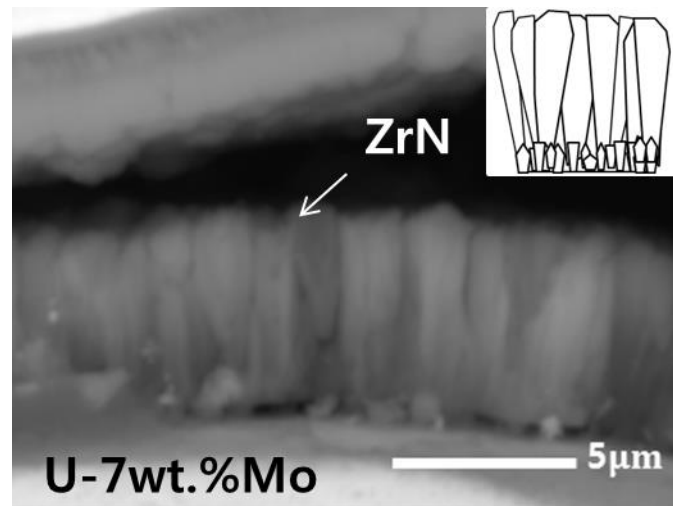


**Figure 51. SEM BSE micrograph and schematic (upper-right image) of fractured cross-section of the ZrN coating deposited on a U-7Mo powder for 25 h [62].**

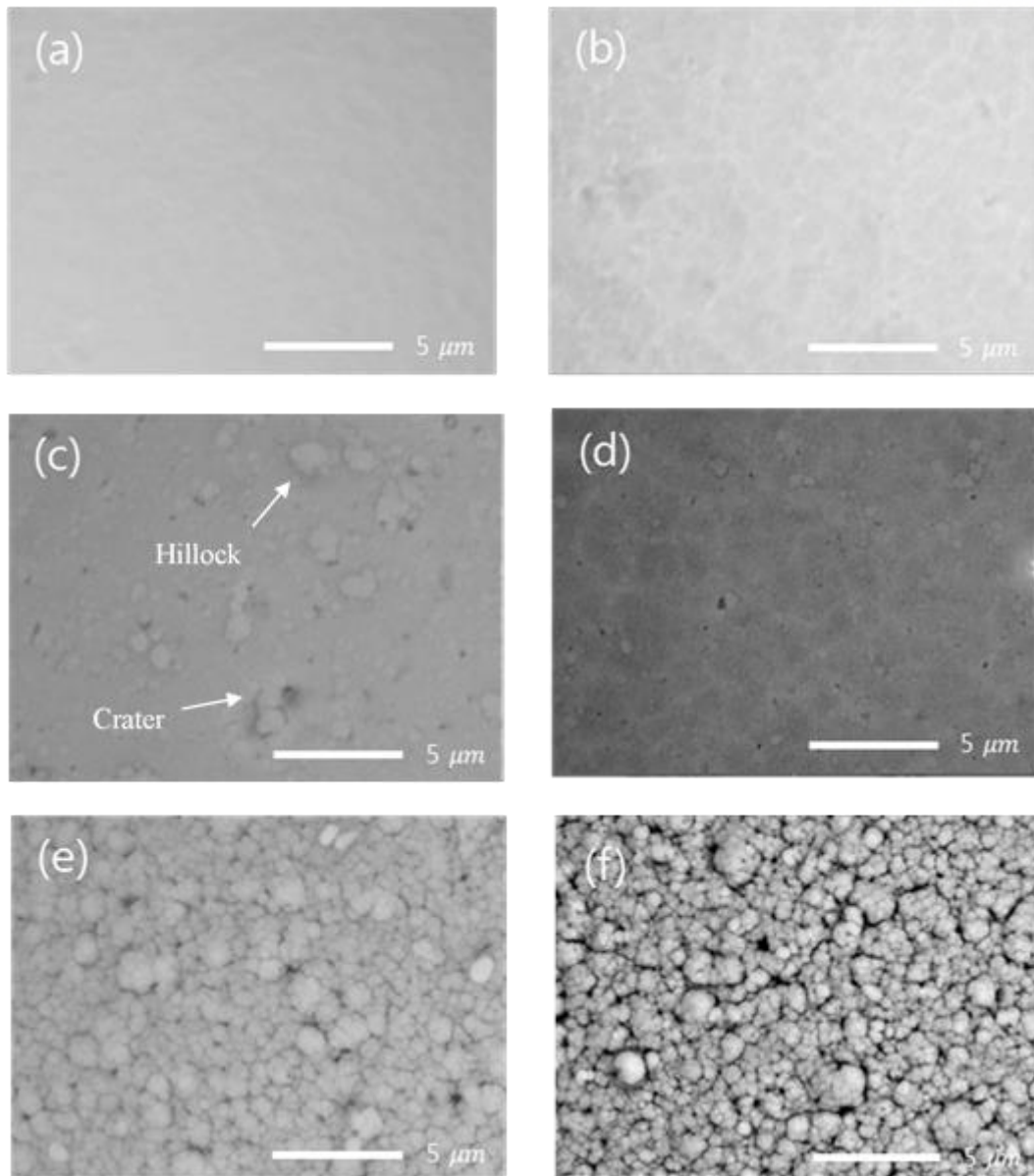


**Figure 52. SEM BSE top-view images of ZrN coatings with deposition times of (a) 2 h, (b) 4 h (0.49 μm-thick ZrN coating on 45 μm-sized powder), (c) 4 h (0.73 μm-thick ZrN coating on 90 μm-sized powder), (d) 7 h, (e) 15 h, and (f) 25 h on a U-7Mo powder [62].**

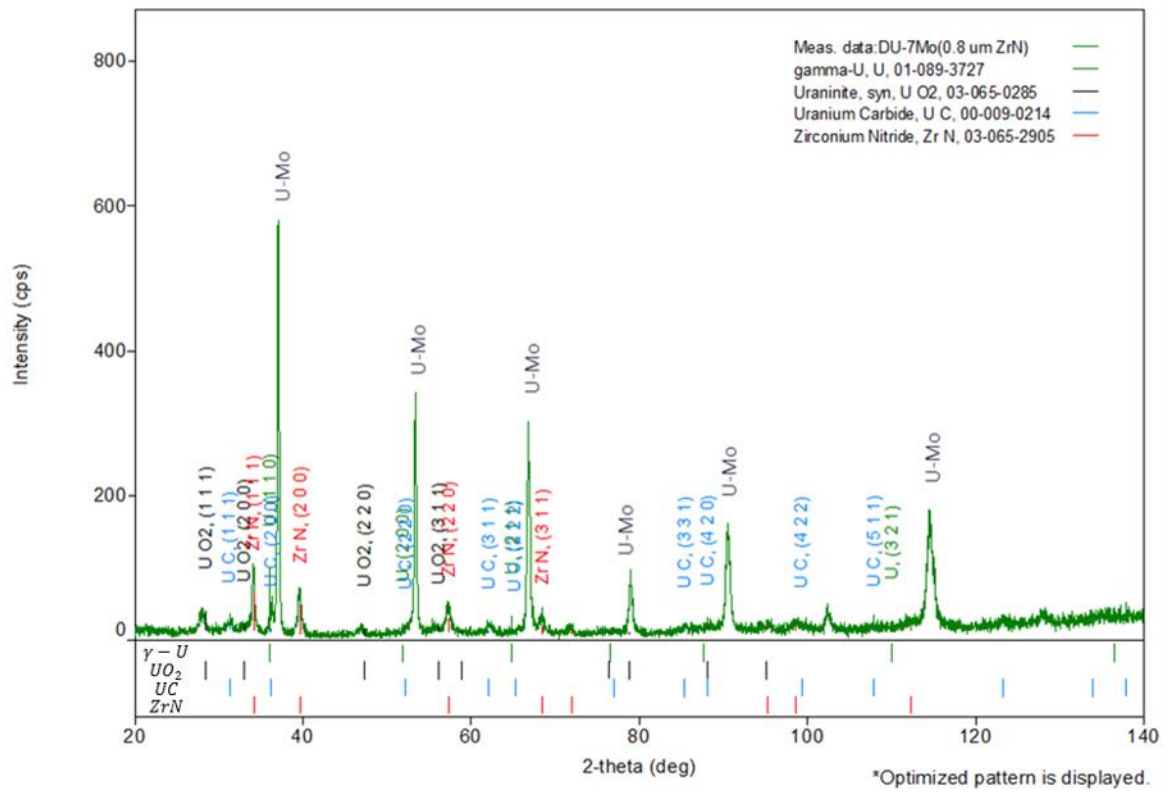
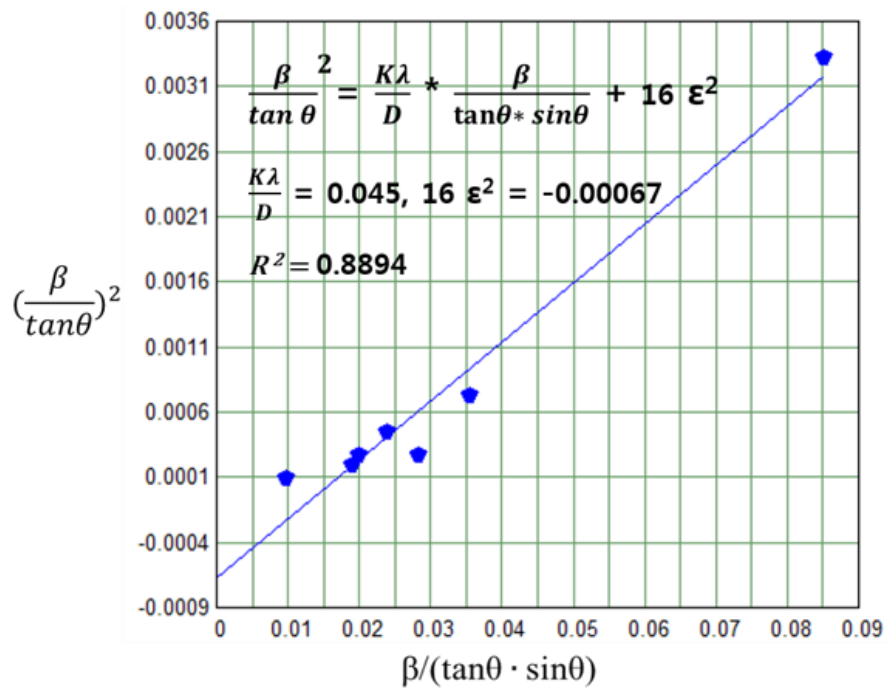
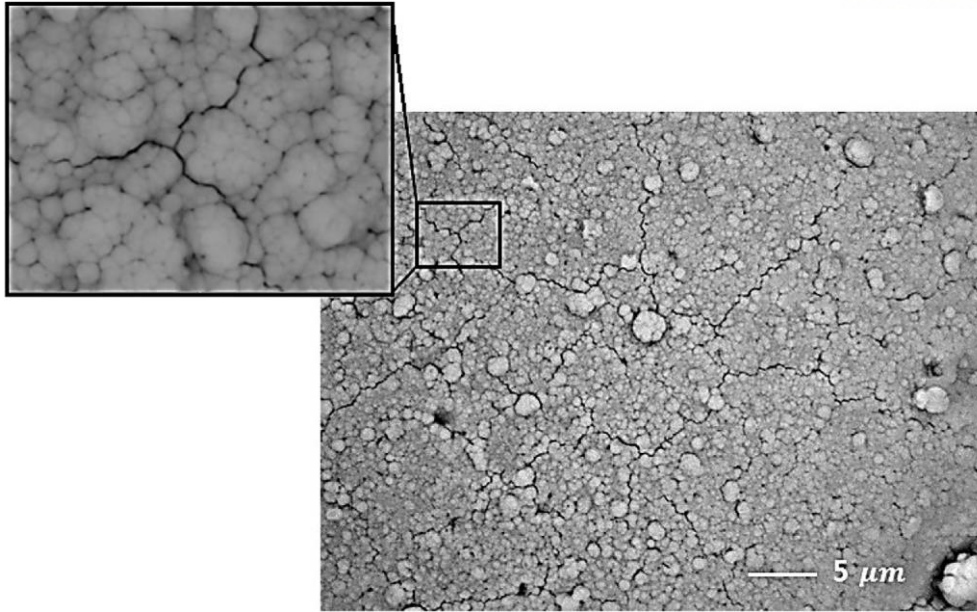


Figure 53. XRD profile of ZrN coatings deposited on 45–90 μm-sized U-7Mo powders for 7 h [62].



**Figure 54.** Halder-Wagner grain size-microstrain plot of ZrN coatings deposited on 45-90  $\mu\text{m}$ -sized U-7Mo powders for 7 h. The slope and the y-intercept of the plot are  $K \lambda / D$  and  $16\epsilon^2$ , respectively [62].



**Figure 55. SEM BSE top-view image of a mean 3.46 μm-thick ZrN coating after annealing at 500°C for 2 h [62].**

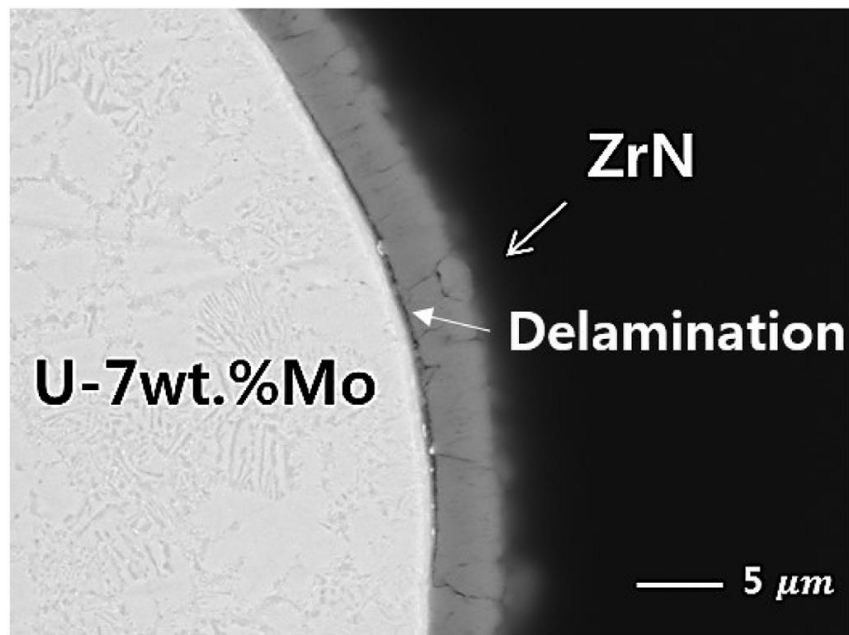


**Figure 56.** Cross-sectional SEM BSE image of a 3.8 μm-thick ZrN coating layer annealed at 500°C for 2 h [62].

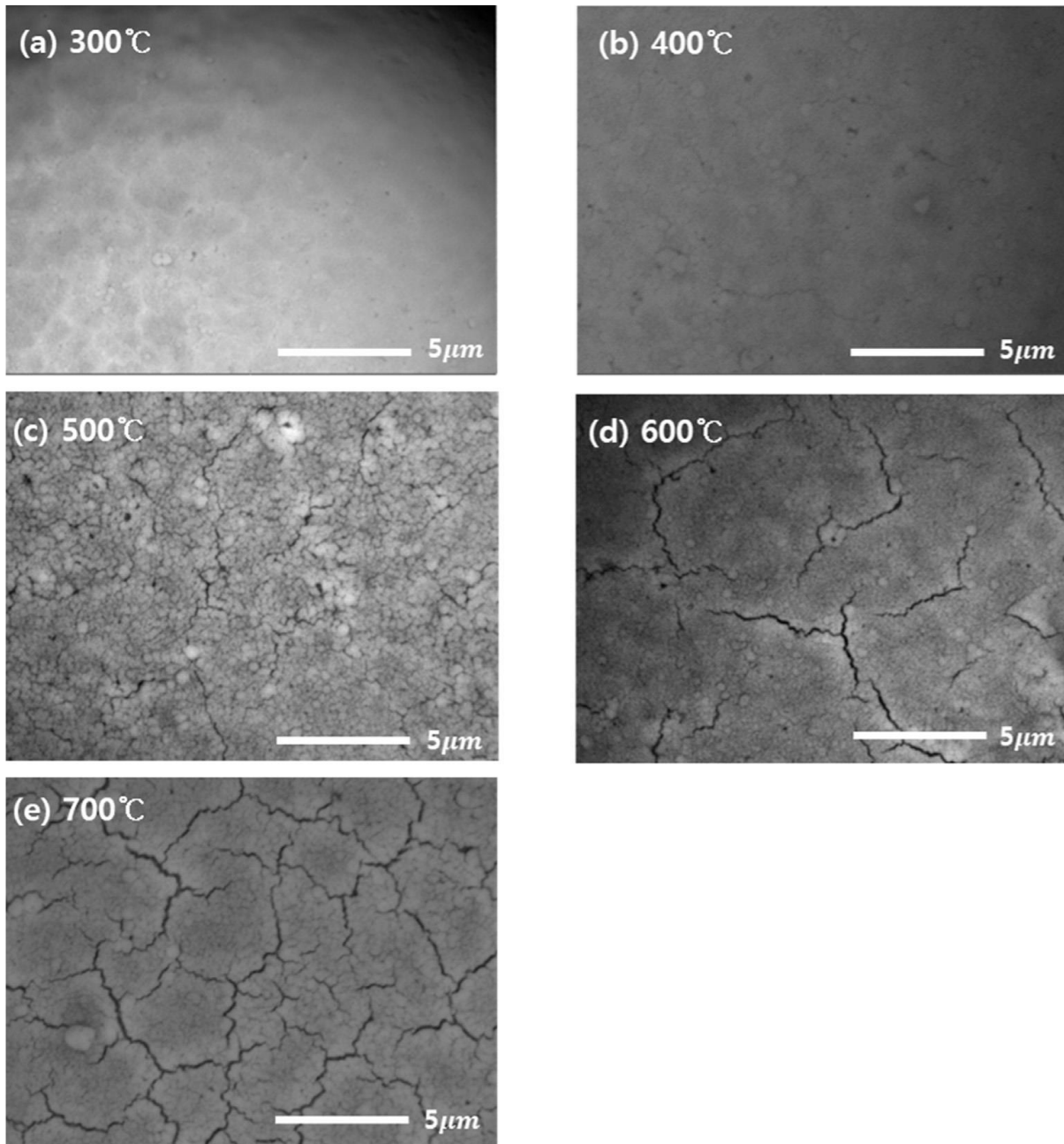


**Figure 57.** Surficial SEM BSE images of average 1.06 μm-thick ZrN coatings annealed at 300°–700°C for 2 h [62].

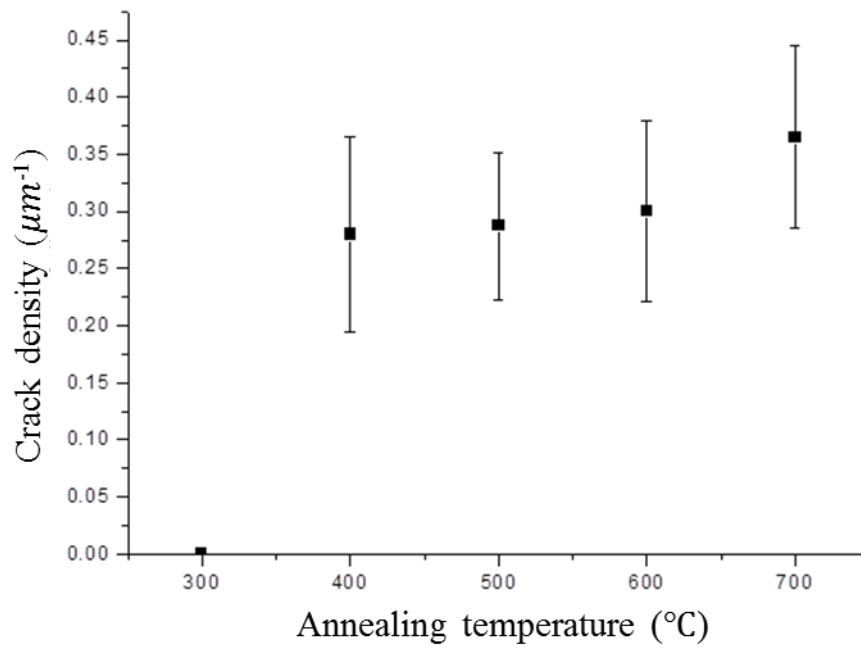


**Figure 58. Crack density of 1.06  $\mu\text{m}$ -thick ZrN coatings various annealing temperatures based on surficial SEM BSE image analysis [62].**



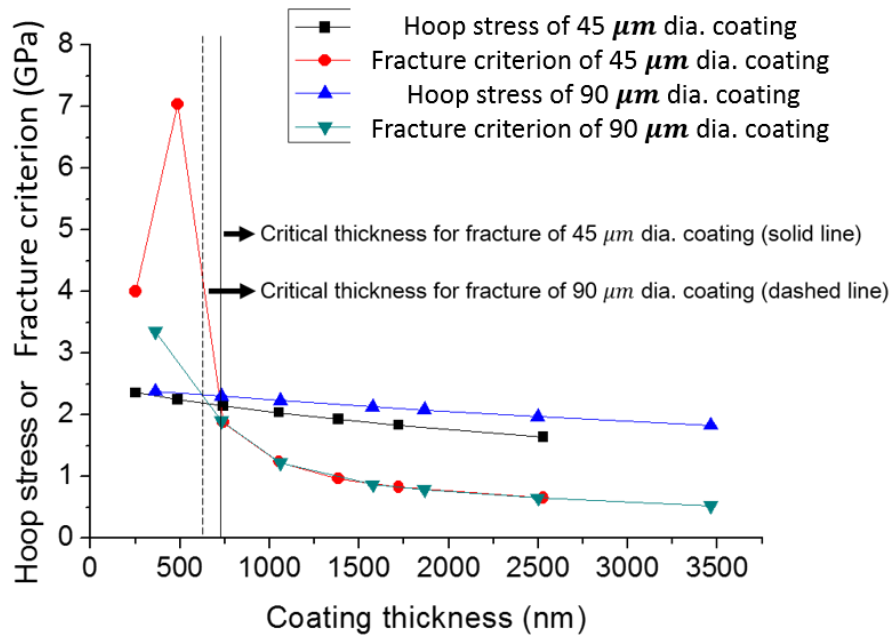


**Figure 59. Comparison of the calculated hoop stress and fracture criterion of ZrN coatings at different coating thicknesses with respect to two U-7Mo powder sizes [62]. The fracture criterion is ultimate tensile strength for coating thicknesses less than 0.5 μm, and fracture strength for coating thicknesses over 0.5 μm.**

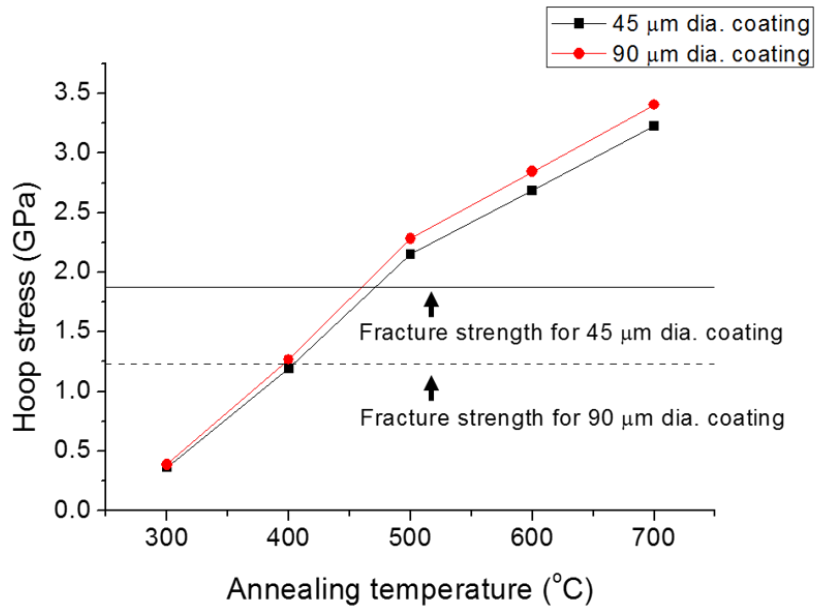


**Figure 60. Comparison of the calculated hoop stress and fracture strength (fracture criterion) of ZrN coatings at different annealing temperatures with respect to two U-7Mo powder sizes (i.e., two coating forms) [62].**

## Chapter 6. Conclusions

### 6.1. Summary

U-7wt.%Mo (U-7Mo) alloy was selected as a next fissionable fuel material for high-performance (or high neutron-flux) research and test reactors (RRs). U-7Mo/Al dispersion fuel plate is a general RR fuel design. To achieve the high neutron flux, U-7Mo/Al dispersion fuel plates should be irradiated up to high burnup. U-7Mo/Al dispersion fuel plates showed a good irradiation performance at low burnup, and however the fuel plates irradiated up to high burnup presented the structural failure mainly by the fission-induced interdiffusion interaction layer (IL) between the U-Mo powder and Al matrix. Accordingly, as a solution to suppress the IL formation, a ZrN diffusion barrier coating layer has been actively applied to U-7Mo/Al dispersion fuel plates. In the case of ZrN coating adopted U-7Mo/Al dispersion fuel plates irradiated up to a high burnup, acceptable thin ILs were generated next to the intact ZrN coatings, while a undesirably huge IL were formed near the damaged ZrN coatings. The local coating damage, which is suspected to be produced during the dispersion-fuel-plate manufacturing, is a critical problem significantly degrading the diffusion barrier capability. However, there are no studies scientifically investigating the ZrN coating damage. Accordingly, in this research, based on the parametric studies of ZrN coating microstructure, the fracturing behavior of the coatings on U-7Mo powders was experimentally and numerically investigated as a function of the coating thickness, U-7Mo substrate size, and annealing temperature.

This research can be summarized as follows.:

First, ZrN coatings with various thicknesses in the range of mean 0.1–2.6  $\mu\text{m}$  was deposited on 45–90  $\mu\text{m}$ -sized U-7Mo substrate powders and then characterized in terms of the microstructure and residual stress by SEM, EDS, and XRD. Result showed that the ZrN coatings appearing a V-shaped columnar structure changed in the microstructures and residual stress state with the coating thickness: The the different residual stress states along the coating thickness led to the interlaminar delamination, which limited the maximum thickness to 2.2  $\mu\text{m}$ . As the coating thickness increased from 0.1 to 2.6  $\mu\text{m}$ , the grain size of the coating increased from 2 to 6 nm, which implied that the grain boundary density of the coating decreased. Based on the atom-scale structure and surface morphology analyzed by XRD and SEM, it could be supposed that the coating's packing density increased up to 0.2  $\mu\text{m}$  thickness, and afterwards reduced abruptly due to the formation of macroscopic defects (i.e., hillock, crater, pinhole, and column gap) and increase in the interplanar spacing. The ZrN coating showed a structural transformation from dense-to-porous structure at a critical thickness between 0.2 and 0.5  $\mu\text{m}$ .

The porous outer coating layer above the critical thickness considerably reduced the fracture strength of the coating, which led to the through-thickness cracking of the coating under the stress environment of fabrication, as demonstrated in my next study. The through-thickness crack had a strong impact on the penetration kinetics of solids and gases, which undesirably facilitated the U-Mo/Al IL formation and the coalescing of generated fission gases during irradiation. Based on the above observed microstructural features of the ZrN coating, the main limitation for the coating thickness was identified as the porous outer coating layer triggering through-thickness coating cracking. Thus, it was concluded that the optimum thickness of the ZrN diffusion barrier coating for U-7Mo/Al dispersion fuels is between 0.2 and 0.5  $\mu\text{m}$ .

Second, a mean 0.9  $\mu\text{m}$  ZrN coating layer was deposited on 45–90  $\mu\text{m}$ -sized U-7Mo substrate powders and then the microstructure of the as-fabricated ZrN coatings was measured as a function of the U-7Mo substrate size. The ZrN coating thickness increased with increasing the U-7Mo substrate size: the coating thickness extended from 0.55 (for 45  $\mu\text{m}$ -sized U-7Mo powder) to 1.17  $\mu\text{m}$  (for 90  $\mu\text{m}$ -sized powder). An analytical model, quantitatively describing the dependence of the coating thickness on the U-7Mo substrate size, was developed based on the configuration and deposition mechanism of the coating machine and the rotation position of the U-7Mo powders in the drum of the coating machine. Moreover, the fitting parameters obtained by using the experimental values were also applied to the developed model. In addition, with increasing the U-7Mo substrate size, the coating showed an increase in the density and area fraction of macroscopic defects, column and grain size, and crystallinity, which is probably due to the different coating thicknesses and deposition rates depending on the substrate size. The semi-analytical model can be used to accurately assess the ZrN coating thicknesses with the known U-7Mo powder sizes. The different microstructure characteristics and hence diffusion barrier capability of the coatings can lead to the undesired phenomenon in which a thin coating with a relatively undesired microstructure deposited on the small substrate powders and/or a thick porous coating on the large powders fails prematurely. Therefore, for the better diffusion barrier performance of the ZrN coating, optimization studies to improve the structural homogeneity and packing density should be performed, and additionally, the thickness limitation of the coatings is needed to avoid the porous outer coating layer.

Lastly, the effect of coating thickness and annealing temperature on ZrN non-reactively sputtered coating failure of U-Mo powders at heat-treatment temperature of temperature of dispersion-fuel-plate manufacturing. The fracture behavior of ZrN coatings on U-7Mo powders was investigated as a function of the coating thickness, U-7Mo substrate size, and annealing temperature by experiments and finite element simulations (FESs). By SEM surficial and cross-sectional image analysis, the fracture behavior of annealed ZrN coatings was examined. In addition to the experimental test, FESs with a developed model from the experiment were performed to calculate the induced stresses for given

annealing temperatures and coated powder structure and then evaluate the possibility of coating failure numerically. The FESs fully accounted for the coupled effects of residual stress of the as-deposited coating by adopting multi-step analysis, and the microstructure-related mechanical properties (grain boundary induced- strengthening, density, crack tip). The FES results showed the dependence of the fracture behavior of the coating on coating thickness, U-7Mo substrate size, and the annealing temperature: First, it was found that through-thickness cracking occurred from each specific coating thickness for 45 and 90  $\mu\text{m}$ -sized U-7Mo powders. This is caused by vertical surface cracks created along the porous structure of low fracture resistance which starts from 0.5  $\mu\text{m}$  thickness. Such generated surface cracks act as a crack tip, and lead to a fracture strength reduction proportional to its length. As a result, thicker coatings are subject to be fractured easily through their coating thickness direction by propagation of the surface cracks. Through-thickness cracking is suggested to be generated from 0.74 and 0.73  $\mu\text{m}$  coating thicknesses, respectively, for 45 and 90  $\mu\text{m}$ -sized U-7Mo powders at 500°C. Second, the induced stresses over the coating increase and tend to cause through-thickness cracking as annealing temperature increases. For a 0.74  $\mu\text{m}$ -thick coating on a 45  $\mu\text{m}$ -sized powder and a 1.06  $\mu\text{m}$ -thick coating on a 90  $\mu\text{m}$ -sized powder, the coating failure starts from 500°C and 400°C, respectively. These FE results were in close agreement with the experimental results. Investigations for the critical values of coating thickness and annealing temperature to initiate coating fracture presented in this study are expected to be one of the guidelines for coating design or processing temperature condition for dispersion fuel.

## 6.2. Conclusions

This study also found that the diffusion barrier performance of ZrN coating can be improved by preventing the through-thickness cracking of the coating during high temperature plate fabrication. For the structural integrity of ZrN coating, the following solutions can be proposed.

1. First, To sufficiently suppress the interaction layer growth of U-Mo/Al dispersion fuels during the entire operation time, a ZrN coating layer needs a thickness of 1  $\mu\text{m}$  based on the TRIM simulation result. However, according to ' $x = \sqrt{D \cdot t^2}$ ' (where  $x$ , and  $t$  are the thickness, and lifetime of a diffusion barrier coating, respectively, and  $D$  is the diffusivity of a passing material through the coating.), a significant increase in the diffusivity ( $D$ ), caused by the coating damage, should be avoided for the long lifetime ( $t$ ) even by reducing the coating thickness ( $x$ ). That is, the ZrN coating layer should be formed to a maximum thickness that is not damaged. Therefore, when considering the structural integrity of the ZrN coating at the normal fabrication temperature of 500°C, the optimum coating thickness is 0.74 and 0.73  $\mu\text{m}$  for 45 and 90  $\mu\text{m}$ -sized U-7Mo powders, respectively.
2. Second, in the case of a fixed tensile stress and coating thickness, smaller ZrN coating diameter (i.e., smaller U-Mo substrate) is advantageous to maintain the structural integrity of the coating.
3. Lastly, by using the U-7Mo substrate powders with a narrow size range, the thickness and structural homogeneity of the ZrN coating can be improved for the effective and reliable diffusion barrier performance.

### 6.3. Other uncertainties and Future works

To successfully prevent U-Mo/Al IL even at a high burnup, a ZrN diffusion barrier coating layer within the U-Mo/Al dispersion fuel plates should sustain the structural integrity during the entire manufacturing process of the dispersion fuel plate. Typically, a dispersion fuel plate is manufactured through a sequence of steps including mixing, compacting, assembling, welding, hot rolling with multiple heating, blister testing, cold rolling at room temperature, trimming, and inspection. Among these steps, the thermal stress induced at the high-temperature condition of the multiple heat-treatments, the mechanical stress induced during compacting, hot rolling, and cold rolling are suspected as critical sources that may damage the ZrN coating.

In this research, solutions to avoid the coating fracturing at a high heat-treatment temperature used in dispersion-fuel-plate fabrication were suggested based on the examined coating microstructure. However, solutions to ensure the structural integrity of the coating during the entire fabrication process should eventually be presented. Accordingly, the effects of the mechanical stresses induced from the other critical steps on the damage to a ZrN coating should be further investigated in the future.

## References

- [1] H. Etherington, *Nuclear engineering handbook*, vol. 1. McGraw-Hill New York, 1958.
- [2] I. A. E. Agency, *Research Reactor Core Conversion Guidebook Volume 5: Operations (appendices L-n)*. International Atomic Energy Agency, 1992.
- [3] D. Stahl, “Nuclear Converter Reactor Fuel Cycle Technology,” 1982.
- [4] A. Travelli, “US reduced enrichment research and test reactor (RERTR) program: accomplishments, plans, and schedules,” *Trans Am Nucl Soc;(United States)*, vol. 35, no. CONF-801107-, 1980.
- [5] J. L. Snelgrove, G. L. Hofman, M. K. Meyer, C. L. Trybus, and T. C. Wiencek, “Development of very-high-density low-enriched-uranium fuels1,” *Nucl Eng Des*, vol. 178, no. 1, pp. 119–126, 1997.
- [6] A. Travelli, “Progress of the US RERTR program,” 1998.
- [7] A. Loukianova and C. Hansell, “Leveraging US policy for a global commitment to HEU elimination,” *Nonproliferation Rev*, vol. 15, no. 2, pp. 159–183, 2008.
- [8] Y. S. Kim, “Uranium intermetallic fuels (U–Al, U–Si, U–Mo),” 2012.
- [9] G. L. Hofman, M. R. Finlay, and Y. S. Kim, “Post-irradiation analysis of low enriched U–Mo/Al dispersions fuel miniplatte tests, RERTR 4 and 5,” 2005.
- [10] S. Nazaré, “Low enrichment dispersion fuels for research and test reactors,” *J Nucl Mater*, vol. 124, pp. 14–24, 1984.
- [11] R. F. Domagala, T. C. Wiencek, and H. R. Thresh, “U–Si and U–Si–Al Dispersion Fuel Alloy Development for Research and Test Reactors,” *Nucl Technol*, vol. 62, no. 3, pp. 353–360, 1983.
- [12] D. D. Keiser, S. L. Hayes, M. K. Meyer, and C. R. Clark, “High-density, low-enriched uranium fuel for nuclear research reactors,” *JOM J Miner Met Mater Soc*, vol. 55, no. 9, pp. 55–58, 2003.
- [13] A. Travelli, “Proceedings of the 1978 international meeting on reduced enrichment for research and test reactors,” Argonne National Laboratory, 1993.
- [14] M. K. Meyer, T. C. Wiencek, S. L. Hayes, and G. L. Hofman, “Irradiation behavior of U6Mn–Al dispersion fuel elements,” *J Nucl Mater*, vol. 278, no. 2–3, pp. 358–363, 2000.
- [15] M. K. Meyer, G. L. Hofman, J. L. Snelgrove, C. R. Clark, S. L. Hayes, R. V Strain, J. M. Park, and K. H. Kim, “Irradiation Behavior of Uranium-Molybdenum Dispersion Fuel: Fuel Performance Data from RERTR-1 and RERTR-2,” in *Proceedings of the XXII RERTR Meeting*, 1999, pp. 3–8.



- [16] D. O. Leeeser, F. A. Rough, and A. A. Bauer, "Radiation stability of fuel elements for the Enrico Fermi power reactor," Atomic Power Development Associates, Inc., Detroit; Battelle Memorial Inst., Columbus, Ohio, 1958.
- [17] G. L. Hofman, R. F. Domagala, and G. L. Copeland, "Irradiation behavior of low-enriched U 6 Fe-Al dispersion fuel elements," *J Nucl Mater*, vol. 150, no. 2, pp. 238–243, 1987.
- [18] G. L. Hofman, L. C. Walters, and T. H. Bauer, "Metallic fast reactor fuels," *Prog Nucl Energy*, vol. 31, no. 1–2, pp. 83–110, 1997.
- [19] D. Petti, D. Crawford, and N. Chauvin, "Fuels for advanced nuclear energy systems," *MRS Bull*, vol. 34, no. 1, pp. 40–45, 2009.
- [20] D. Olander, "Nuclear fuels—present and future," *J Nucl Mater*, vol. 389, no. 1, pp. 1–22, 2009.
- [21] G. L. Hofman, M. K. Meyer, and J.-M. Park, "Observation on the irradiation behavior of U-Mo alloy dispersion fuel," 2000.
- [22] M. K. Meyer, G. L. Hofman, S. L. Hayes, C. R. Clark, T. C. Wienczek, J. L. Snelgrove, R. V. Strain, and K.-H. Kim, "Low-temperature irradiation behavior of uranium–molybdenum alloy dispersion fuel," *J Nucl Mater*, vol. 304, no. 2–3, pp. 221–236, 2002.
- [23] J. L. Snelgrove, G. L. Hofman, C. L. Trybus, and T. C. Wienczek, "Development of very-high-density fuels by the RERTR program," in *Proceedings of the International Meeting on Reduced Enrichment for Research and Test Reactors, Seoul, Korea*, 1996, pp. 7–10.
- [24] G.L. Hofman and J.L. Snelgrove, *No Title*, Vol. 10A. New York: VCH, 1994.
- [25] S. Van den Berghe, W. Van Renterghem, and A. Leenaers, "Transmission electron microscopy investigation of irradiated U–7 wt% Mo dispersion fuel," *J Nucl Mater*, vol. 375, no. 3, pp. 340–346, 2008.
- [26] G. L. Hofman, Y. S. Kim, M. R. Finlay, J. L. Snelgrove, S. L. Hayes, M. K. Meyer, and C. R. Clark, "Recent observations at the post-irradiation examination of low-enriched U-Mo miniplates irradiated to high burn-up," 2003.
- [27] A. Leenaers, S. Van den Berghe, E. Koonen, C. Jarousse, F. Huet, M. Trotabas, M. Boyard, S. Guillot, L. Sannen, and M. Verwerft, "Post-irradiation examination of uranium–7 wt% molybdenum atomized dispersion fuel," *J Nucl Mater*, vol. 335, no. 1, pp. 39–47, 2004.
- [28] Y. S. Kim and G. L. Hofman, "Improved performance of U-Mo dispersion fuel by Si addition in Al matrix.," Argonne National Lab.(ANL), Argonne, IL (United States), 2011.
- [29] W. Van Renterghem, A. Leenaers, and S. Van Den Berghe, "Transmission electron microscopy investigation of UAL x based MTR fuel," 2010.
- [30] J. Gan, B. Miller, D. Keiser Jr, A. Robinson, P. Medvedev, and D. Wachs, "TEM Characterization of Irradiated U3Si2/Al Dispersion Fuel," in *32nd International Meeting on Reduced Enrichment for Research and Test Reactors (RERTR)*, 2010.

- [31] R. C. Birtcher, J. W. Richardson, and M. H. Mueller, “Amorphization of U<sub>3</sub>Si<sub>2</sub> by ion or neutron irradiation,” *J Nucl Mater*, vol. 230, no. 2, pp. 158–163, 1996.
- [32] A. Leenaers, E. Koonen, Y. Parthoens, P. Lemoine, and S. Van den Berghe, “Post-irradiation examination of AlFeNi clad U<sub>3</sub>Si<sub>2</sub> fuel plates irradiated under severe conditions,” *J Nucl Mater*, vol. 375, no. 2, pp. 243–251, 2008.
- [33] A. Leenaers, S. Van den Berghe, E. Koonen, P. Jacquet, C. Jarousse, B. Guigon, A. Ballagny, and L. Sannen, “Microstructure of U<sub>3</sub>Si<sub>2</sub> fuel plates submitted to a high heat flux,” *J Nucl Mater*, vol. 327, no. 2–3, pp. 121–129, 2004.
- [34] G. L. Hofman, M. K. Meyer, and A. E. Ray, “Design of high density gamma-phase uranium alloys for LEU dispersion fuel applications,” in *Proceedings of the 1998 International Reduced Enrichment for Test Reactor Conference*, 1998.
- [35] A. Leenaers, S. Van den Berghe, W. Van Renterghem, F. Charollais, P. Lemoine, C. Jarousse, A. Röhrmoser, and W. Petry, “Irradiation behavior of ground U (Mo) fuel with and without Si added to the matrix,” *J Nucl Mater*, vol. 412, no. 1, pp. 41–52, 2011.
- [36] A. Leenaers, S. Van den Berghe, E. Koonen, V. Kuzminov, and C. Detavernier, “Fuel swelling and interaction layer formation in the {SELENIUM} Si and ZrN coated U(Mo) dispersion fuel plates irradiated at high power in {BR2},” *J Nucl Mater*, vol. 458, pp. 380–393, 2015.
- [37] Y. S. Kim and G. L. Hofman, “Irradiation behavior of the interaction product of U-Mo fuel particle dispersion in an Al matrix,” *J Nucl Mater*, vol. 425, no. 1–3, pp. 181–187, 2012.
- [38] K.-H. Kim, J.-M. Park, C.-K. Kim, G. L. Hofman, and M. K. Meyer, “Irradiation behavior of atomized U–10wt.% Mo alloy aluminum matrix dispersion fuel meat at low temperature,” *Nucl Eng Des*, vol. 211, no. 2–3, pp. 229–235, 2002.
- [39] A. Leenaers, S. Van Den Berghe, and C. Detavernier, “Surface engineering of low enriched uranium-molybdenum,” *J Nucl Mater*, vol. 440, no. 1–3, pp. 220–228, 2013.
- [40] Y. S. Kim, G. Y. Jeong, D.-S. Sohn, and L. M. Jamison, “Pore growth in U-Mo/Al dispersion fuel,” *J Nucl Mater*, vol. 478, pp. 275–286, 2016.
- [41] W. D. Nix, “WD Nix and BM Clemens, *J. Mater. Res.* 14, 3467 (1999).,” *J Mater Res*, vol. 14, p. 3467, 1999.
- [42] G. L. Hofman and M. K. Meyer, “Progress in irradiation performance of experimental uranium-molybdenum dispersion fuel,” 2002.
- [43] K.-H. Kim, J.-M. Park, C.-K. Kim, G. L. Hofman, M. K. Meyer, and J. L. Snelgrove, “Stable in-reactor performances at low temperature of U-10wt.% Mo dispersion fuel containing centrifugally atomized powder.,” Argonne National Lab., IL (US), 2001.
- [44] E. Perez, “Interdiffusion Behavior Of U-mo Alloys In Contact With Al And Al-si Alloys,” 2011.

- [45] L. Kniznik, P. R. Alonso, P. H. Gargano, M. D. Forti, and G. H. Rubiolo, “First principles study of U-Al system ground state,” *Procedia Mater Sci*, vol. 1, pp. 514–519, 2012.
- [46] T. Zweifel, “Fission gas behaviour and interdiffusion layer growth in in-pile and out-of-pile irradiated U-Mo/Al nuclear fuels,” 2014.
- [47] B. A. Latella, B. K. Gan, K. E. Davies, D. R. McKenzie, and D. G. McCulloch, “Titanium nitride/vanadium nitride alloy coatings: mechanical properties and adhesion characteristics,” *Surf Coatings Technol*, vol. 200, no. 11, pp. 3605–3611, 2006.
- [48] H. Noël, O. Tougait, and S. Dubois, “Phase relations in the U–Mo–Al ternary system,” *J Nucl Mater*, vol. 389, no. 1, pp. 93–97, 2009.
- [49] J. M. Park, H. J. Ryu, S. J. Oh, D. B. Lee, C. K. Kim, Y. S. Kim, and G. L. Hofman, “Effect of Si and Zr on the interdiffusion of U–Mo alloy and Al,” *J Nucl Mater*, vol. 374, no. 3, pp. 422–430, 2008.
- [50] A. Ewh, E. Perez, D. D. Keiser, and Y. H. Sohn, “Microstructural Characterization of U-Nb-Zr, U-Mo-Nb, and U-Mo-Ti Alloys via Electron Microscopy,” *J phase equilibria Diffus*, vol. 31, no. 3, pp. 216–222, 2010.
- [51] Y. S. Kim, G. L. Hofman, A. B. Robinson, D. M. Wachs, H. J. Ryu, J. M. Park, and J. H. Yang, “Irradiation performance of U–Mo–Ti and U–Mo–Zr dispersion fuels in Al–Si matrixes,” *J Nucl Mater*, vol. 427, no. 1–3, pp. 233–238, 2012.
- [52] Y. S. Kim, J. M. Park, H. J. Ryu, Y. H. Jung, and G. L. Hofman, “Reduced interaction layer growth of U–Mo dispersion in Al–Si,” *J Nucl Mater*, vol. 430, no. 1–3, pp. 50–57, 2012.
- [53] A. Leenaers, S. Van den Berghe, J. Van Eyken, E. Koonen, F. Charollais, P. Lemoine, Y. Calzavara, H. Guyon, C. Jarousse, and D. Geslin, “Microstructural evolution of U (Mo)–Al (Si) dispersion fuel under irradiation–Destructive analyses of the LEONIDAS E-FUTURE plates,” *J Nucl Mater*, vol. 441, no. 1–3, pp. 439–448, 2013.
- [54] S. Van den Berghe, Y. Parthoens, F. Charollais, Y. S. Kim, A. Leenaers, E. Koonen, V. Kuzminov, P. Lemoine, C. Jarousse, and H. Guyon, “Swelling of U (Mo)–Al (Si) dispersion fuel under irradiation–Non-destructive analyses of the LEONIDAS E-FUTURE plates,” *J Nucl Mater*, vol. 430, no. 1–3, pp. 246–258, 2012.
- [55] D. D. Keiser, J.-F. Jue, B. D. Miller, J. Gan, A. B. Robinson, P. G. Medvedev, J. W. Madden, and G. A. Moore, “Microstructural characterization of a Mg matrix U-Mo dispersion fuel plate irradiated in the advanced test reactor to high fission density: SEM results,” *Metall Mater Trans E*, vol. 3, no. 2, pp. 71–89, 2016.
- [56] K. Huang, H. Heinrich, D. D. Keiser, and Y. H. Sohn, “Fuel-Matrix Chemical Interaction Between U-7wt.% Mo Alloy and Mg,” in *Defect and Diffusion Forum*, 2013, vol. 333, pp. 199–206.

- [57] J. Gan, D. D. Keiser Jr, B. D. Miller, J. F. Jue, A. B. Robinson, and J. Madden, “TEM characterization of irradiated U-7Mo/Mg dispersion fuel,” *J Nucl Mater*, vol. 494, pp. 380–397, 2017.
- [58] H.-Y. Chiang, “Material selection of UMo fuel for research reactors: Swift heavy ion irradiation studies.” Universitätsbibliothek der TU München, 2014.
- [59] T. Zweifel, H. Palancher, A. Leenaers, A. Bonnin, V. Honkimaki, R. Tucoulou, S. Van Den Berghe, R. Jungwirth, F. Charollais, and W. Petry, “Crystallographic study of Si and ZrN coated U–Mo atomised particles and of their interaction with Al under thermal annealing,” *J Nucl Mater*, vol. 442, no. 1–3, pp. 124–132, 2013.
- [60] R. Jungwirth, T. Zweifel, H.-Y. Chiang, W. Petry, S. Van den Berghe, and A. Leenaers, “Heavy ion irradiation of UMo/Al samples {PVD} coated with Si and ZrN layers,” *J Nucl Mater*, vol. 434, no. 1–3, pp. 296–302, 2013.
- [61] D. D. Keiser, E. Perez, T. Wiencek, A. Leenaers, and S. Van Den Berghe, “Microstructural characterization of a thin film ZrN diffusion barrier in an As-fabricated U-7Mo/Al matrix dispersion fuel plate,” *J Nucl Mater*, vol. 458, pp. 406–418, 2015.
- [62] J.-H. Kim, G. Y. Jeong, S. Kim, Y. J. Jeong, and D.-S. Sohn, “Effect of coating thickness and annealing temperature on ZrN coating failure of U-Mo particles under heat treatment,” *J Nucl Mater*, vol. 507, pp. 347–359, 2018.
- [63] J.-H. Kim, G. Y. Jeong, S. Kim, Y. J. Jeong, J. M. Park, and D.-S. Sohn, “Dependence of thickness, morphology, and crystallographic properties of Mo and ZrN coatings on U-Mo substrate size,” *J Nucl Mater*, 2018.
- [64] S. Van den Berghe and P. Lemoine, “Review of 15 years of high-density low-enriched UMo dispersion fuel development for research reactors in Europe,” *Nucl Eng Technol*, vol. 46, no. 2, pp. 125–146, 2014.
- [65] D. R. McGregor Jr, “Growth Optimization and Characterization of Reactively Sputtered Zirconium Nitride Thin Films for III-V Buffer Layer Applications,” 2002.
- [66] V. V Iakovlev, A. L. IZHUTOV, V. V Alexandrov, A. E. NOVOSELOV, V. A. STARKOV, A. A. SHELDYAKOV, V. Y. U. SHISHIN, I. V DOBRIKOVA, A. V VATULIN, and V. B. SUPRUN, “THE MAIN RESULTS OF INVESTIGATION OF MODIFIED DISPERSION LEU U–MO FUEL TESTED IN THE MIR REACTOR,” *HOT CELL POST-IRRADIATION Exam POOLSIDE Insp Nucl FUEL*, p. 217, 2013.
- [67] L. Sudderth, D. Perez-Nunez, D. Keiser, and S. McDeavitt, “Fabrication of ZrN Barrier Coatings for U-Mo Microspheres Via Fluidized Bed Chemical Vapor Deposition Using a Metalorganic Precursor,” *Nucl Technol*, vol. 202, no. 1, pp. 81–93, 2018.

- [68] S. M. Rossnagel, S. W. D. Sproul, and K. O. Legg, “Opportunities for Innovation Advanced Surface Engineering,” *Sproul WD LK, Ed Switz Technomic Publ Co*, 1995.
- [69] S. Van den Berghe, A. Leenaers, and C. Detavernier, “SELENIUM fuel: Surface engineering of U (Mo) particles to optimise fuel performance,” *Trans RRFM-2010*, pp. 21–25, 2010.
- [70] J. A. Thornton and D. W. Hoffman, “Stress-related effects in thin films,” *Thin Solid Films*, vol. 171, no. 1, pp. 5–31, 1989.
- [71] M.-A. Nicolet, “Diffusion barriers in thin films,” *Thin Solid Films*, vol. 52, no. 3, pp. 415–443, 1978.
- [72] K. Huang, C. C. Kammerer, D. D. Keiser, and Y. H. Sohn, “Diffusion barrier selection from refractory metals (Zr, Mo and Nb) via interdiffusion investigation for U-Mo RERTR fuel alloy,” *J phase equilibria Diffus*, vol. 35, no. 2, pp. 146–156, 2014.
- [73] K. E. Huang, “Diffusion And Reaction In Selected Uranium Alloy System,” 2012.
- [74] K. Huang, Y. Park, D. D. Keiser, and Y. H. Sohn, “Interdiffusion between Zr diffusion barrier and U-Mo alloy,” *J Phase Equilibria Diffus*, vol. 33, no. 6, pp. 443–449, 2012.
- [75] W. C. Thurber and R. J. Beaver, “DEVELOPMENT OF SILICON-MODIFIED 48 Wt.% U-AL ALLOYS FOR ALUMINUM PLATE-TYPE FUEL ELEMENTS,” Oak Ridge National Lab., Tenn., 1959.
- [76] V. M. T. O.A. Golosov, S.A. Averin, M.S. Lyutikova, V.V. Shushlebin and G. A. B. B.V. Popov, “Proceedings of the 30th International Meeting on Reduced Enrichment for Research and Test Reactors (RERTR),” 2008.
- [77] S. V. den B. M. Ripert, S. Dubois, J. Noirot, P. Boulcourt, P. Lemoine and C. J. A. Leenaers, A. Rohrmoser, W. Petry, “Transactions of RRFM-2008,” p. 2008.
- [78] Y. S. Kim, J. M. Park, K. H. Lee, B. O. Yoo, H. J. Ryu, and B. Ye, “In-pile test results of U-silicide or U-nitride coated U-7Mo particle dispersion fuel in Al,” *J Nucl Mater*, vol. 454, no. 1, pp. 238–246, 2014.
- [79] W. J. Kim, H. Palancher, H. J. Ryu, J. M. Park, J. M. Nam, A. Bonnin, V. Honkimäki, F. Charollais, and P. Lemoine, “Phase analyses of silicide or nitride coated U–Mo and U–Mo–Ti particle dispersion fuel after out-of-pile annealing,” *J Alloys Compd*, vol. 589, pp. 94–100, 2014.
- [80] A. L. Izhutov, V. V Iakovlev, A. E. Novoselov, V. A. Starkov, A. A. Sheldyakov, V. Y. Shishin, V. M. Kosenkov, A. V Vatulin, I. V Dobrikova, and V. B. Suprun, “Comparative Analysis of Structural Changes in U-Mo Dispersed Fuel of Full-Size Fuel Elements and Mini-Rods Irradiated in the MIR Reactor,” *Nucl Eng Technol*, vol. 45, no. 7, pp. 859–870, 2013.

- [81] X. ILTIS, H. PALANCHER, F. VANNI, J. ALLENOU, B. STEPNIK, A. LEENAERS, S. VAN DEN BERGHE, D. D. KEISER, and I. GLAGOLENKO, “Characterization of fresh EMPiRE and SEMPER FIDELIS plates with PVD-coated U (Mo) particles.”
- [82] L. He, M. Bachhav, D. D. Keiser, J. W. Madden, E. Perez, B. D. Miller, J. Gan, W. Van Renterghem, A. Leenaers, and S. Van den Berghe, “STEM-EDS/EELS and APT characterization of ZrN coatings on UMo fuel kernels,” *J Nucl Mater*, vol. 511, pp. 174–182, 2018.
- [83] N. R. Council, *Coatings for high-temperature structural materials: trends and opportunities*. National Academies Press, 1996.
- [84] X. J. Zheng, Y. C. Zhou, and H. Zhong, “Dependence of fracture toughness on annealing temperature in Pb(Zr<sub>0.52</sub>Ti<sub>0.48</sub>)O<sub>3</sub> thin films produced by metal organic decomposition,” *J Mater Res*, vol. 18, no. 3, pp. 578–584, 2003.
- [85] K. S. Gadre and T. L. Alford, “Crack formation in TiN films deposited on Pa-n due to large thermal mismatch,” *Thin Solid Films*, vol. 394, no. 1–2, pp. 124–129, 2001.
- [86] R.-M. Keller, S. P. Baker, and E. Arzt, “Quantitative analysis of strengthening mechanisms in thin Cu films: Effects of film thickness, grain size, and passivation,” *J Mater Res*, vol. 13, no. 5, pp. 1307–1317, 1998.
- [87] M. J. Cordill and A. A. Taylor, “Thickness effect on the fracture and delamination of titanium films,” *Thin Solid Films*, vol. 589, pp. 209–214, 2015.
- [88] R. Venkatraman and J. C. Bravman, “Separation of film thickness and grain boundary strengthening effects in Al thin films on Si,” *J Mater Res*, vol. 7, no. 8, pp. 2040–2048, 1992.
- [89] J. W. M. DuMond and J. P. Youtz, “Selective X-ray diffraction from artificially stratified metal films deposited by evaporation,” *Phys Rev*, vol. 48, no. 8, p. 703, 1935.
- [90] I. Petrov, P. B. Barna, L. Hultman, and J. E. Greene, “Microstructural evolution during film growth,” *J Vac Sci Technol A Vacuum, Surfaces, Film*, vol. 21, no. 5, pp. S117–S128, 2003.
- [91] J. Singh, F. Quli, D. E. Wolfe, J. T. Schriempf, and J. Singh, “An overview: Electron beam-physical vapor deposition technology-present and future applications,” *Appl Res Lab Pennsylvania State Univ USA*, 1999.
- [92] *ICDD no. 00-035-0753*. .
- [93] H. Behret, J. Gilbert, P. Holland, W. Klein, W. Pjienenburg, T. Tavares, S. Yehuda, P. Dysseler, R.-P. Martin, and J. Miyamoto, “International Union of Pure and Applied Chemistry,” 1979.
- [94] M. W. Chase Jr and N.-J. T. Tables, “Data reported in NIST standard reference database 69, June 2005 release: NIST Chemistry WebBook,” *J Phys Chem Ref Data, Monogr*, vol. 9, pp. 1–1951, 1998.

- [95] L. Krusin-Elbaum and M. Wittmer, "Oxidation kinetics of ZrN thin films," *Thin Solid Films*, vol. 107, no. 1, pp. 111–116, 1983.
- [96] H. O. Pierson, *Handbook of refractory carbides and nitrides: properties, characteristics, processing and applications*. William Andrew, 1996.
- [97] A. Leenaers, "Surface-engineered low-enriched Uranium-Molybdenum fuel for research reactors," *Univ Ghent, Dep Solid State Sci Ghent, Belgium*, 2014.
- [98] J. Rest, Y. S. Kim, G. L. Hofman, M. K. Meyer, and S. L. Hayes, "U-Mo fuels handbook. Version 1.0," Argonne National Lab.(ANL), Argonne, IL (United States), 2006.
- [99] W. H. Bragg and W. L. Bragg, "The Reflection of X-rays by Crystals," *Proc R Soc London Ser A*, vol. 88, no. 605, p. 428 LP-438, Jul. 1913.
- [100] J. Wang, F. Yang, X. Wei, Y. Zhang, L. Wei, J. Zhang, Q. Tang, B. Guo, and L. Xu, "Controlled growth of conical nickel oxide nanocrystals and their high performance gas sensing devices for ammonia molecule detection," *Phys Chem Chem Phys*, vol. 16, no. 31, pp. 16711–16718, 2014.
- [101] N. C. Halder and C. N. J. Wagner, "Analysis of the Broadening of Powder Pattern Peaks Using Variance, Integral Breadth, and Fourier Coefficients of the Line Profile," in *Advances in X-Ray Analysis: Volume 9 Proceedings of the Fourteenth Annual Conference on Applications of X-Ray Analysis Held August 25--27, 1965*, G. R. Mallett, M. J. Fay, and W. M. Mueller, Eds. Boston, MA: Springer US, 1966, pp. 91–102.
- [102] N. C. Halder and C. N. J. Wagner, "Separation of particle size and lattice strain in integral breadth measurements," *Acta Crystallogr*, vol. 20, no. 2, pp. 312–313, 1966.
- [103] *International Centre for Diffraction Data (ICDD) card No.03-065-2905*. .
- [104] S. Lin, J. Zhang, R. Zhu, S. Fu, and D. Yun, "Effects of sputtering pressure on microstructure and mechanical properties of ZrN films deposited by magnetron sputtering," *Mater Res Bull*, vol. 105, pp. 231–236, 2018.
- [105] K. H. Kim, D. B. Lee, C. K. Kim, G. E. Hofman, and K. W. Paik, "Characterization of U-2 wt% Mo and U-10 wt% Mo alloy powders prepared by centrifugal atomization," *J Nucl Mater*, vol. 245, no. 2, pp. 179–184, 1997.
- [106] A. Telama, T. Mäntylä, and P. Kettunen, "A study of defects in sputtered TiN coatings by electrochemical polarization," *J Vac Sci Technol A Vacuum, Surfaces, Film*, vol. 4, no. 6, pp. 2911–2914, 1986.
- [107] P. Panjan, D. K. Merl, F. Zupanič, M. Čekada, and M. Panjan, "SEM study of defects in PVD hard coatings using focused ion beam milling," *Surf Coatings Technol*, vol. 202, no. 11, pp. 2302–2305, 2008.
- [108] W. M. Haynes, *CRC handbook of chemistry and physics*. CRC press, 2014.

- [109] L. Lutterotti, D. Chateigner, S. Ferrari, and J. Ricote, “Texture, residual stress and structural analysis of thin films using a combined X-ray analysis,” *Thin Solid Films*, vol. 450, no. 1, pp. 34–41, 2004.
- [110] J. Peng, V. Ji, W. Seiler, A. Tomescu, A. Levesque, and A. Bouteville, “Residual stress gradient analysis by the GIXRD method on CVD tantalum thin films,” *Surf Coatings Technol*, vol. 200, no. 8, pp. 2738–2743, 2006.
- [111] F. Vaz, L. Rebouta, P. Goudeau, J. P. Rivière, E. Schäffer, G. Kleer, and M. Bodmann, “Residual stress states in sputtered Ti<sub>1-x</sub>Si<sub>x</sub>Ny films,” *Thin Solid Films*, vol. 402, no. 1, pp. 195–202, 2002.
- [112] E. Atar, C. Sarioglu, U. Demirler, E. Sabri Kayali, and H. Cimenoglu, “Residual stress estimation of ceramic thin films by X-ray diffraction and indentation techniques,” *Scr Mater*, vol. 48, no. 9, pp. 1331–1336, 2003.
- [113] J. Zalesak, J. Todt, R. Pitonak, A. Köpf, R. Weißenbacher, B. Sartory, M. Burghammer, R. Daniel, and J. Keckes, “Combinatorial refinement of thin-film microstructure, properties and process conditions: iterative nanoscale search for self-assembled TiAlN nanolamellae,” *J Appl Crystallogr*, vol. 49, no. 6, pp. 2217–2225, 2016.
- [114] A. A. Volinsky, J. Vella, I. S. Adihetty, V. i Sarihan, L. Mercado, B. H. Yeung, and W. W. Gerberich, “Microstructure and mechanical properties of electroplated Cu thin films,” *MRS Online Proc Libr Arch*, vol. 649, 2000.
- [115] J. M. Oparowski, R. D. Sisson Jr, and R. R. Biederman, “The effects of processing parameters on the microstructure and properties of sputter-deposited TiW thin film diffusion barriers,” *Thin Solid Films*, vol. 153, no. 1–3, pp. 313–328, 1987.
- [116] Y.-J. Lee, H.-W. Yeon, S.-Y. Jung, S.-K. Na, J.-S. Park, Y.-Y. Choi, H.-J. Lee, O.-S. Song, and Y.-C. Joo, “Effects of film thickness and deposition rate on the diffusion barrier performance of titanium nitride in Cu-through silicon vias,” *Electron Mater Lett*, vol. 10, no. 1, pp. 275–279, 2014.
- [117] M. Mühlbacher, “High-resolution characterization of TiN diffusion barrier layers.” Linköping University Electronic Press, 2015.
- [118] M. Hecker, R. Hübner, R. Ecke, S. Schulz, H.-J. Engelmann, H. Stegmann, V. Hoffmann, N. Mattern, T. Gessner, and E. Zschech, “Effect of annealing on the microstructure of ultrathin tungsten nitride diffusion barriers for copper metallization,” *Microelectron Eng*, vol. 64, no. 1–4, pp. 269–277, 2002.
- [119] J. Zou, B. Liu, L. Lin, Y. Lu, Y. Dong, G. Jiao, F. Ma, and Q. Li, “Investigation of microstructure and properties of ultrathin graded ZrN<sub>x</sub> self-assembled diffusion barrier in deep



- nano-vias prepared by plasma ion immersion implantation,” *Appl Surf Sci*, vol. 427, pp. 950–955, 2018.
- [120] G. Janssen, F. D. Tichelaar, and C. C. G. Visser, “Stress gradients in CrN coatings,” *J Appl Phys*, vol. 100, no. 9, p. 93512, 2006.
- [121] R. W. Hoffman, “Mechanical properties of non-metallic thin films,” in *Physics of nonmetallic thin films*, Springer, 1976, pp. 273–353.
- [122] W. D. Nix and B. M. Clemens, “Crystallite coalescence: A mechanism for intrinsic tensile stresses in thin films,” *J Mater Res*, vol. 14, no. 8, pp. 3467–3473, 1999.
- [123] E. Chason, B. W. Sheldon, L. B. Freund, J. A. Floro, and S. J. Hearne, “Origin of compressive residual stress in polycrystalline thin films,” *Phys Rev Lett*, vol. 88, no. 15, p. 156103, 2002.
- [124] S. C. Seel, C. V Thompson, S. J. Hearne, and J. A. Floro, “Tensile stress evolution during deposition of Volmer–Weber thin films,” *J Appl Phys*, vol. 88, no. 12, pp. 7079–7088, 2000.
- [125] C. V Thompson, “Grain growth in thin films,” *Annu Rev Mater Sci*, vol. 20, no. 1, pp. 245–268, 1990.
- [126] J.-H. Huang, H.-C. Yang, X.-J. Guo, and G.-P. Yu, “Effect of film thickness on the structure and properties of nanocrystalline ZrN thin films produced by ion plating,” *Surf Coatings Technol*, vol. 195, no. 2–3, pp. 204–213, 2005.
- [127] E. Perez, B. Yao, D. D. Keiser Jr, and Y. H. Sohn, “Microstructural analysis of as-processed U–10 wt.% Mo monolithic fuel plate in AA6061 matrix with Zr diffusion barrier,” *J Nucl Mater*, vol. 402, no. 1, pp. 8–14, 2010.
- [128] L. Hultman, J. Sundgren, and J. E. Greene, “Formation of polyhedral N<sub>2</sub> bubbles during reactive sputter deposition of epitaxial TiN (100) films,” *J Appl Phys*, vol. 66, no. 2, pp. 536–544, 1989.
- [129] C.-S. Shin, D. Gall, Y.-W. Kim, N. Hellgren, I. Petrov, and J. E. Greene, “Development of preferred orientation in polycrystalline NaCl-structure  $\delta$ -TaN layers grown by reactive magnetron sputtering: Role of low-energy ion surface interactions,” *J Appl Phys*, vol. 92, no. 9, pp. 5084–5093, 2002.
- [130] A. J. Detor, A. M. Hodge, E. Chason, Y. Wang, H. Xu, M. Conyers, A. Nikroo, and A. Hamza, “Stress and microstructure evolution in thick sputtered films,” *Acta Mater*, vol. 57, no. 7, pp. 2055–2065, 2009.
- [131] H. Windischmann, “An intrinsic stress scaling law for polycrystalline thin films prepared by ion beam sputtering,” *J Appl Phys*, vol. 62, no. 5, pp. 1800–1807, 1987.
- [132] G. Carter, “Peening in ion-assisted thin-film deposition: a generalized model,” *J Phys D Appl Phys*, vol. 27, no. 5, p. 1046, 1994.

- [133] N. A. Marks, D. R. McKenzie, B. A. Pailthorpe, M. Bernasconi, and M. Parrinello, “Ab initio simulations of tetrahedral amorphous carbon,” *Phys Rev B*, vol. 54, no. 14, p. 9703, 1996.
- [134] P. R. Guduru, E. Chason, and L. B. Freund, “Mechanics of compressive stress evolution during thin film growth,” *J Mech Phys Solids*, vol. 51, no. 11–12, pp. 2127–2148, 2003.
- [135] C.-W. Pao, S. M. Foiles, E. B. Webb III, D. J. Srolovitz, and J. A. Floro, “Thin film compressive stresses due to adatom insertion into grain boundaries,” *Phys Rev Lett*, vol. 99, no. 3, p. 36102, 2007.
- [136] G. Knuyt, “A model for the behaviour of tensile and compressive residual stresses developed in thin films produced by ion beam-assisted deposition techniques,” *Thin Solid Films*, vol. 467, no. 1–2, pp. 275–283, 2004.
- [137] K. Müller, “Stress and microstructure of sputter-deposited thin films: Molecular dynamics investigations,” *J Appl Phys*, vol. 62, no. 5, pp. 1796–1799, 1987.
- [138] C. A. Davis, “A simple model for the formation of compressive stress in thin films by ion bombardment,” *Thin Solid Films*, vol. 226, no. 1, pp. 30–34, 1993.
- [139] G. Abadias and P. Guerin, “In situ stress evolution during magnetron sputtering of transition metal nitride thin films,” *Appl Phys Lett*, vol. 93, no. 11, p. 111908, 2008.
- [140] J. Proost and F. Spaepen, “Evolution of the growth stress, stiffness, and microstructure of alumina thin films during vapor deposition,” *J Appl Phys*, vol. 91, no. 1, pp. 204–216, 2002.
- [141] A. Javaid, “Membranes for solubility-based gas separation applications,” *Chem Eng J*, vol. 112, no. 1–3, pp. 219–226, 2005.
- [142] A. F. Ismail, K. C. Khulbe, and T. Matsuura, “Fundamentals of Gas Permeation Through Membranes,” in *Gas Separation Membranes*, Springer, 2015, pp. 11–35.
- [143] A. J. Edwards, “HP Klug and LE Alexander, x-ray diffraction procedures for polycrystalline and amorphous materials: Wiley-Interscience, New York, 2nd edn., 1974, xxv+ 966 pp. price£ 18.55.” Elsevier, 1975.
- [144] K. Aryal, H. Khatri, R. W. Collins, and S. Marsillac, “In situ and ex situ studies of molybdenum thin films deposited by rf and dc magnetron sputtering as a back contact for CIGS solar cells,” *Int J Photoenergy*, vol. 2012, 2012.
- [145] W. Qin, T. Nagase, Y. Umakoshi, and J. A. Szpunar, “Relationship between microstrain and lattice parameter change in nanocrystalline materials,” *Philos Mag Lett*, vol. 88, no. 3, pp. 169–179, 2008.
- [146] P. Jin and S. Maruno, “Bias Effect on the Microstructure and Diffusion Barrier Capability of Sputtered TiN and TiOxNy Films,” *Jpn J Appl Phys*, vol. 31, no. 5R, p. 1446, 1992.
- [147] K. Lu, “Nanocrystalline metals crystallized from amorphous solids: nanocrystallization, structure, and properties,” *Mater Sci Eng R Reports*, vol. 16, no. 4, pp. 161–221, 1996.

- [148] K. Lu, R. Lück, and B. Predel, "Variation of the interfacial energy with grain size in nanocrystalline materials," *Mater Sci Eng A*, vol. 179, pp. 536–540, 1994.
- [149] P. P. Chattopadhyay, P. M. G. Nambissan, S. K. Pabi, and I. Manna, "Polymorphic bcc to fcc transformation of nanocrystalline niobium studied by positron annihilation," *Phys Rev B*, vol. 63, no. 5, p. 54107, 2001.
- [150] J. W. Flocken and J. R. Hardy, "Asymptotic lattice displacements about point defects in cubic metals," *Phys Rev B*, vol. 1, no. 6, p. 2447, 1970.
- [151] J. W. Christian, *The theory of transformations in metals and alloys*. Newnes, 2002.
- [152] P. G. Sanders, A. B. Witney, J. R. Weertman, R. Z. Valiev, and R. W. Siegel, "Residual stress, strain and faults in nanocrystalline palladium and copper," *Mater Sci Eng Mater*, vol. 204, no. 1, pp. 7–11, 1995.
- [153] Y. H. Zhao, K. Zhang, and K. Lu, "Structure characteristics of nanocrystalline element selenium with different grain sizes," *Phys Rev B*, vol. 56, no. 22, p. 14322, 1997.
- [154] T. R. Malow and C. C. Koch, "Grain growth in nanocrystalline iron prepared by mechanical attrition," *Acta Mater*, vol. 45, no. 5, pp. 2177–2186, 1997.
- [155] P. Quintana, A. I. Oliva, O. Ceh, J. E. Corona, and M. Aguilar, "Thickness effects on aluminum thin films," *Superf y vacío*, no. 9, 1999.
- [156] N. G. Semaltianos, "Thermally evaporated aluminium thin films," *Appl Surf Sci*, vol. 183, no. 3–4, pp. 223–229, 2001.
- [157] M. Aguilar, P. Quintana, and A. I. Oliva, "Thickness–stress relations in aluminum thin films," *Mater Manuf Process*, vol. 17, no. 1, pp. 57–65, 2002.
- [158] S.-J. Hwang, J.-H. Lee, C.-O. Jeong, and Y.-C. Joo, "Effect of film thickness and annealing temperature on hillock distributions in pure Al films," *Scr Mater*, vol. 56, no. 1, pp. 17–20, 2007.
- [159] M. Higo, X. Lu, U. Mazur, and K. W. Hipps, "Preparation of atomically smooth aluminum films: Characterization by transmission electron microscopy and atomic force microscopy," *Langmuir*, vol. 13, no. 23, pp. 6176–6182, 1997.
- [160] C. W. Hollars and R. C. Dunn, "Evaluation of thermal evaporation conditions used in coating aluminum on near-field fiber-optic probes," *Rev Sci Instrum*, vol. 69, no. 4, pp. 1747–1752, 1998.
- [161] C.-P. Liu and H.-G. Yang, "Deposition temperature and thickness effects on the characteristics of dc-sputtered ZrN<sub>x</sub> films," *Mater Chem Phys*, vol. 86, no. 2–3, pp. 370–374, 2004.
- [162] A. E.-H. B. Kashyout, H. M. A. Soliman, H. A. Gabal, P. A. Ibrahim, and M. Fathy, "Preparation and characterization of DC sputtered molybdenum thin films," *Alexandria Eng J*, vol. 50, no. 1, pp. 57–63, 2011.

- [163] A. Y. Chen, Y. Bu, Y. T. Tang, Y. Wang, F. Liu, X. F. Xie, and J. F. Gu, “Deposition-rate dependence of orientation growth and crystallization of Ti thin films prepared by magnetron sputtering,” *Thin Solid Films*, vol. 574, pp. 71–77, 2015.
- [164] H. Qiu, F. Wang, P. Wu, L. Pan, L. Li, L. Xiong, and Y. Tian, “Effect of deposition rate on structural and electrical properties of Al films deposited on glass by electron beam evaporation,” *Thin Solid Films*, vol. 414, no. 1, pp. 150–153, 2002.
- [165] M. Higo, K. Fujita, M. Mitsushio, T. Yoshidome, and T. Kakoi, “Epitaxial growth and surface morphology of aluminum films deposited on mica studied by transmission electron microscopy and atomic force microscopy,” *Thin Solid Films*, vol. 516, no. 1, pp. 17–24, 2007.
- [166] M. Higo, K. Fujita, Y. Tanaka, M. Mitsushio, and T. Yoshidome, “Surface morphology of metal films deposited on mica at various temperatures observed by atomic force microscopy,” *Appl Surf Sci*, vol. 252, no. 14, pp. 5083–5099, 2006.
- [167] J. Podbrský and V. Drahoš, “Electron microscope study of aluminium films evaporated on air-cleaved sodium chloride,” *Czechoslov J Phys B*, vol. 19, no. 2, pp. 217–221, 1969.
- [168] D. J. Semin and K. L. Rowlen, “Influence of vapor deposition parameters on SERS active Ag film morphology and optical properties,” *Anal Chem*, vol. 66, no. 23, pp. 4324–4331, 1994.
- [169] U. J. Quaade and K. Pantleon, “Orientationally ordered ridge structures of aluminum films on hydrogen terminated silicon,” *Thin Solid Films*, vol. 515, no. 4, pp. 2066–2072, 2006.
- [170] V. Starý, “Epitaxial growth of Al thin films on mica and investigation of film structure,” *Czechoslov J Phys B*, vol. 26, no. 8, pp. 882–889, 1976.
- [171] V. S. Chernysh, V. S. Kulikauskas, A. S. Patrakeevev, K. M. Abdul-Cader, and V. I. Shulga, “Angular distribution of atoms sputtered from silicon by 1–10 keV Ar ions,” *Radiat Eff Defects Solids*, vol. 159, no. 3, pp. 149–155, 2004.
- [172] V. S. Chernysh, A. S. Patrakeevev, and V. I. Shulga, “Angular distribution of atoms sputtered from germanium by 1–20 keV Ar ions,” *Radiat Eff Defects Solids*, vol. 161, no. 12, pp. 701–707, 2006.
- [173] V. S. Chernysh and A. S. Patrakeevev, “Angular distribution of atoms sputtered from alloys,” *Nucl Instruments Methods Phys Res Sect B Beam Interact with Mater Atoms*, vol. 270, pp. 50–54, 2012.
- [174] P. Sigmund, *Fundamental processes in sputtering of atoms and molecules (SPUT92): symposium on the occasion of the 250th anniversary of the Royal Danish Academy of Sciences and Letters, Copenhagen, 30 August-4 September, 1992: invited reviews*, vol. 43. Kongelige Danske videnskabernes selskab, 1993.

- [175] A. Sakaya, T. Yamazaki, T. Kikuta, T. Yoshizawa, H. Hirate, and T. Kida, “Thickness Distribution of Metal Films by Magnetron Sputtering,” *J Vac Soc Japan*, vol. 54, pp. 184–187, 2011.
- [176] S. Swann, “Film thickness distribution in magnetron sputtering,” *Vacuum*, vol. 38, no. 8–10, pp. 791–794, 1988.
- [177] J. A. Thornton and D. W. Hoffman, “Stress-related effects in thin films,” *Thin Solid Films*, vol. 171, no. 1, pp. 5–31, Apr. 1989.
- [178] D. M. Mattox, *Handbook of physical vapor deposition (PVD) processing*. William Andrew, 2010.
- [179] P. Bai, J. F. McDonald, T. -M. Lu, and M. J. Costa, “Effect of substrate surface roughness on the columnar growth of Cu films,” *J Vac Sci Technol A Vacuum, Surfaces, Film*, vol. 9, no. 4, pp. 2113–2117, 1991.
- [180] J. W. Patten, “The influence of surface topography and angle of adatom incidence on growth structure in sputtered chromium,” *Thin Solid Films*, vol. 63, no. 1, pp. 121–129, 1979.
- [181] K. Robbie, “Sculptured thin films and glancing angle deposition: Growth mechanics and applications,” *J Vac Sci Technol A Vacuum, Surfaces, Film*, vol. 15, no. 3, p. 1460, 1997.
- [182] J. Vetter, M. Stuber, and S. Ulrich, “Growth effects in carbon coatings deposited by magnetron sputtering,” *Surf Coatings Technol*, vol. 168, pp. 169–178, 2003.
- [183] P. Panjan, M. Čekada, M. Panjan, and D. Kek-Merl, “Growth defects in PVD hard coatings,” *Vacuum*, vol. 84, no. 1, pp. 209–214, 2009.
- [184] P. Chaudhari, “Hillock growth in thin films,” *J Appl Phys*, vol. 45, no. 10, pp. 4339–4346, 1974.
- [185] H. Palancher, A. Bonnin, V. Honkimäki, H. Suhonen, P. Cloetens, T. Zweifel, R. Tucoulou, A. Rack, and M. Voltolini, “Coating thickness determination in highly absorbent core–shell systems,” *J Appl Crystallogr*, vol. 45, no. 5, pp. 906–913, 2012.
- [186] A. M. Phillips, G. S. Mickum, and D. E. Burkes, “Thermophysical properties of U-10MO alloy,” Idaho National Laboratory (INL), 2010.
- [187] Y.-C. Chieh, W.-Z. Lo, and F.-H. Lu, “Microstructure evolution of ZrN films annealed in vacuum,” *Surf Coatings Technol*, vol. 200, no. 10, pp. 3336–3340, 2006.
- [188] M. J. Verrilli and M. G. Castelli, “Thermomechanical fatigue behavior of materials: Second volume,” 1996.
- [189] U. S. B. of L. Management, *Broadwell Basin Specified Hazardous Waste Facility, San Bernardino County: Environmental Impact Statement*, no. V. 2. 1993.
- [190] A. G. Evans and J. W. Hutchinson, “The thermomechanical integrity of thin films and multilayers,” *Acta Metall Mater*, vol. 43, no. 7, pp. 2507–2530, 1995.

- [191] R. E. Cuthrell, F. P. Gerstle, and D. M. Mattox, "Measurement of residual stresses in films of unknown elastic modulus," *Rev Sci Instrum*, vol. 60, no. 6, pp. 1018–1020, 1989.
- [192] S. M. Hu, "Film-edge-induced stress in substrates," *J Appl Phys*, vol. 50, no. 7, pp. 4661–4666, 1979.
- [193] R. L. Williamson, B. H. Rabin, and J. T. Drake, "Finite element analysis of thermal residual stresses at graded ceramic-metal interfaces. Part I. Model description and geometrical effects," *J Appl Phys*, vol. 74, no. 2, pp. 1310–1320, 1993.
- [194] P. Temple-Boyer, C. Rossi, E. Saint-Etienne, and E. Scheid, "Residual stress in low pressure chemical vapor deposition SiN<sub>x</sub> films deposited from silane and ammonia," *J Vac Sci Technol A Vacuum, Surfaces, Film*, vol. 16, no. 4, pp. 2003–2007, 1998.
- [195] K. Ito, H. Kuriki, H. Araki, S. Kuroda, and M. Enoki, "Detection of segmentation cracks in top coat of thermal barrier coatings during plasma spraying by non-contact acoustic emission method," *Sci Technol Adv Mater*, vol. 15, no. 3, p. 35007, 2014.
- [196] H. A. Nied, "Ceramic coating edge failure due to thermal expansion interference," *J Eng gas turbines power*, vol. 120, no. 4, pp. 820–824, 1998.
- [197] F. J. Humphreys and M. Hatherly, *Recrystallization and related annealing phenomena*. Elsevier, 2012.
- [198] A. A. Voevodin, D. V. Shtansky, E. A. Levashov, and J. J. Moore, *Nanostructured thin films and nanodispersion strengthened coatings*, vol. 155. Springer Science & Business Media, 2006.
- [199] S. S. Panwar, P. T. UMASANKAR, K. Balasubramanian, and B. Venkataraman, "High-temperature stability of yttria-stabilized zirconia thermal barrier coating on niobium alloy—C-103," *Bull Mater Sci*, vol. 39, no. 1, pp. 321–329, 2016.
- [200] I. Brooks, P. Lin, G. Palumbo, G. D. Hibbard, and U. Erb, "Analysis of hardness–tensile strength relationships for electroformed nanocrystalline materials," *Mater Sci Eng A*, vol. 491, no. 1, pp. 412–419, 2008.
- [201] W. D. Callister and D. G. Rethwisch, *Fundamentals of materials science and engineering*, vol. 471660817. Wiley London, UK:, 2000.
- [202] I. A. Yakubtsov, P. Poruks, and J. D. Boyd, "Microstructure and mechanical properties of bainitic low carbon high strength plate steels," *Mater Sci Eng A*, vol. 480, no. 1, pp. 109–116, 2008.
- [203] H. E. Boyer and T. L. Gall, "Metals handbook; desk edition," 1985.
- [204] C. C. Koch and J. Narayan, "The Inverse Hall-Petch Effect—Fact or Artifact?," *MRS Online Proc Libr Arch*, vol. 634, 2000.

- [205] J. R. Trelewicz and C. A. Schuh, “The Hall–Petch breakdown in nanocrystalline metals: a crossover to glass-like deformation,” *Acta Mater*, vol. 55, no. 17, pp. 5948–5958, 2007.
- [206] C. E. Carlton and P. J. Ferreira, “What is behind the inverse Hall–Petch effect in nanocrystalline materials?,” *Acta Mater*, vol. 55, no. 11, pp. 3749–3756, 2007.
- [207] A. J. Detor and C. A. Schuh, “Tailoring and patterning the grain size of nanocrystalline alloys,” *Acta Mater*, vol. 55, no. 1, pp. 371–379, 2007.
- [208] M. A. Meyers, A. Mishra, and D. J. Benson, “Mechanical properties of nanocrystalline materials,” *Prog Mater Sci*, vol. 51, no. 4, pp. 427–556, 2006.
- [209] Z. B. Qi, P. Sun, F. P. Zhu, Z. C. Wang, D. L. Peng, and C. H. Wu, “The inverse Hall–Petch effect in nanocrystalline ZrN coatings,” *Surf Coatings Technol*, vol. 205, no. 12, pp. 3692–3697, 2011.
- [210] A. A. Griffith, “AA Griffith, R. Soc. London Philos. Trans., Ser. A 221, 163 (1921).,” *R Soc London Philos Trans, Ser A*, vol. 221, p. 163, 1921.
- [211] H. Xu and H. Guo, *Thermal barrier coatings*. Elsevier, 2011.
- [212] Y. S. Kim, G. L. Hofman, J. S. Cheon, A. B. Robinson, and D. M. Wachs, “Fission induced swelling and creep of U–Mo alloy fuel,” *J Nucl Mater*, vol. 437, no. 1, pp. 37–46, 2013.
- [213] B. Narayanan, K. Sasikumar, Z.-G. Mei, A. Kinaci, F. G. Sen, M. J. Davis, S. K. Gray, M. K. Y. Chan, and S. K. R. S. Sankaranarayanan, “Development of a Modified Embedded Atom Force Field for Zirconium Nitride Using Multi-Objective Evolutionary Optimization,” *J Phys Chem C*, vol. 120, no. 31, pp. 17475–17483, 2016.
- [214] V. P. Sinha, P. V Hegde, G. J. Prasad, G. K. Dey, and H. S. Kamath, “Phase transformation of metastable cubic  $\gamma$ -phase in U–Mo alloys,” *J Alloys Compd*, vol. 506, no. 1, pp. 253–262, 2010.
- [215] T. W. Cho, “Measurements and Modeling of Thermal Conductivity of U-Mo/Al Dispersion Fuel for Research Reactor,” 2018.
- [216] G. J. Prasad, V. P. Sinha, and P. V Hegde, “Development and Fabrication of LEU Plate Fuel for Modified Core of APSARA Reactor,” *BARC Newsl*, pp. 21–27, 2012.
- [217] M. Hara, Y. Hatano, T. Abe, K. Watanabe, T. Naitoh, S. Ikeno, and Y. Honda, “Hydrogen absorption by Pd-coated ZrNi prepared by using Barrel-Sputtering System,” *J Nucl Mater*, vol. 320, no. 3, pp. 265–271, 2003.
- [218] M. Metzler and Y. Lu, “Cambridge Nanotech Savannah Atomic Layer Deposition (ALD) Film Characterization,” 2016.
- [219] B. Hafner, “Energy Dispersive Spectroscopy on the SEM,” *Charact Facil Univ Minnesota, USA*, 2011.

- [220] A. H. M. Areef Billah, “Investigation of multiferroic and photocatalytic properties of Li doped BiFeO<sub>3</sub> nanoparticles prepared by ultrasonication,” 2016.
- [221] L. Corbari, M.-A. Cambon-Bonavita, G. J. Long, F. Grandjean, M. Zbinden, F. Gaill, and P. Compère, “Iron oxide deposits associated with the ectosymbiotic bacteria in the hydrothermal vent shrimp *Rimicaris exoculata*,” *Biogeosciences Discuss*, vol. 5, no. 2, pp. 1825–1865, 2008.
- [222] C. Gillet, V. Mary, V. Sanchez Garcia de la Torre, S. Thomine, and B. Satiat-Jeunemaître, “Subcellular localization of metal pools determined by TEM-EDS in embryo *Arabidopsis thaliana* mutants,” in *European Microscopy Congress 2016: Proceedings*, 2016, pp. 121–122.
- [223] “Lecture 3 : Powder diffraction.” .



## Acknowledgements

First, I am deeply grateful to my ex-advisor, Prof. Dong-Seong Sohn and Prof. Deokjung Lee, for his continuous support and patience throughout my Ph.D course. Besides my advisors, I would like to thank the rest of my thesis committee: Dr. Jong Man Park, Dr. Yeon Soo Kim, Prof. Jaeyeong Park, for their constructive comments and suggestions, but also for the questions which incited me to widen my research from various perspectives. Their feedback was invaluable. Particularly, I am grateful for the assistance given by Dr. Yeon Soo Kim. His guidance helped me in all the time of research and writing of this thesis.

Next, I would like to thank all members of Research Reactor Fuel Development Division at KAERI for providing the U-Mo fuel powders, facilities, and the financial support that permitted me to complete. Specially, I am deeply indebted to Dr. Jong Man Park, Dr. Yong Jin Jeong, and Dr. Sunghwan Kim, who provided me an opportunity to join their team, and who gave access to the laboratory and research facilities. Without their precious support it would not be possible to conduct this research.

My acknowledgement would be incomplete without expressing the deepest appreciation to people who are the greatest source of my strength. I would like to thank my groom-to-be, Bosung LEE, for giving me insights, for being so thoughtful and supportive during my Ph.D period, and for putting up with me in difficult moments when I was mentally and physically tough. Also, I would like to offer my special thanks to my family including my mom and maternal grandmother who raised me and gave me unforgettable good memories. Without their unwavering support and warm encouragement, it would not be possible to complete this thesis. I dedicate this thesis to them.

Ji Hyeon Kim

## Journal Publications

1. J.-H. Kim, G. Y. Jeong, S. Kim, Y. J. Jeong, and D.-S. Sohn, “Effect of coating thickness and annealing temperature on ZrN coating failure of U-Mo particles under heat treatment,” *J. Nucl. Mater.*, vol. 507, pp. 347–359, 2018.
2. J.-H. Kim, G. Y. Jeong, S. Kim, Y. J. Jeong, J. M. Park, and D.-S. Sohn, “Dependence of thickness, morphology, and crystallographic properties of Mo and ZrN coatings on U-Mo substrate size,” *J. Nucl. Mater.*, 2018.
3. J.-H. Kim, S. Kim, Y. J. Jeong, J. M. Park, and D.-S. Sohn, “Effect of coating thickness on the microstructure and residual stress of non-reactively sputtered ZrN coating on U-Mo particles,” *Surf. Coatings Technol.*, 2018, submitted.